Final report

for

Development of high performance ODS alloys

Technical Work Scope Identifier No.: FC-2.2 (High performance cladding and core components)

PI: Lin Shao (Texas A&M University)
Co-PI: Fei Gao (University of Michigan) and Frank Garner (Texas A&M University)

A Proposed scope description

This project aims to capitalize on insights developed from recent high-dose self-ion irradiation experiments in order to develop and test the next generation of optimized ODS alloys needed to meet the nuclear community's need for high strength, radiation-tolerant cladding and core components, especially with enhanced resistance to void swelling. Two of these insights are that ferrite grains swell earlier than tempered martensite grains, and oxide dispersions currently produced only in ferrite grains require a high level of uniformity and stability to be successful. An additional insight is that ODS particle stability is dependent on as-yet unidentified compositional combinations of dispersoid and alloy matrix, such as dispersoids are stable in MA957 to doses greater than 200 dpa but dissolve in MA956 at doses less than 200 dpa. These findings focus attention on candidate next-generation alloys which address these concerns. Collaboration with two Japanese groups provides this project with two sets of first-round candidate alloys that have already undergone extensive development and testing for unirradiated properties, but have not yet been evaluated for their irradiation performance. The first set of candidate alloys are dual phase (ferrite + martensite) ODS alloys with oxide particles uniformly distributed in both ferrite and martensite phases. The second set of candidate alloys are ODS alloys containing non-standard dispersoid compositions with controllable oxide particle sizes, phases and interfaces.

The project will employ coordinated experiments to study swelling, radiation hardening and changes in mechanical properties not only of these ODS alloys, but also further-optimized ODS candidates resulting from these first-round studies. The project will identify key factors influencing radiation tolerance of new ODS alloys for further property optimization. In addition to void swelling, post-irradiation testing will focus on atomic scale characterization of oxide particle stability, elemental segregation at oxide-matrix interface, and overall phase stability of alloys under extreme radiation conditions. Mechanical characterization efforts will include various micron-level mechanical tests, including pillar compression experiments and indentation experiments. To gain atomic scale understanding, the project will integrate these experiments with modeling capabilities, including molecular dynamics and dislocation dynamics simulations to understand the roles of yttria and other dispersoids as well as their various dispersion modes on both microstructural changes and mechanical property changes.

B Cumulative list of journal publications from the project: 18

1 T. Chen, H. Kim, J. Gigax, D. Chen, C-C. Wei, F.A. Garner, L. Shao, “Radiation response of oxide-dispersion-strengthened alloy MA956 after self ion irradiation”, ***Nucl. Instrum. Methods Phys. Res. B*** 409, 259-263 (2017).

2 Jonathan G. Gigax, Hyosim Kim, Eda Aydogan, Frank A. Garner, Stu Maloy & Lin Shao, "Beam-contamination-induced compositional alteration and its neutron-atypical consequences in ion simulation of neutron-induced void swelling", ***Mat. Res. Lett***. 5, 478-485 (2017).

3 Changwoo Kang, Q. Wang, L. Shao, "Kinetics of interstitial defects in alpha-Fe: the effect from uniaxial stress", ***J. Nucl. Mat***. 485, 159-168, 2017

4 E. Aydogan, S.A. Maloy, O. Anderoglu, C. Sun, J.G. Gigax, L. Shao, F.A. Garner, I.E. Anderson, J.J. Lewandowski, "Effect of tube processing methods on microstructure, mechanical properties and irradiation response of 14YWT nanostructured ferritic alloys", ***Acta Materialia*** 134, 116-127 (2017).

5 L. Shao, J. Gigax, D. Chen, H. Kim, F.A. Garner, J. Wang, M.B. Toloczko, "Standardization of accelerator irradiation procedures for simulations of neutron induced damage in reactor structural materials", ***Nucl. Instrum. Methods Phys. Res. B*** 409, 251-254 (2017).

6 J.G. Gigax, H. Kim, T. Chen, F.A. Garner, L. Shao, "Radiation instability of equal channel angular extruded T91 at ultra-high damage levels", ***Acta Materialia*** 132, 395-404 (2017).

7 Eda Aydogan, et al., "Microstructural changes induced by high dose self-ion irradiation in EK-181 alloy in ferritic annealed and severe-plastically-deformed conditions", ***J. Nucl. Mat.*** 487, 96-104 (2017).

8 E. Aydogan, N. Almirall, G.R. Odette, S.A. Maloy, O. Anderoglu, L. Shao, J.G. Gigax, L. Price, D. Chen, T. Chen, F.A. Garner, Y. Wu, P. Wells, J.J. Lewandowski, D.T. Hoelzer, Stability of nanosized oxides in ferrite under extremely high dose self ion irradiations, ***J. Nucl. Mat***. 486, 86-95 (2017).

9 C. Kang, Q. Wang, L. Shao, Kinetics of interstitial defects in alpha-Fe: The effect from uniaxial stress, ***Journal of Nuclear Materials*** 485, 159-168 (2017).

10 J.G. Gigax, T. Chen, Hyosim Kim, J. Wang, L.M. Price, E. Aydogan, S.A. Maloy, D.K. Schreiber, M.B. Toloczko, F.A. Garner, Lin Shao, Radiation response of alloy T91 at damage levels up to 1000 peak dpa, ***Journal of Nuclear Materials*** 482, 257-265 (2016).

11 Tianyi Chen, Jonathan G. Gigax, Di Chen, Lloyd Price, Xuemei Wang, S. Ukai, Eda Aydogan, Stu Maloy, F. A. Garner, Lin Shao, "Temperature dependent dispersoid stability in ion-irradiated ferritic-martensitic dual-phase oxide-dispersion-strengthened alloy: coherent vs. incoherent interfaces", ***Acta Materialia*** 116, 29-42(2016).

12 Q. Yan, J. Gigax, D. Chen, F.A. Garner, L. Shao, Monte Carlo modeling of cavity imaging in pure iron using back-scatter electron scanning microscopy, ***Journal of Nuclear Materials*** 480, 420-428 (2016).

13 J. Wang, M.B. Toloczko, N. Bailey, F.A. Garner, J. Gigax, L. Shao, Modification of SRIM-calculated dose and injected ion profiles due to sputtering, injected ion buildup and void swelling, Nucl. Instrum. Methods Phys. Res. B 387, 20-28 (2016).

14 M.P. Higgins, C.Y. Lu, Z. Lu, L. Shao, L.M. Wang, F. Gao, "Crossover from disordered to core-shell structures of nano-oxide Y2O3 dispersed particle in Fe", ***Applied Physics Letters*** 109, 031911 (2016).

15 Lin Shao, "Ion accelerator based radiation simulation of neutron damage in reactors: issues and challenges in experiments and modeling", ***Nucl. Safety & Simulation*** 6, 234 (2015).

16 Tianyi Chen, Eda Aydogan, Jonathan Gigax, Di Chen, Jing Wang, Xuemei Wang, S. Ukai, Yuedong Wu, Yong Yang, F.A. Garner, and Lin Shao, "Microstructural development and void

swelling of a 12Cr ODS dual-phase steel during high-dose Fe2+ ion irradiation", ***J. Nucl. Mat.*** 467, 42-49 (2015)

17 J. Gigax, Eda Aydogan, Tianyi Chen, Di Chen, Lin Shao, Y. Wu, W.Y. Lo, Y. Yang, F.A. Garner "The influence of beam rastering on the swelling of self-ion irradiated pure iron at 450°C", ***J. Nucl. Mat***. 465, 343-348 (2015).

18 S. Pasebani, I. Charit, J. Burns, S. Alsagabi, D.P. Butt, J.I. Cole, L.M. Price, L. Shao, "Microstructural stability of a self-ion irradiated lanthana-bearing nanostructured ferritic steel", ***J. Nucl. Mat.*** 462, 191 (2015).

C Cumulative list of conference publication from the project: 1

Lin Shao, Jonathan Gigax, Hyosim Kim, Frank A. Garner, Jing Wang, Mychailo B. Toloczko, "Carbon contamination, its consequences and its mitigation in ion-simulation of neutron-induced swelling of structural metals', Environmental degradation of materials in nuclear power systems, page 681-693, 2017.

D Student dissertations resulted from the project

The project has resulted in two Ph.D degree (Tianyi Chen in 2015 and Jonathan Gigax in 2017). The third Ph.D student is about to finish in 2018. Dr. Tianyi Chen was hired as a postdoc at Oak Ridge National Laboratory and Dr. Jonatan Gigax was hired as a postdoc at Los Alamos National Laboratory.

- Tianyi Chen, Ph.D dissertation, "Radiation response of oxide dispersion strengthened alloy", 2015, Texas A&M University.

- Jonathan Gigax, Ph.D dissertation, "Neutron atypical effects and the influence on the radiation response of metallic alloys at ultra-high damage levels, 2017, Texas A&M University.

E Research Highlights

The project has impacted three major research directions: the first impact is establishment of correct ion beam testing procedures for high dap testing which can be used to a wide range of alloys; the second impact is obtaining fundamentals understandings of ODS behaviors under irradiation including matrix effects, temperature effect, dpa effect and dpa rate effects; and the third impact is to developing novel ODS alloys with either enhanced radiation tolerance or reduced costs. Below, we summarize these highlights.

1. Establishment of correct procedures for ion irradiation testing: rastering vs. defocusing beams
2. Establishment of correct procedures for ion irradiation testing: carbon contamination and solutions
3. Radiation response of oxide-dispersion-strengthened alloy MA 956 after self-ion irradiation
4. Dispersoid stability in ion irradiated ODS alloy: matrix effect (ferritic vs. martensitic)
5. Dispersoid stability in ion irradiated ODS alloy: temperature effect
6. Dispersoid stability in ion irradiated ODS alloy: dpa rate effect
7. Molecular dynamics simulations of oxide particles in Fe
8. Irradiation of rare-earth-oxide-particle strengthened alloys

Research highlight #1

F-1 Establishment of correct procedures for ion irradiation testing: rastering vs. defocusing beams

We studied the influence of beam rastering on the swelling of self-ion irradiated pure iron. This study is important since it builds the foundation of accelerator based testing. Beam scanning or "rastering" is a technique that is frequently used to uniformly cover a larger specimen area during ion irradiation. In this study we addressed the effects of rastered and defocused beams, using 3.5 MeV iron ions to irradiate pure iron at 450°C to peak doses of 50 and 100 dpa. We focused on a frequency range relevant to pulsed fusion devices and show its importance to ion irradiation experiments simulating neutron damage. The beam was scanned at 15.6, 1.94, and 0.244 Hz and the resulting microstructure was compared with that produced by a non-rastered, defocused beam. At 150 dpa the defocused beam case resulted in the highest observed void swelling of ~30% at a depth of ~800 nm, a depth short of the peak dose position at 1000 nm where the dose was 150 dpa. The swelling at 1000 nm was significantly reduced by the defect imbalance phenomenon. A maximum swelling rate of ~0.3%/dpa was measured in this specimen at a depth of 500 nm below the ion-incident surface. Rastering led to much lower swelling levels achieved at significantly lower swelling rates, with the greatest rate of decrease occurring below ~1 Hz. Furthermore, the impact of the defect imbalance arising from interstitial injection and spatial distribution difference of initial interstitial and vacancy defects was strongly pronounced in the non-rastered case with a lesser effect observed with decreasing raster frequency.

F1-1 Introduction

Void swelling of structural alloys is a life-limiting phenomenon of great importance for sustained performance of reactor components. This phenomenon causes volume changes, distortion, changes in mechanical properties and sometimes embrittlement [1]. To study this phenomenon ion irradiation is often used as a surrogate for neutron irradiation to study void swelling [2]. However, there are significant differences between ion and neutron irradiation, especially with respect to the spatial and temporal distribution of radiation damage, as well as in void morphology, sizes and distribution. For neutron irradiation, there are essentially no gradients in dpa rate over dimensions comparable to grain sizes in metals, but there are two primary temporal regimes of interest. These are continuous, steady-state operation (i.e. fission reactors, Tokamak fusion reactors) and pulsed operation (i.e. inertial fusion reactors). In ion irradiation, however, spatial gradients can be very strong, often on sizes smaller than a typical grain diameter, and the ion irradiation can use either a continuous, defocused beam or a focused and scanned beam, the latter often referred to as "rastering".

In order to irradiate a large area, beam rastering is often performed. However, ASTM E521-77 [3] strongly suggests using a defocused beam rather than a scanned beam to simulate damage from steady-state neutron irradiation, noting that a phenomenon called "void throttling" can occur at high temperatures, whereby void nuclei formed at a given location during the beam-on period dissolve in the longer beam-off period before the beam returns. This suggestion, however, is based on a limited set of early (1970's) experiments on pure nickel [4-6] and therefore requires additional investigation before accepting it as a universal proscription against rastering.

The current work addressed the impact of rastering at relatively low frequencies on void swelling in pure iron which was used as a model surrogate material for more complex ferritic alloys to be studied in

later irradiations. In this experiment a limited ranged of low rastering frequencies relevant to pulsed fusion devices was used to produce void swelling and the results were compared with that produced by a steady-state, non-rastered, defocused beam.

F1-2 Experimental details

Samples were prepared from a pure iron bar (99.99%, Sigma-Aldrich) to produce disks of size 4 mm × 4 mm × 0.5 mm. These disks were mechanically polished on a Dace Technologies Nano 2007 polisher using successive grits of 600, 800, and 1200 silicon carbide paper. The samples were further polished using 1 μm and 0.05 μm alumina solutions. After mechanical polishing, the samples were electropolished using a 6% perchloric, 94% acetic solution for 10 seconds to remove all surface damage arising from mechanical polishing. The specimens were then inspected using a scanning electron microscope to ensure an undamaged surface.

The specimens were mounted on an electrically-heated copper stage and good thermal contact was maintained using silver paste. These specimens were brought to a temperature of 450°C measured using thermocouples mounted to the stage. Independent measurements were performed to verify that the beam heating arising from a defocused beam was less than 10°C. The procedure involved coating a thin aluminum grid pattern onto a polished iron surface. The specimen was then heated to a temperature just below the melting point of aluminum and then ion-irradiation was commenced. Comparing the deposition pattern before and after irradiation, the beam heating was deduced by taking the difference between the sample stage temperature at which melting was observed to just begin and the melting temperature of aluminum.

Iron ion irradiation was performed by using a 1.7 MV tandem accelerator with an energy of 3.5 MeV, producing peak damage levels at 1000 nm below the surface of 50 and 150 dpa, as calculated using the Kinchin-Pease option of the SRIM-2013 code [7] as recommended by Stoller and coworkers [8]. There was no gas co-injection employed in this study. The beam current was limited to 200 nA over an area of 36 mm^2, yielding a time-averaged dpa rate of 1.74×10^{-3} dpa/s, varying less than 5% over the duration of the experiment. Beam conditions are listed in Table 1 for all four beam conditions. The beam spot size for the defocus case was chosen to be 6 mm x 6 mm. The configuration for the defocus case involved using an electrostatic quadruple to produce a uniform beam over the desired area. To simplify the analysis, the beam involved one-dimensional rastering rather than the frequently used two-dimensional raster method.

The beam size for the raster case was 2.5 mm x 4 mm and scanned over an area of 9 mm x 4 mm, larger than the specimen size to ensure that all areas were irradiated uniformly. The ion beam was rastered using a Physicon Model RS1200 with a horizontal raster speed at 0.244, 1.93, and 15.625 Hz. The irradiated samples were characterized by cross sectional transmission electron microscopy (TEM), with specimen preparation accomplished using the focused-ion-beam (FIB) based lift-out technique. Microstructural analysis was performed using a FEI Tecnai G2 F20 instrument, operated at 200 kV.

F1-3 Results

Figures 1a-1d show TEM micrographs of 50 dpa specimens obtained with a rastering beam at frequencies of 15.63 Hz, 1.95 Hz, 0.244 Hz , and with a defocused beam, respectively. With decreasing rastering frequencies, void sizes tend to be smaller and densities tend to be higher. In comparison, defocusing results in larger voids. However, we note that, in all cases, voids formed into octahedral-like shapes deduced from the observed square and hexagon shaped voids as predicted by Wulff construction theory[9]. Figures 2a-2d show the TEM micrographs of 150 dpa specimens. The observed differences in

void density, sizes, and shapes at 150 dpa are consistent under different rastering conditions and defocusing with observations from the 50 dpa experiments.

For a better comparison at 50 dpa, depth-dependent void swelling profiles are divided into two groups. Figure 3 compares the 15.63 Hz and 1.95 Hz rastering frequency, and Figure 4 compares 0.244 Hz raster and defocused beam conditions. One general trend is that with decreasing frequencies, the void distributions reach deeper into the specimen. For the lowest frequency, 0.244 Hz, the void distribution is comparable to that of a defocused beam. The "spikeness" of the swelling vs. depth profiles is an artifact of the relatively low number of voids and the choice of sampling statistics. Note that no voids were found in the 50 dpa specimen beyond ~650 nm depth in the defocus case, most likely resulting from the strong influence of the injected interstitial to suppress both void nucleation and subsequent growth [10, 11]. In Table 1 - Raster and defocused beam parameters including the duty factor, beam-on and beam-off times, and instantaneous and average dpa rates.

		Beam-On (s)	Beam-Off (s)	Duty Factor	Instantaneous dpa rate when beam is on (dpa/s)	Time-averaged dpa rate through the whole irradiation (dpa/s)
Raster	15.63 Hz	0.018	0.046	28%	6.26E-3	1.74E-3
	1.95 Hz	0.142	0.370			
	0.244 Hz	1.14	2.96			
Defocus		-	-	100%	1.74E-3	

Table 2 - Void characteristics measured at the peak dpa location from the current study. Void swelling at 500 nm below the surface is also provided for each set of samples.

	50 DPA				150 DPA			
	Maximum Void Swelling (%)	Void Swelling at 500 nm (32 dpa)	Void Density (10^{14}/cm^3)	Average Radius (nm)	Maximum Void Swelling (%)	Void Swelling at 500 nm (96 dpa)	Void Density (10^{14}/cm^3)	Average Radius (nm)
15.63 Hz	0.322	0	3.49	9.43	4.34	2.95	7.67	11.24
1.95 Hz	1.48	0	21.8	7.94	8.50	3.64	2.63	13.45
0.244 Hz	1.13	0.825	53.6	5.0	9.76	4.60	31.65	6.44
Defocus	1.52	1.038	7.24	11.8	29.50	17.92	5.61	19.11

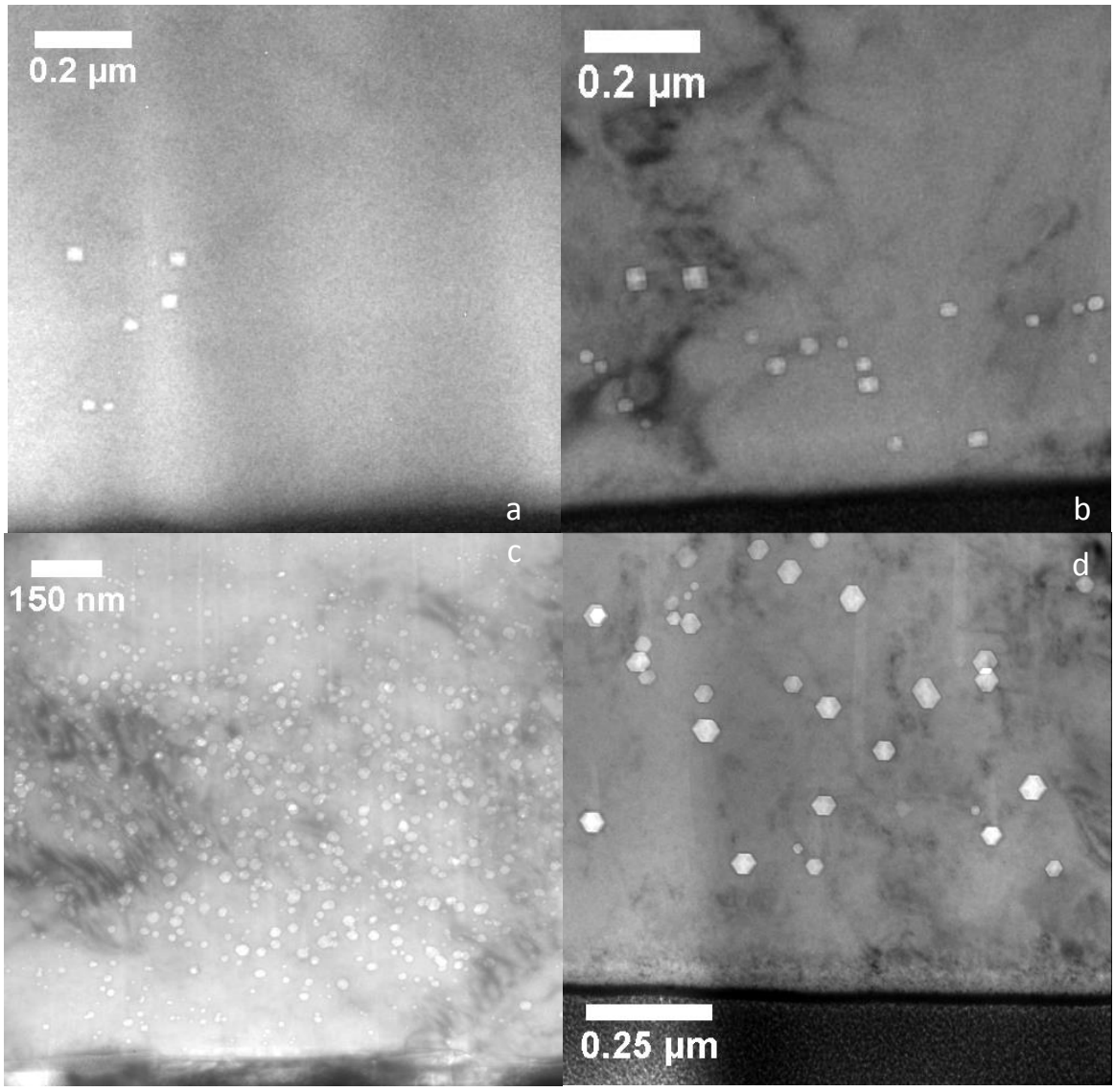

Figure 1 - Micrographs of void swelling for irradiation to 50 dpa at peak maximum in pure iron for rastered beams at. (a) 15.63 Hz, (b) 1.95 Hz, (c) 0.244 Hz , and at (d) defocus condition.

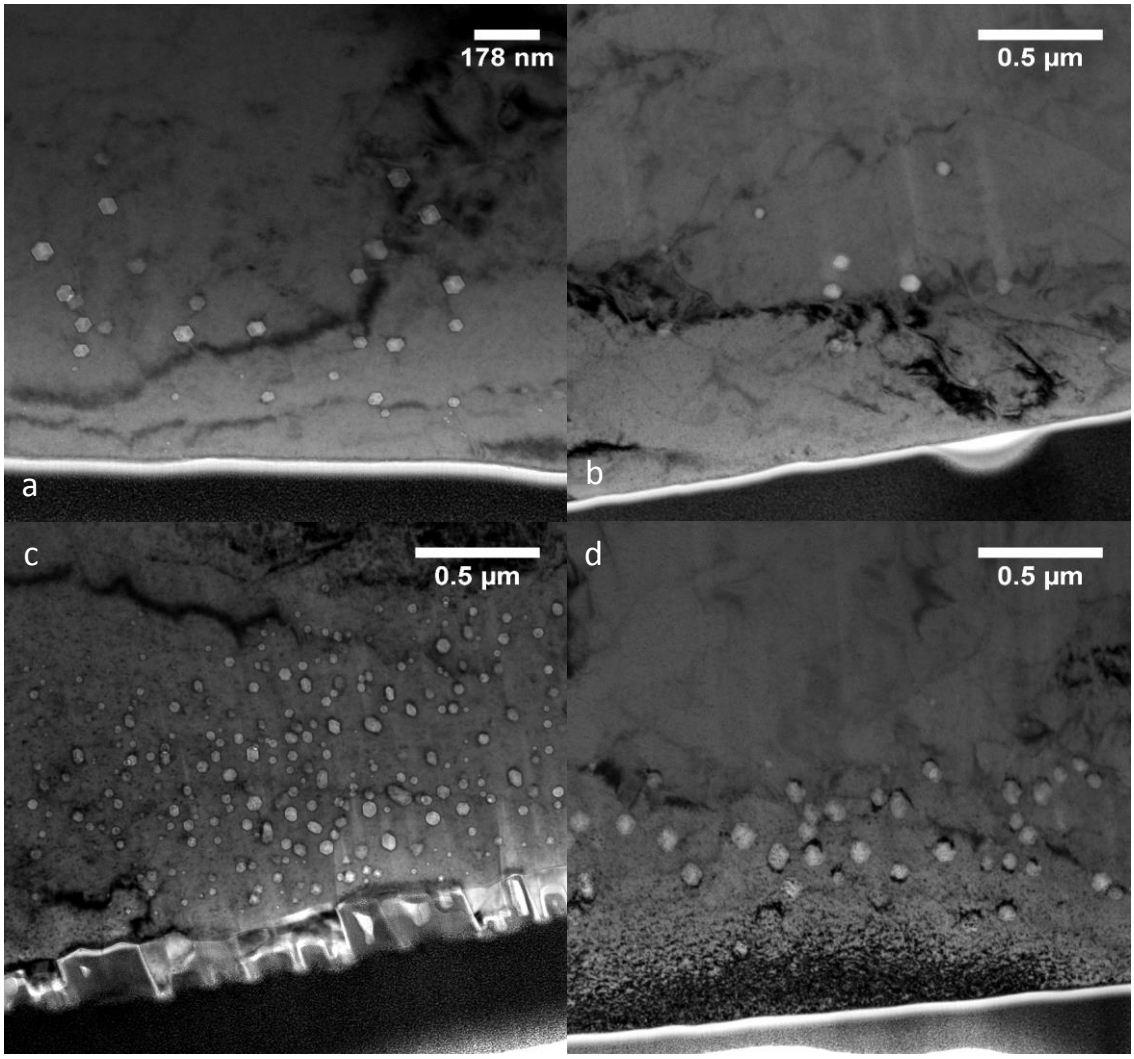

Figure 2 - Micrographs of void swelling for irradiation to 150 dpa at peak maximum in pure iron for rastered beams at (a) 15.63 Hz, (b) 1.95 Hz, (c) 0.244 Hz, and with a (d) defocused beam condition.

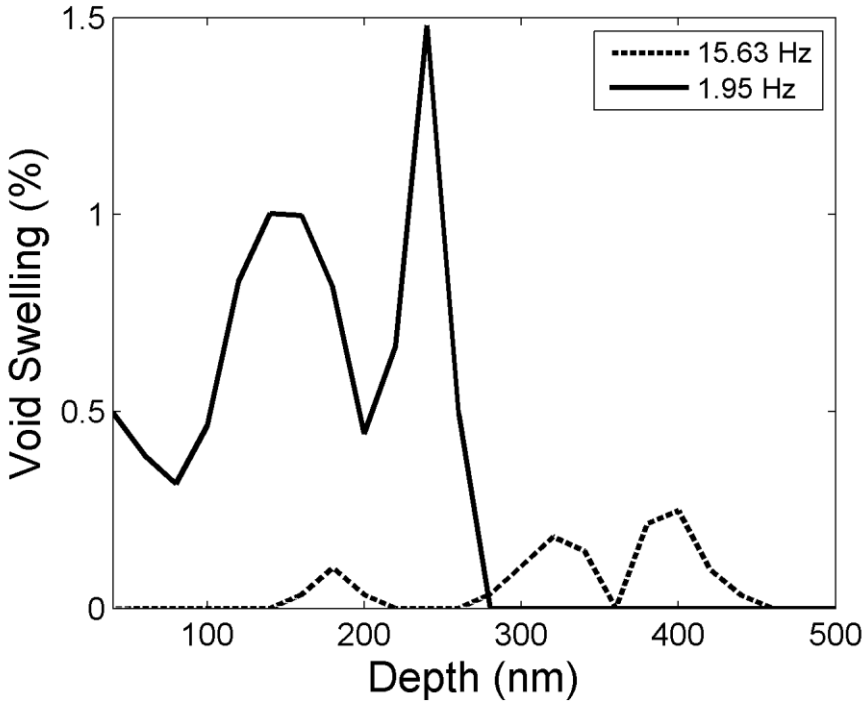

Figure 3. Comparison of depth dependent swelling for 50 peak dpa irradiation with raster beam frequencies of 15.63 Hz and 1.95 Hz.

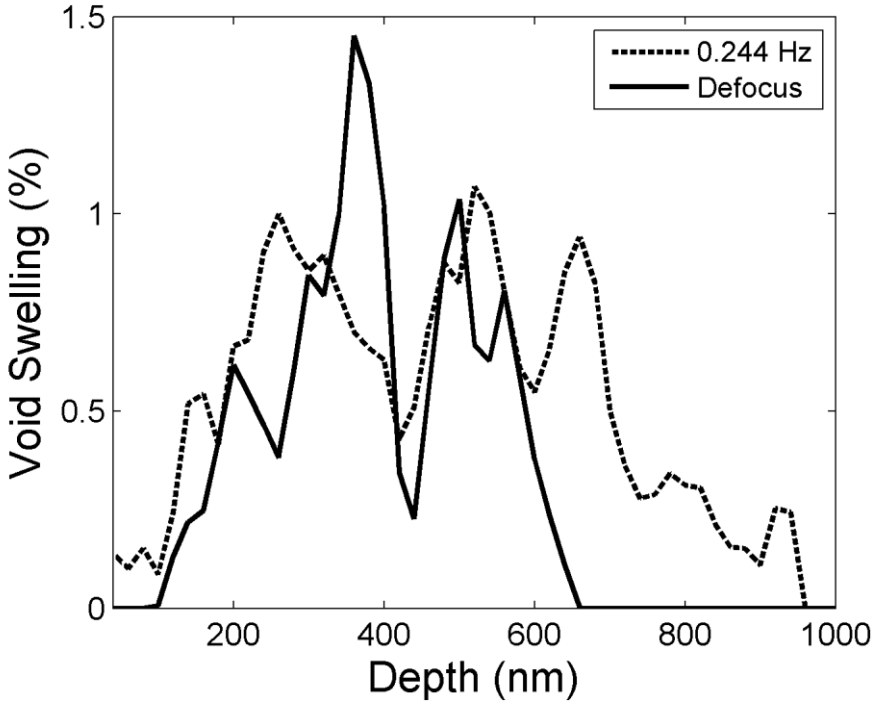

Figure 4 Comparison of depth-dependent swelling for 50 peak dpa irradiation with defocused beam and raster beam frequency of 0.244 Hz.

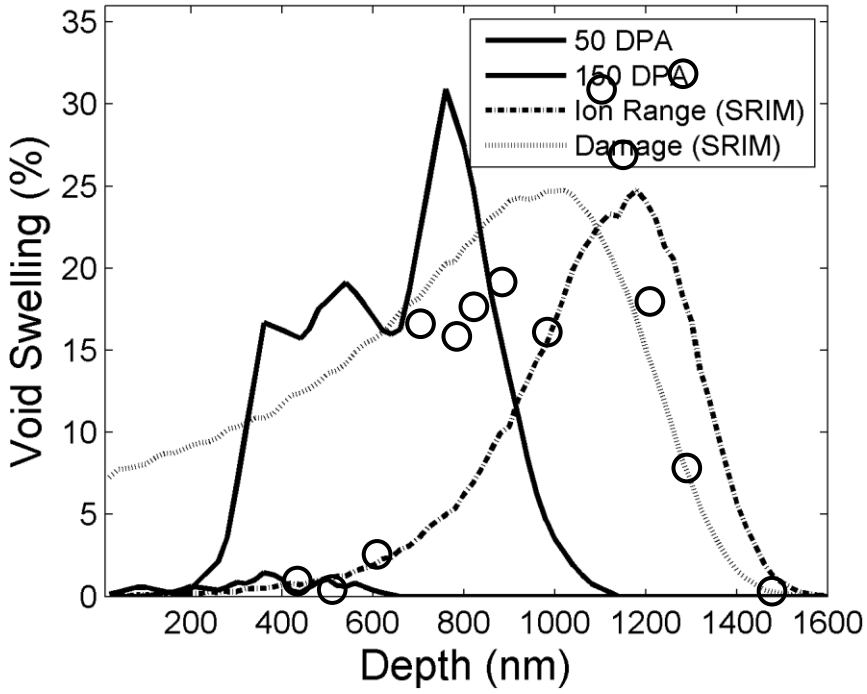

Figure 5 Comparisons of depth-dependent swelling from a defocus beam for 50 and 150 peak dpa. Both profiles of dpa and Fe implants from SRIM calculation are plotted for comparison.

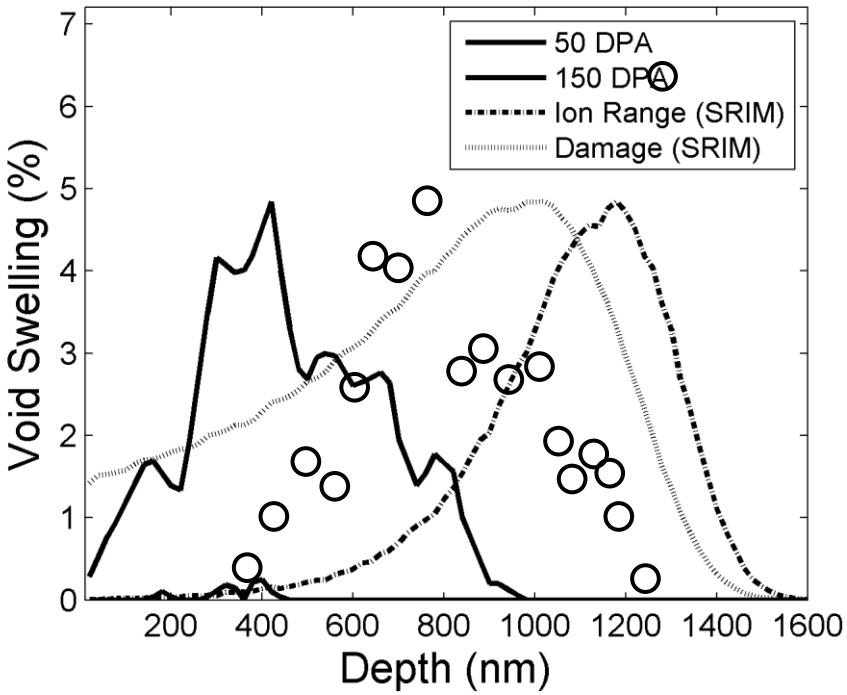

Figure 6 Comparisons of depth-dependent swelling from a 15.63 Hz rastering beam for 50 and 150 peak dpa. Both profiles of dpa and Fe implants from SRIM calculation are plotted for comparison.

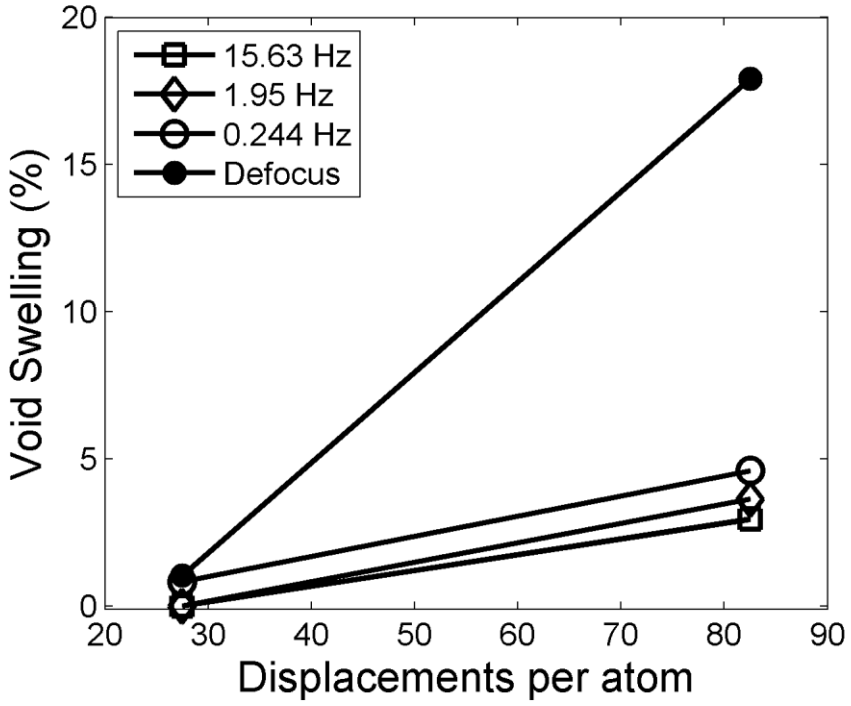

Figure 7 Void swelling rates as a function of DPA measured at the depth of 500 nm.

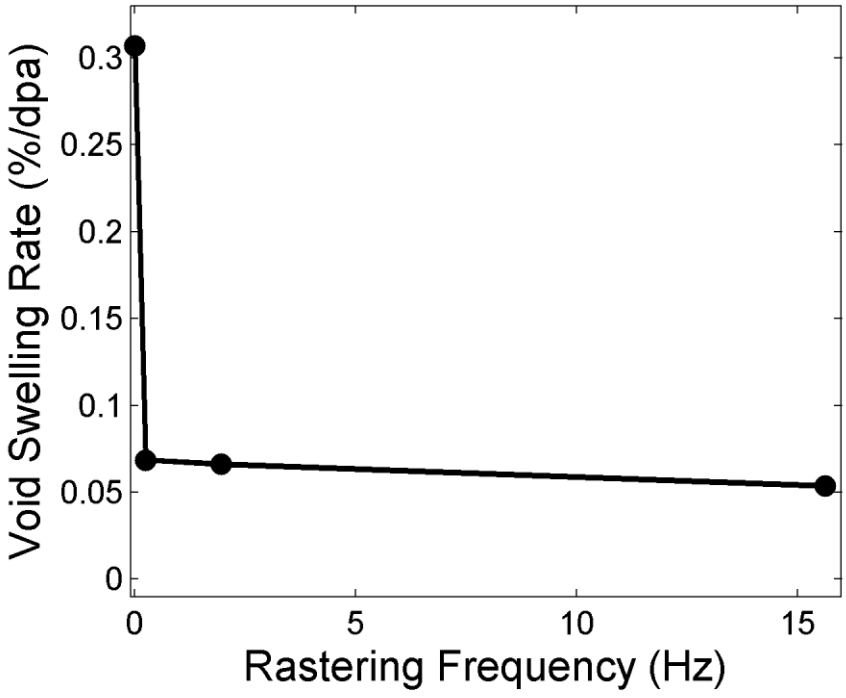

Figure 8 - Void swelling rates as a function of rastering frequencies. A frequency of zero corresponds to a defocused beam.

the rastered cases there is a progressive shortening of the voided region, moving back from 950 to 450 to 300 nm as the rastering frequency increases from 0.244 to 1.95 to 15.63 Hz. Notably, the slowest raster rate of 0.244 Hz produced voids to a deeper depth than did the non-raster case.\

Figures 5 and 6 show the depth profiles of void swelling for the defocused and 15.63 Hz cases for 50 dpa and 150 dpa, respectively. The void depth profiles are superimposed on the normalized SRIM-calculated dpa and injected interstitial profiles. Note that at 150 dpa, voids reach deeper into the sample compared to the 50 dpa case as void nucleation at the higher dose progressively overcomes the defect imbalance effect [11]. In both cases however, void swelling is depressed in the peak dpa region.

As also shown in Figures 5 and 6 there is a strong change in dose rate from the ion-incident surface to the peak dose position, increasing by a factor of ~3.7. In order to determine an unperturbed swelling rate between the 50 and 150 peak dpa cases without introducing differences in dpa rate, it is necessary select a depth for analysis that minimizes the influence of the specimen surface and also avoids the defect imbalance suppressed zone. Therefore, swelling data was taken from the depth of 500 nm ± 100 nm, where the average dose is only ~55% of the peak value. Thus, data were actually measured at 28 and 83 dpa rather than at 50 and 150 dpa. The swelling results are shown in Figure 7 and the void characteristics are presented in Table 2. Although our studies are limited to two dpa values only, the observed large swelling difference between the defocused and rastered cases are consistent. Clearly, rastering tends to suppress void swelling.

In Fig. 5, a peak swelling of ~30% at ~800 nm, along with a swelling of ~18% at a depth of 500 nm (corresponding to 83 dpa), was observed in the defocused irradiation, but that the rastering-produced swelling levels are significantly lower. As shown in Fig. 6, the void densities at both 50 and 150 dpa irradiations are lowest for the 15.63 Hz case, but all show a monotonic increase from 28 to 83 dpa. Overall, the depth-dependent swelling behaviors are complicated. As shown in Figure 8, the highest swelling rate of ~0.3% per dpa is obtained from a defocused beam, while all rastering cases lead to significantly lower swelling values, decreasing with increasing rastering frequency. Furthermore, rastering at relatively low frequencies decreases the swelling rate quickly, with a more gradual rate of decrease occurring beyond ~1 Hz.

There are two very significant observations resulting from this study. First, in pure iron there is a strong suppression of void nucleation and growth in the region where the peak dpa and the injected interstitial overlap. At higher doses the suppression effect is overridden somewhat but is never completely overcome. This behavior was observed not only in this study but in a previous study in the current experimental series [18]. Both the present study and the previous works suggest that swelling suppression effect requires that microstructural data be extracted from a depth removed from the injection zone. The defect imbalance effect [11], and previously reported injected interstitial effect [10, 12-19], is known to suppress both void nucleation and void growth near the end of the ion range. Our previous work has shown that the suppression effects come from two contributions [11]. The first is that extra atoms are implanted into the material, which increases the local interstitial population at the projected range. The other contribution comes from the small spatial distribution difference between vacancies and irradiation induced interstitials produced during the knock-on process in ion irradiation using a collimated beam. Although in damage cascade creation, the knock-on directions seems random, the statistical analysis shows that the overall knock-on interactions favor momentum transfer in the forward directions, which leads to interstitial distributions slightly deeper than that of vacancies. Thus vacancies are a little richer in the near surface region and interstitials are richer in the deposited ion range. Such spatial distribution differences, including the extra injected interstitials, lead to dramatic void swelling suppression near the end of range for ions. As the accumulated dose increases, these influences are overcome somewhat and the void distribution pushes deeper but not completely into the ion range. This

phenomenon was also observed in a study by Kuramoto and coworkers that showed that there was a strong but not total reduction of void swelling in pure iron close to the ion deposition range, with the complication that Kuramoto used nickel ions rather than iron ions, introducing some chemical alteration in the injected region [20]. It is very clear that rastering decreases the swelling rate, but there may be synergisms with other variables that were not revealed in this study. Such synergisms are suggested by the extension of the void range when going from defocused to 0.244 Hz, followed by a steady reduction in void range at higher rastering frequencies. Therefore it appears that the rastering and defect imbalance suppression effects may interact, suggesting the possibilities of more complicated dependencies at temperatures other than the 450°C employed in this study.

To provide an explanation of the underlying phenomenon involved in rastering we rely on the treatment given by previous works of Ghoniem and Kulcinski [21] and Simonen [22] that showed a significant difference between pulsed beam parameters and the resultant void swelling. The modeling was based on the defect interactions with existing void nuclei. In metals, interstitials are faster diffusing than vacancies. Further, in pure Fe with large grains, vacancy with interstitial recombination is the dominant interaction mechanism. Upon pulsed irradiation, interstitials are initially the primary component of the defect flux migrating towards the void nuclei, and cause their shrinkage. After a majority of the interstitials have diffused, the remaining vacancies diffuse towards and into the nuclei and thereby cause their growth. If there is a long duration between pulses, then voids begin to shrink due to vacancy emission at the void surface. Furthermore, if another pulse is introduced before significant vacancy diffusion occurs, the preexisting void nuclei will shrink further. This theory agrees with our observations that higher rastering frequencies lead to lower void swelling. On the other hand, we need to point out an additional complexity which was not considered in the previous modeling. First, if stable void nuclei have already formed prior to pulsed irradiation, the effect will not be as pronounced. The previous studies assumed the existence of void nuclei prior to the irradiation. Full scale modelling is required to account for the impact of pulsing on void nucleation. Second, the existence of strong defect sinks, e.g. high density grain boundaries, may change the defect flux towards the voids, and subsequently affect the overall stability of void nuclei as a result from competition with other defect sinks. Third, when defect imbalance or injected interstitials are included into the picture, enhanced vacancy concentrations near the surface and enhanced interstitials concentrations near the projected range will further make pulsed effect more complicated.

Within the limited accuracy associated with only two data points, our observed swelling rate of ~0.3%/dpa for the defocused beam case for pure iron may or may not be consistent with the swelling rate of ~0.2%/dpa observed in neutron irradiated Fe-Cr binary alloys [23, 24]. It is probably unrealistic, however, to expect that pure iron and iron-chromium alloys must exhibit the same swelling rate. Several neutron irradiation studies have shown that chromium additions to pure iron initially cause a strong decrease of swelling [25-27], and one study showed that cold-worked pure iron swelled ~6% at only 3 dpa [28], a swelling rate of ~0.5%/dpa. In general, the available data shows that swelling in neutron irradiated pure iron is accelerated by cold-work and is also accelerated by irradiation at lower dpa rates [24-28]. For instance, Kuramoto notes that "~0.3% swelling was attained at ~1 dpa" in the JMTR reactor at 450°C, but the uncertainty on his dose level precludes a confident statement that his swelling rate was 0.3%/dpa [20].

Finally, the applicability of our results to other irradiation conditions is constrained by two limitations. First we irradiated at only one temperature and the behavior might change at other temperatures. Simonen [21] notes that as the temperature is increased near the peak swelling temperature, the differences in void swelling for raster speeds becomes larger, decreasing at temperatures beyond the peak void swelling temperature. Second it should be noted that our studies utilized relatively low rastering frequencies characteristic of pulsed fusion devices. However, many current ion irradiation

facilities use rastering at frequencies ranging from 200 to 2500 Hz. If we extrapolate the very slow rate of decline in swelling rate beyond ~1 Hz shown in Figure 8 to such high frequencies, it appears that the swelling rate might saturate at a rather low value. At this time, however, we have no confidence that our results can be extrapolated to such higher frequencies. Therefore the next round of studies will explore this frequency regime. Additionally, at this time our results are only applicable to pure iron and cannot be extrapolated to more complex alloys. Further studies are required to explore such extrapolations.

In summary, this study clearly shows that a significant effect of rastering frequency operates on void nucleation and growth in self-ion irradiated pure iron at 450°C, with rastering leading to reduction of swelling in comparison with irradiation using a defocused, static beam. When compounded with the defect imbalance effect there is a significant suppression of swelling with the net effect varying with depth from the ion-incident surface. In order to confidently use ion bombardment as a surrogate technique to replace neutron irradiation, it appears that a defocused beam should be used. The results of this study therefore support the no-raster recommendation of ASTM E521-77 in simulating neutron damage using ion bombardment.

References

1. F. A. Garner, "Radiation Damage in Austenitic Steels", in Konings, R.J.M., (ed.) Comprehensive Nuclear Materials, volume 4, (2012) pp. 33-95, Elsevier.
2. G. S. Was, (2007). Fundamentals of Radiation Materials Science: Metals and Alloys, Springer.
3. ASTM E521, 2009, "Standard Practice for Neutron Radiation Damage Simulation by Charged-Particle Irradiation," ASTM International, West Conshohocken, PA, DOI: 10.1520/E0521-96R09E01, www.astm.org
4. J. A. Sprague, F. A. Smidt, Jr., J. E. Westmoreland and P. R. Malmberg, NRL Memorandum 2555 (1972).
5. J. A. Sprague and F. A. Smidt. NRL Memorandum 2692 (1972).
6. A. Taylor, *et al*., ANL/CTR/TM-39, Argonne National Laboratory (1975).
7. J. F. Ziegler, M. D. Ziegler, J. P. Biersack. Nucl. Instr. Meth. Phys. Res. B 268 (2010) 1818-1823.
8. R. E. Stoller, M. B. Toloczko, G. S. Was, A. G. Certain, S. Dwaraknath, and F. A. Garner. Nucl. Instr. Meth. Phys. Res. B 310, 75-80.
9. G. Wulff. Zeitschrift fur Krystallographie und Mineralogie. 34 (1901) 449-530.
10. F.A. Garner. J. Nucl. Mater. 117, pp. 177-197.
11. L. Shao, C.-C. Wei, J. Gigax , A. Aitkaliyeva, D. Chen, B. H. Sencer, F. A Garner. J. Nucl. Mater. 453 (2014) 176-181.
12. D. L. Plumton and W. G. Wolfer. J. Nucl. Mater. 120 (1984) 245-253.
13. E. H. Lee, L. K. Mansur, and M. H. Yoo. J. Nucl. Mat. 85 & 86, 577 (1979).
14. D. L. Plumton, G. L. Kulcinski. J. Nucl. Mat. 133 & 134, 444 (1985).
15. L. K. Mansur and M. H. Yoo. J. Nucl. Mater. 85 & 86 (1979) 523-532.
16. D. B. Bullen, G. L. Kulcinski and R. A. Dodd. Nucl. Instr. Meth. Phys. Res. B 10/11 (1985) 561-564.
17. J. B. Whitley, G. L. Kulcinski, P. Wilkes, H. V. Smith Jr. J. Nucl. Mater. 79 (1979) 159-169.
18. D. L. Plumton, H. Attaya, W. G. Wolfer. J. Nucl Mater. 122 & 123 (1984) 650-653.
19. A. D. Brailsford and L. K. Mansur. J. Nucl. Mater. 71 (1977) 110-116.
20. E. Kuramoto, N. Yoshida, N. Tsukuda, K. Kitajima, N. Packan, *et al*. J. Nucl. Mater. 103 (1981) 1091-1096
21. N. Ghoniem and G. L. Kulcinski. J. Nucl. Mater. 69-70 (1978) 816-820.
22. E. P. Simonen, N. M. Ghoniem, and H. K. Packan. J. Nucl. Mater. 122 & 123 (1984) 391-401.
23. B. H. Sencer, F. A. Garner. J. Nucl. Mater. 283-287 (2000) 164.
24. F. A. Garner, M. B. Toloczko and B. H. Sencer. J. Nucl. Mater. 276 (2000) 123-142.

25. S. I. Porollo, A. M. Dvoriashin, A. N. Vorobyev, Yu. V. Konobeev. J. Nucl. Mater. 256 (1998) 47-253.
26. Yu. V. Konobeev, A. M. Dvoriashin, S. I. Porollo, and F. A. Garner. J. Nucl. Mater. 355 (2006) 124-130.
27. E. A. Little, D. A. Stow, in Proc. Int. Conf. on Irradiation Behaviour of Metallic Materials for Fast Reactor Core Components, Ajaccio, France 1979, pp. 17-24.
28. A. M. Dvoriashin, S. I. Porollo, Yu. V. Konobeev and F. A. Garner. J. Nucl. Mater. 283-287 (2000) 157-160.
29. N. I. Budylkin, E. G. Mironova and V. M. Chernov, V. A. Krasnoselov, S. I. Porollo and F. A. Garner. J. Nucl. Mater. 375 (2008) 359-364.

Research highlight #2

F-2 Establishment of correct procedures for ion irradiation testing: carbon contamination and solutions

Neutron-induced swelling in austenitic and ferritic steels is sensitive to the carbon level in the steel, as well as its distribution in matrix or precipitates. It recently become known that ion-irradiation to high dpa levels leads to a progressive increase in carbon concentration and precipitation within the ion range, with concurrent reductions in void swelling. This neutron-atypical phenomenon imperils the credibility of ion simulation for PWR applications. A series of experiments involving pure iron, and both model and commercial alloys, was conducted to identify the source and distribution of injected carbon. It was found that negatively-charged carbon atoms are entrained in the self-ion beam by a Coulomb drag effect, thereby delivered at low energy to the irradiated surface, followed by ion-beam-mixing and diffusion. A technique for filtering out contaminants was developed and resulted in higher swelling levels.

F2-1 Introduction

Studies on material degradation of structural alloys caused by neutron irradiation are critical for license extension of currently operating reactors and for design of various advanced reactor concepts [1-3]. For currently light water reactors (LWRs) the neutron exposure can induce damage in their austenitic structural alloys approaching 100 displacements per atom (dpa) over the 40 year license period [2]. Various advanced concepts based on fast reactors or accelerator-driven spallation reactors envision even higher target doses of 300-400 dpa and perhaps 500-600 dpa in some optimistic designs [3]. However, the highest attained doses to date are only ~200 dpa for a few ferritic-martensitic alloys [4,5]. To explore higher doses for a larger range of currently available or new alloys requires using ion accelerator for accelerated material screening and developments. Although defect morphologies caused by irradiation of different particle types and particle energies are different [6], there is a first-order-approximation to correlate radiation damage from different particles types through the use of the displacement-per-atom concept (dpa) [1]. Using self-ions of 3-5 MeV it is possible to achieve 1000 peak dpa during 7-10 days of continuous irradiation [7].

Correlation of ion-induced damage to that produced by neutrons requires that a number of neutron-atypical factors of ion irradiation be incorporated into the analysis, such as sputtering [8], internal gradients in dpa rates [9], atypical stress [10,11], dpa-rate-gradient induced segregation of elements [12-15], pulse beam effect [16-20], and local swelling suppression by injected interstitials at projected ranges of bombarding atoms [21-27].

However, one neutron-atypical issue has recently been recognized, arising from chemical modification during irradiation of the ion-damaged layer from elements that are introduced across the ion-incident surface, especially if the element is known to have a strong effect on void swelling. Carbon in particular is known to have a strong effect on void swelling in both austenitic and ferritic iron-base alloys [2-4,28]. The presence of carbon contamination is frequently evidenced by observations of a thin layer rich in carbon and oxygen that forms on the surface of ion-irradiated materials. For stainless steels, this layer is often accompanied by Cr-rich particle formation on the surface. Such contamination can obviously be reduced by maintaining a better vacuum. However, even with a target chamber vacuum better than 1×10^{-8} torr, problems often still exist, usually observed as a pale or dark-colored patina on the surface. In the 1970-1980s such discolorations were often observed in irradiations reaching perhaps ~100 dpa but their potential influence was not thought to be important. However, now that ion irradiations routinely reach ~1000 dpa the introduction of carbon especially cannot be casually dismissed.

There are a number of potential sources of carbon contamination, and the present study, together with two recent studies [29,30], are aimed to determine what is the major source so that it can be eliminated or strongly reduced. Previous studies show that the residual vacuum of an accelerator system includes traces of N_2, CO, N, H_2O, O_2, O, CH_4, OH, Ar, CO_2 and hydrocarbons [31]. Use of oil-free mechanical pumps and high vacuum turbo-pumps cannot completely avoid the presence such molecules [32]. Possible contaminant-releasing sources include all kinds of pumps, sealing materials, plastics, stripping gas, target refilling gas, and the stainless steel walls of the beam tube and target chamber. Improving the vacuum to the range of 1×10^{-7} torr to 1×10^{-8} torr in our studies and in other facilities does not appear to eliminate the problem. Adding a cold trap in the target chamber area is helpful but by itself cannot solve the issue as was observed in the present study. Blondiaux *et al.* proposed that the contamination comes from dissociation of volatile hydrocarbons in the volume near the target, with dissociation caused by interactions with secondary electrons emitted by the target [32]. This proposed mechanism, however, is difficult to reconcile with the insensitivity to the vacuum level of the carbon contamination.

There is an urgency to address the carbon contamination issue, specifically for accelerator-based ion irradiation testing of ferritic-martensitic iron base alloys where carbon can strongly affect the microstructural evolution. The issue is particularly severe for the current void swelling studies since high dose involves prolonged ion irradiation of 1-10 days or more at temperatures ranging from 300°C to 700°C. Such a long irradiation can induce significant deposition of carbon irradiation at elevated temperatures.

F2-2 Experimental procedure

In order to study this issue with a minimum of competing processes, we use pure iron to avoid many of the processes and complications that would occur in a more complicated alloy. High purity polycrystalline Fe (99.95%) and single crystal Fe (99.995%) were sectioned by electrical discharge machining into 1 mm disks, following by mechanical polishing with grade 600 to 1200 grit and then finally polishing using a 0.05 um colloidal silica and alumina solution to remove surface damage. Samples were irradiated with 3.5 MeV Fe ions at 475°C, using a 1.7 MV General Ionex Tandetron accelerator. To avoid beam pulsing beam effects, a defocused beam of 6 mm×6 mm was used [16]. All samples are irradiated to 100 dpa, defined at the peak damage depth using the SRIM code, choosing the modified Kinchin-Pease option and a displacement threshold energy of 40 eV [33]. Prior to ion irradiation, the target chamber was baked overnight. The vacuum in the target chamber during ion irradiation was maintained $<1\times10^{-8}$ torr.

Depth profiles of C, O, and Fe were obtained by using secondary ion mass spectrometry (SIMS). The data were acquired at EAG Laboratories (East Windsor, New Jersey) by using a Physical Electronics Model 6600 SIMS System with cesium primary ion bombardment at 4 keV. Negatively-charged secondary ions were detected. C concentration is determined through yield calibration using a standard C-implanted Fe sample.

F2-3 Carbon enrichment

Figure 1a shows the secondary ion mass spectrometry (SIMS) profile of carbon in unirradiated polycrystalline Fe. The C profile remains flat in the bulk region at a concentration about $1\times10^{19}/cm^3$. Figure 1b shows the carbon profile after 3.5 MeV Fe ion irradiation at 475°C in an accelerator with a target chamber vacuum of better than 1×10^{-7} torr but otherwise without any modifications to minimize carbon contamination. Ion irradiation induces carbon enrichment in the region up to about 1.2 μm, with its peak concentration about a factor of 6 higher than the background concentration. In the region

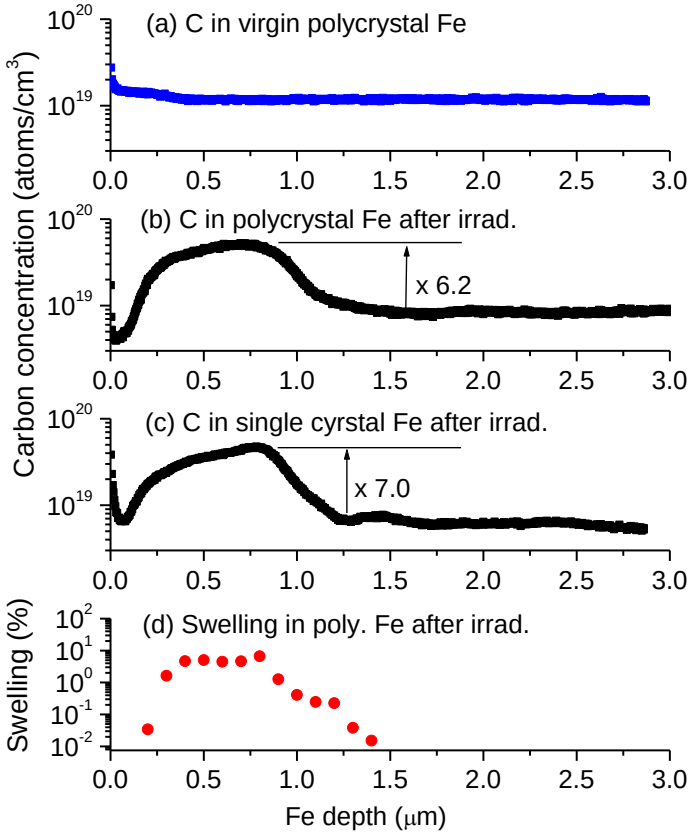

Figure 1. (a) SIMS C profile in unirradiated polycrystalline Fe, (b) C profile in irradiated polycrystalline Fe, (c) C profile in irradiated single crystal Fe, and (d) void swelling as a function of depth in polycrystalline Fe, measured from transmission electron microscopy characterization. C profiles follow void swelling distributions after Fe self-ion irradiation.

immediately beyond the enrichment region, the carbon concentration profile is relatively flat without any obvious sign of carbon depletion from the volume beyond the ion range.

Figure 1c shows the carbon profile in irradiated single crystal Fe. Similar enrichment in the irradiated region is observed. Different from the polycrystalline Fe specimen, the single crystal Fe has lower carbon background carbon concentration at about $5\times10^{18}/cm^3$ which reflects its higher initial purity. Note that a comparable carbon enrichment peak is observed at essentially the same depth as in the polycrystalline specimen.

Carbon distributions appear to agree with the void swelling profiles measured from transmission electron microscopy (TEM). Figure 1d plot the swelling profile in polycrystalline Fe after the irradiation. Significant swelling occurs in the depth region from about 300 nm to about 900 nm, which is also the region of significant carbon enrichment, as shown in Figs. 1b.

We believe that carbon enrichment in the near surface region comes from beam-induced contamination, but the deposited carbon probably does not arrive at energies sufficient to penetrate into the specimen. Instead, the deposited carbon atoms diffuse into the bulk and decorate open volume defects inside. Similar to other light elements, carbon atoms diffuse via an interstitial mechanism due to its smaller atomic radii [34,35]. It is well known that interstitial carbon atoms prefer to occupy octahedral

sites in both bcc and fcc iron [34,35]. The presence of an interstitial carbon atom leads to lattice expansion and a local strain field [36]. On other hand, vacancy defects created from ion irradiation induce local lattice relaxations and thereby attract and immobilize carbon atoms. Hence, it is not surprising that carbon atoms become fixed at open volume defects and therefore become enriched, decorating vacancies and voids, with the carbon distribution measured by SIMS correlating with the swelling profile.

F2-4 Carbon contamination mechanism

C atoms and other impurities in the beam tube can be either neutral, positive or negative, but we propose that contamination is caused by interactions of the positively charged Fe beam with negatively charged C ions. Positively charged C ions are mainly created from direct collisions of C atoms with beam particles, but the corresponding cross section is small. The negatively charged C ions are mainly created from interactions with secondary electrons in beam lines, which is believed to be significant considering the existence of high density electron cloud along beam lines. Such electron cloud is created first by beam interactions with accelerator inner components, and is then amplified through continuous secondary electron creation by electron interactions with tube walls. The existence of such electron cloud has been well known for causing beam instability in many accelerator facilities [37,38].

We believe the contamination is caused by long range Coulomb force interactions between Fe ions and carbon contaminants. Negatively-charged carbon atoms or carbon complexes within the beam volume experience a net drift down the beam line due to slight dragging forces imparted by Coulomb interactions every time a positive 3.5 MeV ion passes closely by a negative carbon atom or carbon complex. The drift energies of carbon along the beam axis are very small, resulting in deposition on the irradiated surface without significant penetration into the bulk. Molecular dynamics simulation has confirmed such small momentum transfers occurs to carbon contaminants [29].

Figure 2a shows that, with repeating 3.5 MeV Fe ion bombardments, carbon contaminants (originally randomly distributed within the simulation cell) began to be enriched in the Fe bombardment plane. Furthermore, as shown in Fig. 2b, the sum of carbon atoms' velocity close to the Fe bombardment plane changes from zero to negative values. Note that the negative velocity direction corresponds to Fe ion beam direction. These modeling studies suggest that that Coulomb interactions lead to a decoration of carbon cloud along the beam. Hence, the contamination is more like a directional contamination.

F2-5 A technique of multiple beam bending developed to remove carbon from the beam

We developed a technique of multiple beam bending to purify the Fe beam for relatively carbon-free ion irradiation. The design principle is rather simple: Due to differences in both mass/charge ratio and particle velocity, a magnetic or electronic field will bend carbon and Fe ions toward different directions. This technique is not limited to carbon atoms, since other contaminants such as O, N, H are residual gas atoms in an accelerator system, and these can be also effectively removed or minimized by this technique.

The deflectors used in this study are magnetic deflectors Model 2EA032940, manufactured by NEC Inc., and are driven by KEPCO bipolar power supplies Model BOP 36-12M. The technique includes the following key steps. First, the beam after passing the high energy magnet is intentionally bent away from the beam center-line (towards the left side of the chamber). After the first deflector, the beam is slightly bent towards the right side of the chamber. This first bending is able to filter out both C which is negatively charged and also any C-Fe molecules which are neutral (if by chance Fe and C form stable compound molecules). The charged C atoms have lower mass and higher charge-to-mass ratio, hence they are deflected further compared to the Fe beam and therefore carbon is deflected and easily filtered out of the beam. For neutral C-Fe molecules, they are insensitive to bending and will hit the beam lines. At the second deflector, the beam is bent towards the left side of the chamber and contaminated C atoms are again filtered out by the same mechanism. After the third deflector, C atoms created between the second

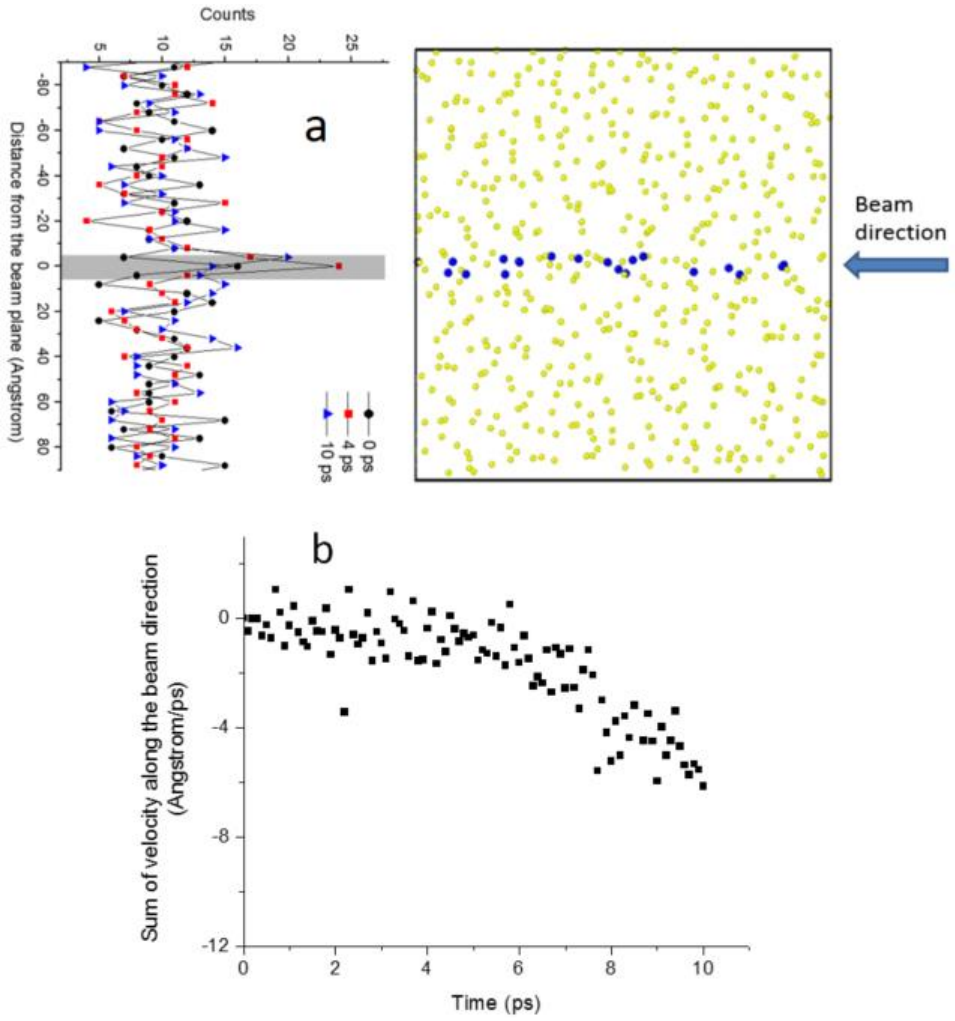

Fig. 2 (a) Counts of carbon atoms as a distance away from the plane which has repeated bombardments of 3.5 MeV Fe ions, and (b) the sum of velocities of carbon atoms close to the bombardment plane. Carbon atoms are randomly distributed in the simulation cell with random velocities corresponding to room temperature.

and third deflectors are filtered out again as the beam is bent to hit the sample. The last deflector needs to be positioned as close as possible to the target chamber to minimize new production of carbon atoms in that last segment of the flight path. This distance, however, cannot realistically be zero. To further reduce the possibility that the ion beam will again collect C atoms during the last flight segment, a liquid nitrogen trap is used to locally improve the vacuum and reduce the amount of carbon contamination.

F2-6 Demonstration of the effectiveness of the technique

Figure 3 compares the carbon profiles in 100 dpa irradiated Fe with or without beam deflection technique applied. Obviously the deflection technique is very efficient to reduce carbon contamination. The carbon concentration in the filtered irradiation is comparable to the background level before the irradiation. Still the carbon profile shows a small peak in the swelling region. Such carbon segregation

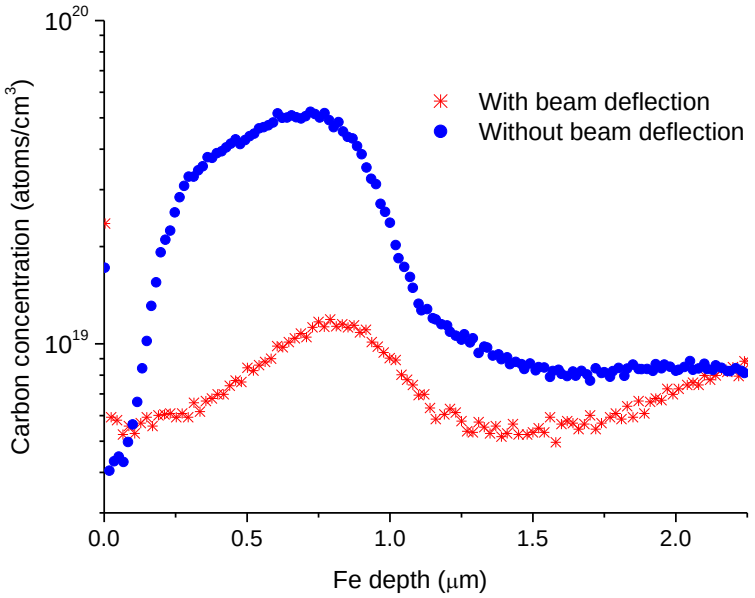

Figure 3 SIMS carbon profiles within the beam spot region after 100 peak dpa irradiation at 475°C, with or without applying the beam deflection technique.

can be caused by interaction of open volume defects with carbon atoms originally in Fe. Similar studies on HT-9 has found that not only carbon, but also oxygen and nitrogen contamination are greatly suppressed by the beam deflection technique [30].

In Fig. 3, C concentrations in the near surface regions (about 150 nm deep) of irradiated samples appear depleted with sharp gradients. This, however, is likely a SIMS artifact. C sensitivity in the near surface region is greatly affected in the presence of an oxide layer. We observed a thick oxide layer of about 100 to 150 nm thickness in the irradiated sample without beam deflection, and a relatively thin oxide layer of about 50 nm thickness if the beam deflection technique is applied. Surface oxygen promotes C+ yield and suppresses C- yield (which is what collected in SIMS analysis), leading to underestimated C concentrations in the region marked by shadowed boxes in Fig. 3.

F2-7 Discussion

Previous studies have suggested that carbon interactions can dramatically change defect kinetics. Due to carbon-vacancy interactions, the effective vacancy diffusivity becomes less than the intrinsic value [39] A small change in diffusivity is thought to dramatically change the evolution of microstructure under irradiation. Recent studies have shown that carbon contamination greatly suppresses void swelling in HT-9. Introducing extra carbon atoms leads to overestimation of swelling resistance, which is a critical issue for accelerator simulation of neutron damage.

We consider it unlikely that the beam contamination comes primarily from the ion source. Although C, H, O always occur at the very beginning of sputtering and beam transport in an ion source, such molecules are easily separable from the beam after beam bending by a low energy magnet. Note that both high energy and low energy magnets available for commercial accelerators have excellent mass resolution to easily differentiate isotopes of a given element. We were unable to find a C-Fe molecule which have

the same mass to charge ratio that of Fe. Furthermore, the contamination issue exists for all ion beam devices and is not unique for one particular ion specie. Hence, attention paid to changing of cathode material will most likely not solve the contamination problem.

The present study uses three beam deflectors. The number of beam deflectors can be reduced down to two or even one. Using less deflectors, however, it will be difficult to balance and reduce the distances between the high energy magnet and the target chamber. In order to minimize beam contamination along the last flight segment prior to entering the target chamber, the last deflector needs to be as close as possible to the chamber. On the other hand, if the deflector is far away from the high energy magnet, the maintenance of best beam optics is challenging in order to minimize beam dispersion. Adding multiple beam deflectors does not require modification of standard beam line configuration and the proposed technique should be feasible to apply to any system.

In summary, the proposed bending technique should be used as a standard for accelerator-based void swelling simulation in order to better correlate ion-generated data to neutron-generated damage.

References

1] Was, G.S. *Fundamentals of Radiation Materials Science: Metals and Alloys* (Springer, 2007).

[2] Garner, F. A. *Understanding and Mitigating Aging in Nuclear Power Plants* (ed Tipping, P.G) Ch. 10, 308-356 (Woodhouse, 2010).

[3] Garner, F.A. *Comprehensive Nuclear Materials Vol. 4* (ed Konings, R.J.M.), 33-95 (Elsevier, 2012).

[4] Toloczko, M. B., Garner, F. A., Eiholzer, C. R. Irradiation creep and swelling of the U.S. fusion heats of HT9 and 9Cr-1Mo to 208 dpa at ~400°C, *J. Nucl. Mater.* **212-215,** 604-607 (1994).

[5] Gelles, D. S. Microstructural development in reduced activation ferritic alloys irradiated to 200 dpa at 420°C, *J. Nucl. Mater.* **212-215,** 714-719 (1994).

[6] Greenwood, L. R. Neutron interactions and atomic recoil spectra, *J. Nucl. Mat.* **216**, 29-44(1994).

[7] Gigax, J.G. et al. Void swelling of self-ion-irradiated T91 at damage levels up to 1000 peak dpa, *J. Nucl. Mat.* submitted.

[8] Wang, J. et al. Modification of SRIM-calculated dose and injected ion profiles due to sputtering, injected ion buildup and void swelling, 387, 20-28 (2016)

[9] Garner, F.A., Guthrie, G.L. Radiation effects and tritium technology for fusion reactors, CONF-750989, Vol. **I**, pp. 491–518.

[10] Garner, F.A., Wire, G.L., Gilbert, E.R. Radiation effects and tritium technology for fusion reactors, CONF-750989, vol. **I**, pp. 474–490.

[11] Wolfer, W.G., Garner, F.A. Swelling-induced stresses in ion-bombarded surfaces: Effect of crystalline orientation, *J. Nucl. Mater.* **85-86**, 583-589 (1979).

[12] Sethi, V.K., Okamoto, P.R. Conference on phase stability during irradiation, The Metallurgical Society of AIME, Pittsburgh, PA, pp. 109-117 (1980).

[13] Pechenkin, V.A., Chernova, A.D., Garner, F.A. Modeling of local changes in composition of alloys along the projected range under heavy ion irradiation, Proceedings of AccApp 2013, Bruges, Belgium.

[14] Pechenkin, V.A., Chernova, A.D., Molodtsov, V. L., Garner, F.A. Effect of internal sink strength on diffusion mass transport in alloys under high dose ion irradiation, Proceeding of AccApp 2015, Washington, DC., in press.

[15] Vortler, K. et al. Simulated spatial and temporal dependence of chromium concentration in pure Fe and Fe-14%Cr under high dpa ion irradiation, *J. Nucl. Mater.* **479**, 23-35 (2016).

[16] Gigax, J.G. et al. The influence of ion beam rastering on the swelling of self-ion irradiated pure iron at 450° C, *J. Nucl. Mat.* **465**, 343-348 (2015).

[17] ASTM E521, Standard practice for neutron radiation damage simulation by charged-particle irradiation, ASTM International, West Conshohocken, PA (2009).
[18] Ghoniem, N., Kulcinski, G.L. Swelling of metals during pulsed irradiation, *J. Nucl. Mater.* **69–70**, 816-820 (1978).
[19] Getto, E., Jiao, Z., Monterrosa, A.M., Sun, K., Was, G.S. Effect of irradiation mode on the microstructure of self-ion irradiated ferritic-martensitic alloys, *J. Nucl. Mater.* **465**, 116-126 (2015).
[20] Simonen, E.P., Ghoniem, N.M., Packan, N.H. Pulsed flux effects on radiation damage, *J. Nucl. Mat.* **122,** 391-401 (1984).
[21] Shao, L. et al. Effect of defect imbalance on void swelling distributions produced in pure iron irradiated with 3.5 MeV self-ions, *J. Nucl. Mat.* **453**, 176-181 (2014).
[22] Garner, F.A. Impact of the injected interstitial on the correlation of charged particle and neutron-induced radiation damage, *J. Nucl. Mater.* **117**, 177-197 (1983).
[23] Lee, E.H., Mansur, L.K., Yoo, M. H., Spatial variation in void volume during charged particle bombardment — the effects of injected interstitials, *J. Nucl. Mater.* **85-86**, 577-581 (1979).
[24] Plumton, D.L., Kulcinski, G.L. The magnitude and distribution of the excess interstitial fraction during heavy ion irradiation, *J. Nucl. Mater.* **133-134**, 444-447 (1985).
[25] Mansur, L.K., Yoo, M.H. Advances in the theory of swelling in irradiated metals and alloys, *J. Nucl. Mater.* **85-86**, 523-532 (1979).
[26] Plumton, D.L., Attaya, H., Wolfer, W. G. Conditions for the suppression of void formation during ion-bombardment, *J. Nucl Mater.* **122-123**, 650-653 (1984).
[27] Brailsford, A.D., Mansur, L.K. Effect of self-ion injection in simulation studies of void swelling, *J. Nucl. Mater.* **71,** 110-116 (1977).
[28] Sencer, B.H., Garner, F.A. Compositional and temperature dependence of void swelling in model Fe-Cr base alloys irradiated in EBR-II, *J. Nucl. Mater.* **283-287**, 164-168 (2000).
[29] Shao, L., Gigax, J., Chen, D., Kim, H., Garner, F.A., Wang, J., Toloczko, M.B., Standardization of accelerator irradiation procedures for simulation of neutron induced damage in reactor structural materials, *Nucl. Instrum. Methods Phys. Res. B*, in press.
[30] Gigax, J.G., Kim, H., Aydogan, E., Garner, F.A., Maloy, S., Shao, Beam-contamination-induced compositional alteration and its neutron-atypical consequences in ion simulation of neutron-induced void swelling, *Mat. Res. Lett*., in press.
[31] Healy, M.J.F. Minimising carbon contamination during ion beam analysis, *Nucl. Instrum. Methods in Phys. Res.* **B 129**, 130-136 (1997).
[32] Blondiaux, G., Valladon, M., Quaglia, L., Robaye, G., Weber, G., Debrun, J.L. Study of the growth of carbon on targets during ion bombardment, *Nucl. Instr. and Meth. in Phys. Res*, **227,** 19-23 (1984).
[33] Biersack, J., Haggmark, L.G. A Monte Carlo computer program for the transport of energetic ions in amorphous targets, *Nucl. Instru. Method. Phys. Res. B* **174**, 257-276 (1980).
[34] Butler, B.D., Cohen, J.B. What the latest diffraction techniques can tell us about an old material: Steel, *Ultramicroscopy* **52,** 238–242 (1993).
[35] Jiang, D.E., Carter, E.A. Carbon dissolution and diffusion in ferrite and austenite from first principles, *Phys. Rev. B*, **67,** 214103–214113 (2003).
[36] Huang, L., Skorodumova, N.V., Belonoshko, A.B., Johansson, B., Ahuja, R. Carbon in iron phases under high pressure, *Geophysical Research Letters* **32,** L21314 (2005).
[37] Keil, E., Zotter, B. Landau-damping of coupled E-P oscillations, CERN Report CERNISR-TH/71-58, 1971.
[38] Neuffer, D. et al. Observations of a fast transverse instability in the PSR, *Nucl. Instrum. Methods in Phys. Res.* A, **321,** 1-12 (1992).
[39] Short, M.P., Gaston, D.R., Jin, M., Shao, L., Garner, F.A. Modeling injected interstitial effects on void swelling in self-ion irradiation experiments, *J. Nucl. Mat.* **471**, 200-207 (2016).

Research highlight #3

F-3 Radiation response of oxide-dispersion-strengthened alloy MA 956 after self-ion irradiation

We studied the radiation-induced microstructural evolution of an oxide-dispersion-strengthened (ODS) ferritic alloy, MA956, to 180 dpa using 3.5 MeV Fe2+ ions. Post-irradiation examination showed that voids formed rather early and almost exclusively at the particle-matrix interfaces. Surprisingly, voids formed even in the injected interstitial zone. Comparisons with studies on other ODS alloys with smaller and largely coherent dispersoids irradiated at similar conditions revealed that the larger and not completely coherent oxide particles in MA956 serve as defect collectors which promote nucleation of voids at their interface. The interface configuration, which is related to particle type, crystal structure and size, is one of the important factors determining the defect-sink properties of particle-matrix interfaces.

F3-1 Introduction

Oxide-dispersion-strengthened (ODS) ferritic-martensitic steels are being considered as candidate materials for advanced nuclear reactors primarily because of their superior high temperature creep resistance and improved strength and radiation tolerance compared to traditional ferritic-martensitic steels [1-4]. Recent studies have shown that oxide particles embedded in the matrix may also benefit the overall radiation tolerance of the alloy by providing additional defect-trapping sites for both point defects and helium at particle-matrix interfaces, thereby reducing void swelling [3–8]. However, there are very limited results showing direct evidence of oxide particle-defect interactions. Most ODS alloys examined to date are nano-structured and therefore contain a high density of grain boundaries (GBs) that strongly interact with the radiation-induced defects [3, 8-11], thus camouflaging the role played by the oxide particles in interacting with point defects.

In this study, we used the ferritic ODS alloy MA956 with rather large grains and a low density of GBs to reduce the GB contribution to total defect annihilation [9-11]. We used self-ion irradiation, an increasingly well-understood technique that has been applied to nuclear material research for decades [12–16]. We investigated the radiation response of this alloy to acquire evidence of particle-defect interactions and to illuminate the mechanisms involved.

F3-2 Experimental procedures

MA956 was received in final form from Special Metals Corporation with composition given in Table 1. It was sectioned into 2 mm disks that were successively ground with 600, 800 and 1200 grade grit and then finally polished with 50 nm colloidal silica and alumina solution. The disks were then irradiated at 450 °C with 3.5 MeV Fe2+ ions to 60, 120, and 180 peak displacements per atom (dpa), using rastered beam at 15.63 and 0.156 Hz in X and Y directions, respectively. The peak dpa rate was in the order of 10-3 dpa/sec. No gas injection was employed in this study. The profiles for atomic displacement and injected Fe distributions for pure Fe were employed, calculated using the SRIM code [17]. These calculations assumed a displacement energy of 40 eV and used the Kinchin-Pease option to provide a damage estimate comparable to that of neutron irradiation [18, 19].

TEM samples were prepared using a FEI Quanta 3D FEG dual beam secondary-electron-microscope (SEM)/ focused-ion-beam (FIB) system. Cross-sectional samples were lifted-out from the irradiated surfaces, therefore exhibiting a dpa-depth dependence along their length. A FEI TECNAI F20 SUPERTWIN transmission electron microscope (TEM) with energy dispersive X-ray spectroscopy (EDS)

and electron energy-loss spectroscopy (EELS) applications was used. The microstructural development was observed using conventional bright-field TEM. EDS and EELS were used to characterize the microchemistry and thickness of the samples, respectively. The thickness of the TEM samples is typically about 100 nm.

The sizes of grains in this MA956 variant are on the order of millimeters, much larger than the typical FIB size of ~10 × 10 μm. Multiple samples were lifted-out and showed that the variance in microstructure between different grains is minimal. As shown in both previous and current studies, TEM investigations on FIB samples of ferritic-martensitic alloys provide good statistics to demonstrate effects of radiation on microstructural evolution, especially for void formation and growth, as well as changes to nano-particles [3, 20-22].

F3-3 Results and Discussion

Fig. 1 (a) shows the microstructure of MA956 before irradiation. The dark circular features are oxide particles appearing in different contrasts that we attribute to differences in particle-matrix orientations. Most of nano-particles were found to have a diameter less than 60 nm, with a mean diameter of ~18 nm. EDS investigations show that the particles are Y-Al-O rich. Some particles larger than 200 nm exist, with compositions typical of either aluminum oxide or titanium carbide. The density of all nano-particles is 2.7 ± 0.3 × 1015 *cm*-3.

Figs. 1(b-d) show the microstructures of the self-ion-irradiated samples with peak damage levels of 60, 120 and 180 dpa, respectively, with the ions entering from the left. The most significant change induced by irradiation are voids growing exclusively on the particle-matrix interface and possibly growing into both the matrix and the oxide particles. No voids appear to be free of particles. A similar linkage between voids and precipitates in austenitic steels was labeled by Mansur et al. as the "precipitate collector" effect [23-25].

The sizes and densities of voids appear to increase with dose. In Fig. 1(d), large voids formed near a depth of 1000 nm where the dpa reaches its maximum as shown by the superimposed damage profile represented by the solid line. The dashed line in Fig. 1(d) represents the distribution of injected interstitials known to suppress void formation through the defect imbalance effect [12, 14]. Unlike most ferritic alloys where voids are totally absent in the injected interstitial zone, Fig. 1(d) shows there are voids observed between 1000 to 1200 nm where the density of injected interstitials is high, but they are generally smaller compared to those formed between 800 to 1000 nm, where the density of injected interstitials is relatively low. The irradiation also led to an increased dislocation density in the matrix, as seen in Figs. 4b-d and the insert in Fig. 1c. The oxide particles in the present study are not effective in enhancing interstitial-vacancy recombination.

Figs. 2(a) and (b) present void swelling and void densities as a function of depth for the irradiated samples, showing that both the volume fractions of the voids and the position of peak void swelling increase with dpa. This phenomenon has been observed in other ODS and non-ODS ferritic-martensitic alloys when irradiated by self-ions [3,10-12, 21, 22]. The defect imbalance effect and the “internal temperature shift” due to the relatively large variation in the dpa rate over the ion range have been

Table 1: Nominal composition of MA956 ODS from Special Metals Corporation (at. %)

Fe	Cr	C	Si	Mn	Ni	Al	Cu	P	S	Ti	Y2O3
Bal.	19.4	0.02	0.04	0.1	0.05	4.8	0.02	0.01	0.008	0.38	0.51

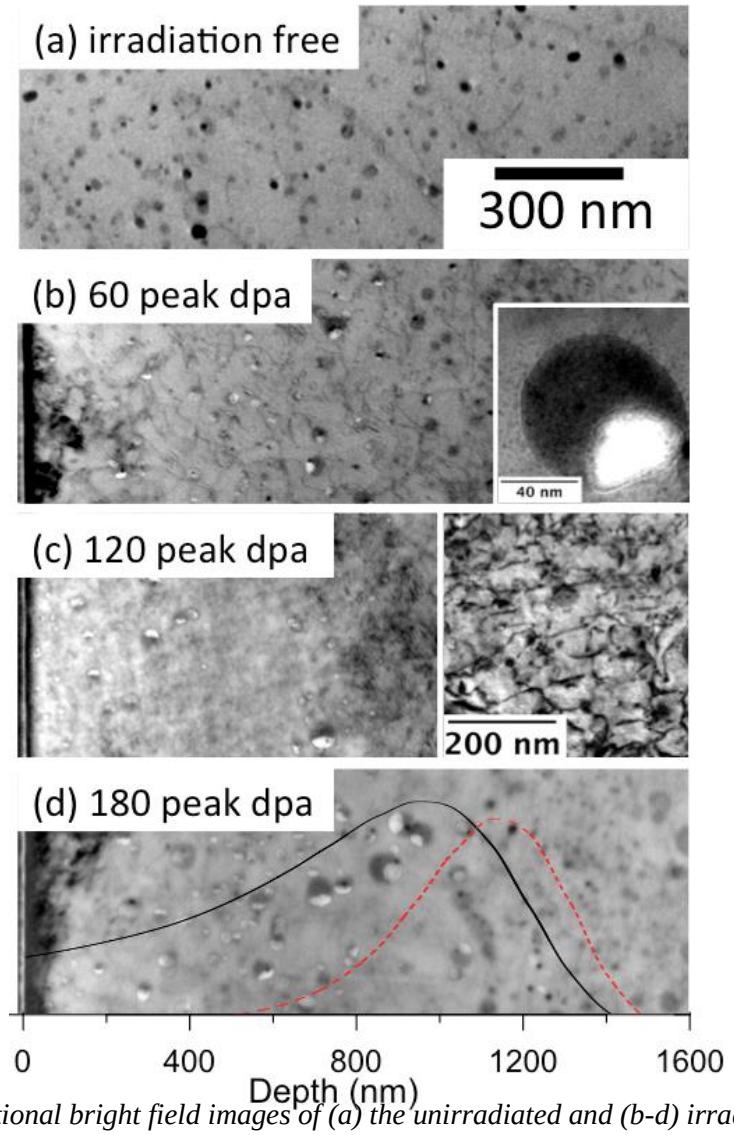

Figure 1 Conventional bright field images of (a) the unirradiated and (b-d) irradiated specimens with 60, 120 and 180 dpa damage peaks, respectively, showing that essentially all voids are associated with oxide particles. The insert in (b) shows a void formed on the side of an oxide particle in the 60 peak dpa sample. Note that the insert also shows a cloud of small precipitates surrounding the particle that was probably formed by recoil dissolution and reprecipitation. The insert in (c) shows the irradiation-induced dislocation network at the depth of 1000 nm in the 120 peak dpa sample. The lines superimposed on (d) are the calculated dpa and injected interstitial profiles as a function of depth.

invoked to explain the shape of these distributions [14, 26]. Void swelling from the depth interval of 600 to 1000 nm was used to produce Fig. 2(c), a plot of void swelling as a function of the average dpa level in that interval. Fig. 2(b) shows that specimens at 120 and 180 peak dpa have higher void densities than the 60 peak dpa sample, indicating nucleation of new voids with increasing damage. On the other hand, from 120 to 180 peak dpa, the changes in void density are not as significant, suggesting that from 120 to 180 peak dpa, the growth of existing voids plays the most important role in increasing swelling.

Fig. 2d shows the density and diameter profiles of oxide particles for the 180 peak dpa sample, solid and empty circles, respectively. The density of oxide particles slightly reduced in the irradiated region, as compared with that beyond the project range of the iron ions, illustrating the instability of oxide particles under irradiation. The diameter of the oxide particles increased within the project range. Comparison between Fig. 2a and 2d shows that particle size changes are correlated with the swelling and both have similar trends. This is because the voids were attached to the oxide particles and made contribution to the as-measured diameters of the particles.

It is important to note that the maximum densities of voids in the 120 and 180 peak dpa samples are close to the density of oxide particles. Close examination of the micrographs shown in Fig. 4 shows that essentially all the voids appear to have nucleated on the particle-matrix interface. Thus, it is believed that the oxide particles provide nucleation sites for voids and operate as biased defect sinks [23, 24]. In fact, because of the oxide particles serving as biased defect sinks, the injected ions do not as effectively suppress swelling as would be expected without the oxides or with neutral defect sinks. As shown in Fig. 2(a), the locations of peak swelling, which are shallower than the peak dpa at 1000 nm, progress deeper with increasing dpa, reflecting the effects of defect imbalance and gradients in dpa rate [14, 26]. At a given dpa level, however the locations of the peak swelling from the irradiating surface in this study are much deeper compared with other body-centered cubic (bcc) metals irradiated by self-ions of the same energy and at similar temperatures [3, 10, 15, 21].

Previous studies have suggested that oxide particles, especially those that are coherent with the matrix, can enhance swelling resistance [3, 6, 8]. The specific behavior of oxide particles in MA956 to enhance void nucleation even in the injected interstitial zone therefore requires some explanation. The obvious starting point is to examine the nature of the dispersoids in MA956 that are different from those in other alloys.

High resolution images of the oxide particles were obtained and analyzed, as shown in Fig. 3. The fast-Fourier-transform (FFT) pattern inserted in Fig. 3(a) suggests that the oxide particle possess a monoclinic crystal structure of $Y4Al2O9$ (YAM) with the FFT pattern corresponding to the [27-1] zone-axis of the YAM. The YAM (-115) and the bcc (101) shares the same spot in the FFT pattern, indicating that the (-115) plane of the YAM particle aligns with the (101) plane of the bcc. This coherence relationship is also shown in the inverse FFT image of Fig. 3(b). On the other hand, not all of the interface is coherent, Fig. 3(c) shows an incoherent part of the interface. The semi-coherency is a result of relaxing of the elastic energy arising from the strain at the coherent interface. Larger particles have higher strain energy at the coherent interface and tend to lose coherency for minimization of free energy[3, 6, 27]. In this study, the compressive strain in the YAM at the coherent $(-115)_{YAM}$ // $(101)_{bcc}$ interface is approximately 7 %.

It is well known that a compressive strain leads to a vacancy bias for defect collection at particle-matrix interfaces [25, 28]. In MA956, the size of the oxide particles is considerably larger than that for many other ODS alloys, leading to higher strain energy at the interfaces and thus a stronger vacancy bias. As a result, the oxide particles can serve as nucleation sites for voids. Meanwhile, the irradiation-induced dislocation network as seen in Fig. 4 might result from interstitials clustering. In general, the misfit between the oxide particles and the matrix is influenced by the type and crystal structure of the oxide particles. The level of strain is correlated to the size of the oxide particles. Thus, ODS alloys with other types of dispersions and/or finer particles do not often show the defect collection effect seen in this study.

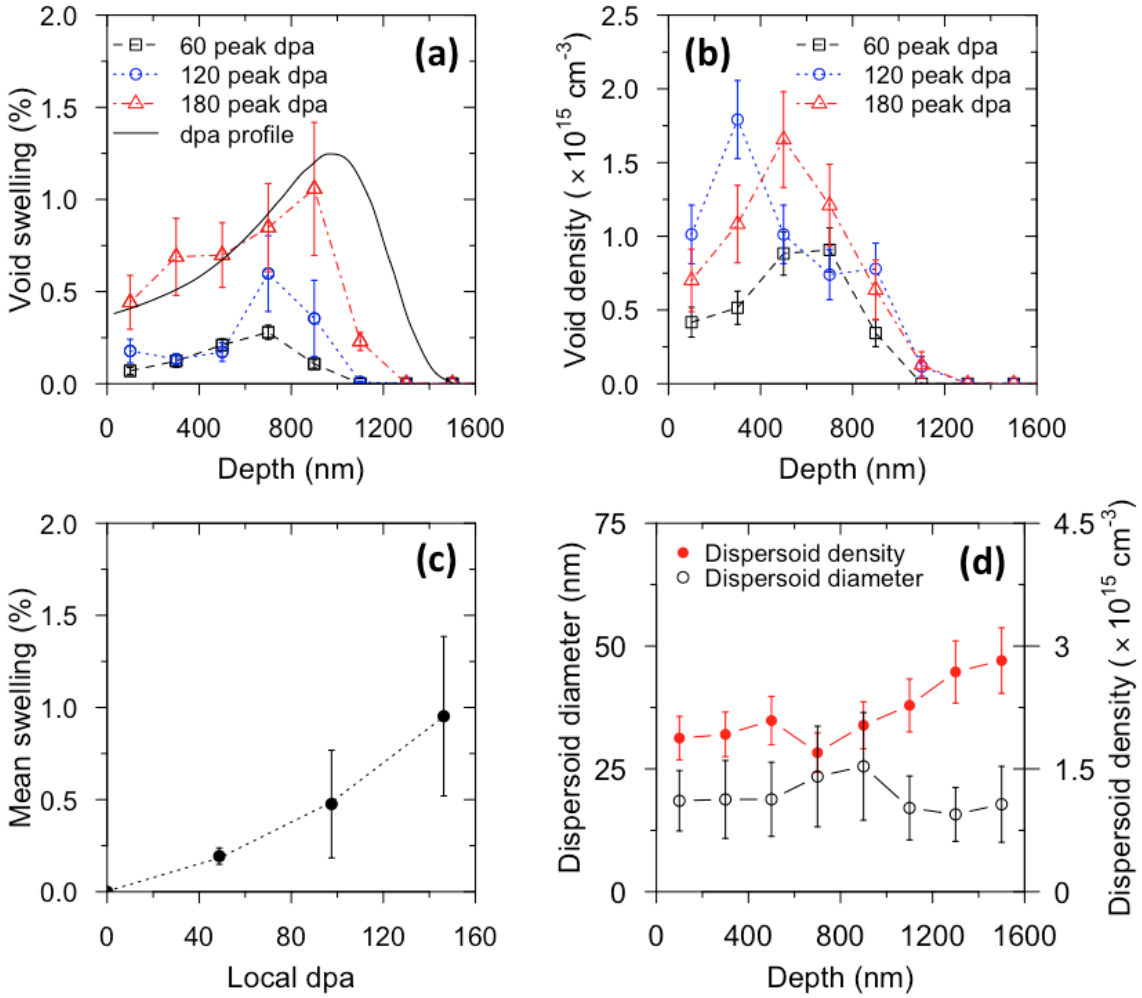

Figure 2: (a) Void swelling as a function of depth of 60, 120 and 180 peak dpa with the dpa depth profile superimposed, (b) void densities as a function of depth at 60, 120 and 180 peak dpa, (c) void swelling as a function of dpa using swelling data extracted from 600 to 1000 nm in depth, (d) density and diameter profiles as a function of depth of the oxide particle for the 180 peak dpa sample, shown in solid and empty circles, respectively.

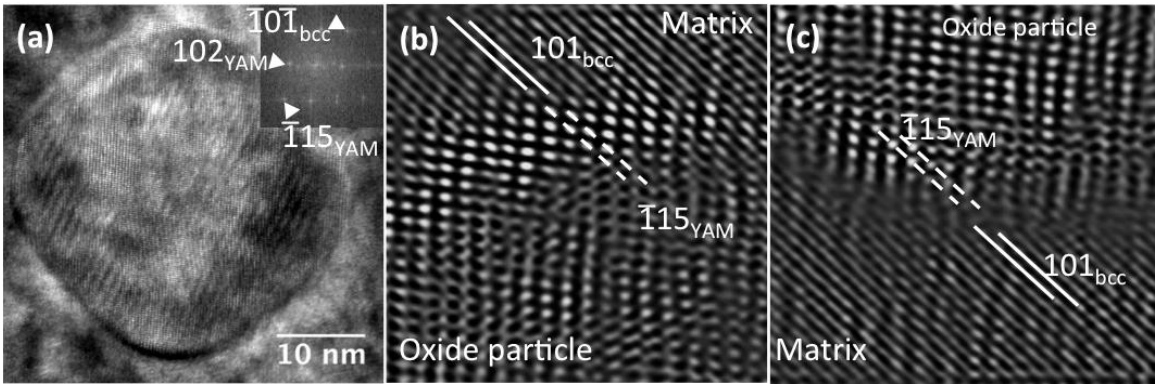

Figure 3 (a) A high-resolution micrograph showing a semi-coherent oxide particle from irradiation-free region, (b-c) inverse FFT images showing the coherent and incoherent particle-matrix interfaces, respectively

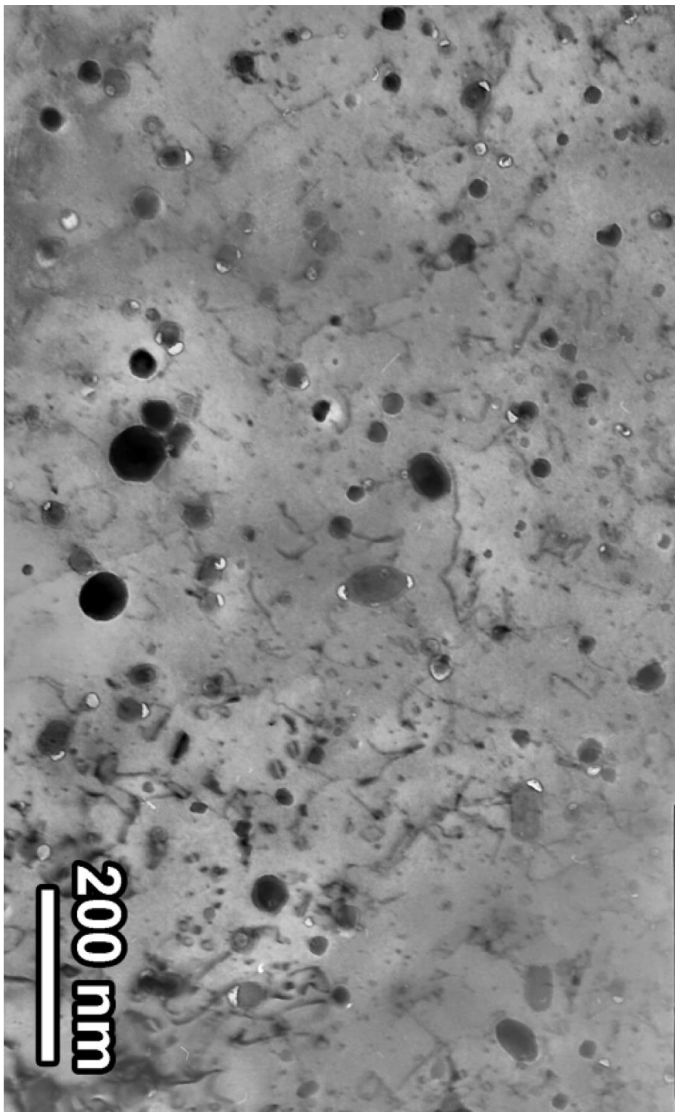

Figure 4 Another heat of MA956 irradiated with a non-rastered defocused beam of 1.8 MeV Cr ions to 100 local dpa at 450°C and 1x10-2 dpa/sec. Micrograph was supplied in advance of publication by V.N. Voyevodin of Kharkov Institute of Physics and Technology [29].

It should be noted that the particle-void association behavior of this alloy has been independently observed in the Ukraine, as shown in Fig. 7, even though the irradiation was conducted at a higher dpa rate using a non-rastered beam with a different ion and ion energy [29]. Therefore, the particle-void association behavior can be considered to be rather reproducible.

Finally, it should be noted that these large dispersoids are not completely stable under irradiation, as illustrated by the dispersoid density profile presented in Fig. 2d. In addition, as shown the inset of Fig. 4b, the large particle is surrounded by a cloud of smaller precipitates, most likely resulting from recoil dissolution at the particle interface and subsequent reprecipitation in the nearby matrix.

References

[1] L.K. Mansur, A.F. Rowcliffe, R.K. Nanstad, S.J. Zinkle, W.R. Corwin, R.E. Stoller, Materials needs for fusion, Generation IV fission reactors and spallation neutron sources-similarities and differences, Journal of Nuclear Materials 329–333 (2004) 166–172.

[2] Y. Gan, K. Mo, D. Yun, D.T. Hoelzer, Y. Miao, X. Liu, K.-C. Lan, J.-S. Park, J. Almer, T. Chen, H. Zhao, Temperature effect of elastic anisotropy and internal strain development in advanced nanostructured alloys: An *in-situ*synchrotron X-ray investigation, Materials Science and Engineering: A, 692 (2017) 53-61.

[3] T. Chen, E. Aydogan, J.G. Gigax, D. Chen, J. Wang, X. Wang, S. Ukai, F.A. Garner, L. Shao, Microstructural changes and void swelling of a 12Cr ODS ferritic-martensitic alloy after high-dpa self-ion-irradiation, Journal of Nuclear Materials 467 (2015) 42–49.

[4] K. Mo, D. Yun, Y. Miao, X. Liu, M. Pellin, J. Almer, J.S. Park, J.F. Stubbins, S. Zhu, A.M. Yacout, Investigation of High-Energy Ion-Irradiated MA957 Using Synchrotron Radiation under In-Situ Tension, Materials 9 (2016) 15

[5] D. Menut, J.-L. Béchade, S. Cammelli, S. Schlutig, B. Sitaud, P.L. Solari, Synchrotron radiation investigations of microstructural evolutions of ODS steels and Zr-based alloys irradiated in nuclear reactors, J. Mater. Res. 30 (9) (2015) 1392–1402.

[6] T. Chen, J.G. Gigax, L. Price, D. Chen, S. Ukai, E. Aydogan, S. Maloy, F.A. Garner, L. Shao, Temperature dependent dispersoid stability in ion-irradiated ferritic-martensitic dual-phase oxide-dispersion-strengthened alloy: coherent interfaces vs. incoherent interfaces, Acta Materialia 116 (2016) 29–42.

[7] J. Chen, P. Jung, W. Hoffelner, H. Ullmaier, Dislocation loops and bubbles in oxide dispersion strengthened ferritic steel after helium implantation under stress, Acta Materialia 56 (2008) 250–258.

[8] M.B. Toloczko, F.A. Garner, V.N. Voyevodin, V.V. Bryk, O.V. Borodin, V.V. Mel'nychenko, A.S. Kalchenko, Ion-induced swelling of ODS ferritic alloy MA957 tubing to 500 dpa, Journal of Nuclear Materials 453 (2014) 323–333.

[9] D. Chen, J. Wang, T. Chen, L. Shao, Defect annihilation at grain boundaries in alpha-Fe, Scientific reports 3 (1450).

[10] E. Aydogan, T. Chen, J. G. Gigax, D. Chen, X. Wang, P. S. Dzhumaev, O. V. Emelyanova, M.G. Ganchenkova, B.A. Kalin, M. Leontiva-Smirnova, R.Z. Valiev, N.A. Enikeev, M.M. Abramova, Y. Wu, W.Y. Lo, Y. Yang, M. Short, S.A. Maloy, F.A. Garner, L. Shao, Effect of self-ion irradiation on the microstructural changes of alloy EK-181 in annealed and severely deformed conditions, Journal of Nuclear Materials 487 (2017) 96-104.

[11] J.G. Gigax, H. Kim, T. Chen, F. A. Garner, L. Shao. Radiation instability of equal channel angular extruded T91 at ultra-high damage levels. Acta Materialia (2017) in press, https://doi.org/10.1016/j.actamat.2017.04.038

[12] F.A. Garner, Impact of the injected interstitial on the correlation of charged particle and neutron-induced radiation damage, Journal of Nuclear Materials 117 (1983) 177–197.

[13] G.S. Was, Fundamentals of radiation materials science: metals and alloys, Springer, 2007.

[14] L. Shao, C. Wei, J.G. Gigax, A. Aitkaliyeva, D. Chen, B.H. Sencer, F.A. Garner, Effect of defect imbalance on void swelling distributions produced in pure iron irradiated with 3.5 MeV self-ions, Journal of Nuclear Materials 453 (2014) 176–181.

[15] J.G. Gigax, E. Aydogan, T. Chen, D. Chen, Y. Wu, W. Lo, Y. Yang, F.A. Garner, The influence of beam rastering on the swelling of self-ion irradiated pure iron at 450 ∘C, Journal of Nuclear Materials 465 (2015) 343–348.

[16] E. Getto, Z. Jiao, A.M. Monterrosa, K. Sun, G.S. Was, Effect of irradiation mode on the microstructure of self-ion irradiated ferritic-martensitic alloys, Journal of Nuclear Materials 465 (2015) 116–126.

[17] J.F. Ziegler, J.P. Biersack, SRIM-2003 Program.

[18] L.R. Greenwood, R.K. Smither, SPECTER: neutron damage calculations for materials irradiations, Tech. Rep. ANL/FPP/TM-197, Argonne National Laboratory, Lemont, IL (1985).

[19] R.E. Stoller, M.B. Toloczko, G.S. Was, A. Certain, S. Dwaraknath, F. Garner, On the use of SRIM for computing radiation damage exposure, Nuclear Instruments and Methods in Physics Research B 310 (2013) 75–80.

[20] E. Aydogan, N. Almirall, G.R. Odette, S.A. Maloy, O. Anderoglu, L. Shao, J.G. Gigax, L. Price, D. Chen, T. Chen, F.A. Garner, Y. Wu, P. Wells, J.J. Lewandowski, D.T. Hoelzer, "Stability of nanosized oxides in ferrite under extremely high dose self ion irradiations" Journal of Nuclear Materials 486 (2017) 86-95.

[21] J.G. Gigax, T. Chen, H. Kim, J. Wang, L. Price, E. Aydogan, S.A. Maloy, D.K. Schreiber, M.B. Toloczko, F.A. Garner, L. Shao, Radiation response of alloy T91 at damage levels up to 1000 peak dpa, Journal of Nuclear Materials 482 (2016) 257–265.

[22] E. Getto, K. Sun, A.M. Monterrosa, Z. Jiao, M.J. Hackett, G.S. Was, Void swelling and microstructure evolution at very high damage level in self-ion irradiated ferritic-martensitic steels, Journal of Nuclear Materials 480 (2016) 159–176.

[23] L.K. Mansur, Theoretical evaluation of a mechanism of precipitate-enhanced cavity swelling during irradiation, Philosophical Magazine A 44 (1981) 867-877.

[24] E.H. Lee, L.K. Mansur, Relationships between Phase Stability and Relationships between phase stability and void swelling in Fe-Cr-Ni alloys during irradiation, Metallurgical and materials transactions A 23A (1992) 1977–1986.

[25] E.H. Lee, A.F. Rowcliffe, L. Mansur, Precipitation and cavity formation in austenitic stainless steels during irradiation, Journal of Nuclear Materials 103-104 (1981) 1475–1480.

[26] F.A. Garner, G.L. Guthrie, Influence of displacement gradients on the interpretation of charged particle simulation experiments, in: J.S. Watson, F.W. Wiffen (Eds.), Radiation effects and tritium technology for fusion reactors, Vol. I, 1976, p. 491.

[27] Y. Miao, K. Mo, B. Cui, W. Chen, M.K. Miller, K.A. Powers, V. McCreary, D. Gross, J. Almer, I.M. Robertson, J.F. Stubbins, The interfacial orientation relationship of oxide nanoparticles in a hafnium-containing oxide dispersion-strengthened austenitic stainless steel, Materials Characterization 101 (2015) 136–143.

[28] R.E. Stoller, G.R. Odette, The effect of helium on swelling in stainless steel: Influence of cavity density and morphology, in: Effects of Radiation on Materials, ASTM International, 1982. DOI: 10.1520/STP34351S

[29] V. Voyevodin, A. Kalchenko, Y. Kupriiyanova, A. Nikitina, M. Leonteva-Smirnova, V. Ageev, F.A. Garner, M.B. Toloczko, D.T. Hoeltzer, S.A. Maloy, The role of dispersoids in determining the swelling resistance of various reactor structural alloys during ion irradiation to 500 dpa, presented at NuMat 2016, Le Corum, Montpellier, France, Nov.7-10, 2016.

Research highlight #4

Dispersoid stability in ion irradiated ODS alloy: matrix effect (ferritic vs. martensitic)

In study, we have shown that a dual-phase 12Cr oxide-dispersion-strengthened (ODS) alloy, with improved corrosion and oxidation resistance exhibits promising void swelling resistance and microstructural stability under Fe^{2+} ion irradiation to 800 dpa at 475 ∘C. Dispersoids were originally present in both ferrite and tempered martensite grains, with the latter having a wider range of dispersoid sizes. In both phases dispersoids > 10 nm in diameter are incoherent with the matrix, while smaller dispersoids are coherent. During irradiation the larger incoherent dispersoids shrank and disappeared. Beyond 60 dpa dispersoids in both phases approached a near-identical equilibrium size of ~2-2.5 nm, which appears to be rather independent of local displacement rate. Grain morphology was found to be stable under irradiation. Compared to other ferritic-martensitic alloys, the ion-induced swelling of this alloy is quite low, arising from swelling resistance associated with both tempered martensite and dispersoids in both phases, with the swelling in tempered martensite being an order of magnitude less than in the ferrite phase.

F4-1. Introduction

Ferritic-martensitic (F/M) alloys are known to have greater resistance to void swelling, higher thermal conductivities and lower thermal expansion coefficients than do austenitic alloys [1-5]. The strength and swelling resistance of F/M alloys can be further improved by adding fine dispersions of various yttria oxides [6-10]. The majority of such oxide-dispersion-strengthened (ODS) alloys introduce dispersoids in ferrite phases [11-18]. However, previous studies have shown that in the absence of dispersoids, the ferrite phase is significantly less swelling resistant than the tempered martensite phase, as tested using neutron irradiation and heavy-ion irradiation [5,19]. The tempered martensite phase is usually smaller in grain size compared with ferrite, and has more dense and complex internal microstructure to serve as sinks for point defects created by radiation, thereby imparting additional resistance to void nucleation. Therefore, it has been suggested that employing dispersoids in the tempered martensite phase may gain additional swelling-suppression, first by pinning the grain walls to maintain small grain size and second by allowing the dispersoids to serve as sinks. To date, however, very limited results have been reported on ODS tempered martensite phase [7-9, 20, 21]. Among them, a 9Cr ODS tempered martensite alloy was reported to have promising swelling resistance, improved strength, but exhibited complicated dispersoid dissolution behavior under irradiation using a rastered ion beam [7-9, 20], in spite of the fact that beam rastering is known to suppress void nucleation and growth [22-24].

Recently, a novel 12Cr ODS dual-phase F/M alloy involving dispersoids in both ferrite and tempered martensite phase was developed to obtain superior corrosion and high-temperature oxidation resistance [25, 26]. This dual-phase alloy has a majority of tempered martensite phase and a minority of ferrite, at a ratio of ~4:1. The amount of ferrite phase, consisting of thermally equilibrium ferrite and residual ferrite, was optimized at ~ 20% to enhance its creep rupture strength [6, 26, 27]. In this work, microstructures of this 12Cr dual-phase ODS were characterized before and after ion irradiation to very high displacements per atom (dpa) values

using a defocused non-rastered beam. Defocusing beams were used since they better resemble reactor neutron damage, compared to pulsed beams that suppress void swelling [23, 24]. The radiation response of dispersoids in both ferrite and tempered martensite were studied separately, providing information to guide the next steps of material development toward a stronger radiation tolerance of F/M alloys.

F4-2. Experiment procedures

The composition of the 12Cr ODS dual-phase F/M alloy is provided in table 1. Elemental powders were mechanically alloyed in an argon gas atmosphere and consolidated at 1100 ºC for 2 hours. The consolidated specimens were then hot-extruded at 1150 ºC, normalized at 1050 ºC for 1 hour before tempering at 800 ºC for 1 hour. More extensive details of alloy synthesis have been reported by Ukai et. al [26].

Specimens were cut to dimensions of 5 mm × 5 mm × 0.7 mm and then mechanically polished with SiC paper, progressing down to a grit of 1200, followed by 0.05 μm aluminum powder. The surface layer containing residual mechanical damage was then removed using electrical polishing with a perchloric solution. Irradiation with 3.5 MeV Fe^{2+} ions was performed using a 1.7 MeV Tandetron accelerator. A defocused beam was used to avoid void-swelling-suppression characteristic of rastered beams [22-24]. The beam current was controlled at 200 ± 10 nA, producing a maximum dpa rate of ~ 1.74×10^{-3} dpa per second at damage peak. The depth profiles of dpa and injected Fe atoms, calculated by the SRIM code [28], are shown in Fig. 1. A value of 40 eV displacement threshold energy and the Kinchin-Pease option were used for the damage calculations [29, 30]. The irradiation temperature was controlled to be 475 ± 10 ºC to maximize swelling based on previous determinations of peak swelling temperatures [25, 31-33]. The chamber vacuum during irradiation was better than 1×10^{-6} torr.

Six specimens received 100, 200, 300, 400, 700 and 800 dpa at the peak displacement depth. Cross-sectional lamella samples from unirradiated and irradiated specimens were prepared using the focused-ion-beam (FIB) lift-out technique for transmission electron microscopy (TEM). TEM characterizations were performed using a 200 keV Technai F20 Supertwin microscope.

F4-3. Results

a) Characterization of unirradiated sample

Figure 2 shows typical TEM micrographs of a ferrite grain (Figs. 2a-b) and a tempered martensite grain (Figs. 2c-d) observed in the as-received unirradiated sample. The ferrite grain fraction was measured to be ~ 20%. As pointed out by Ukai et. al, the ferrite phase in this alloy consists of both residual ferrite and thermal equilibrium ferrite. While they arise from different mechanisms, these phases have essentially the same physical properties [26]. In addition, transformed ferrite can also exist when the phase transformation from austenite to ferrite takes place during air cooling [6]. Differences in grain size between ferrite and tempered martensite grains were obvious; ferrite grains were significantly larger (up to ~ 1μm) compared to tempered martensite grains (~200 nm).

Table 1: Composition of the as-received 12Cr dual-phase ODS alloy

Component:	Fe	C	Cr	Ni	W	Ti	N	Ar	Y_2O_3	Excess O
Weight:	85.74	0.16	11.52	0.34	1.44	0.28	0.007	0.006	0.36	0.144

Table 2: Mean grain size measured in as-received, irradiated and thermal-aged irradiation-free conditions

As-received sample	274 ± 65			Unit: nm
Location in sample	100 peak dpa	200 peak dpa	400 peak dpa	800 peak dpa
Peak dpa region	281 ± 61	271 ± 51	309 ± 40	268 ± 44
Irradiation free region	272 ± 46	293 ± 62	282 ± 46	241 ± 53

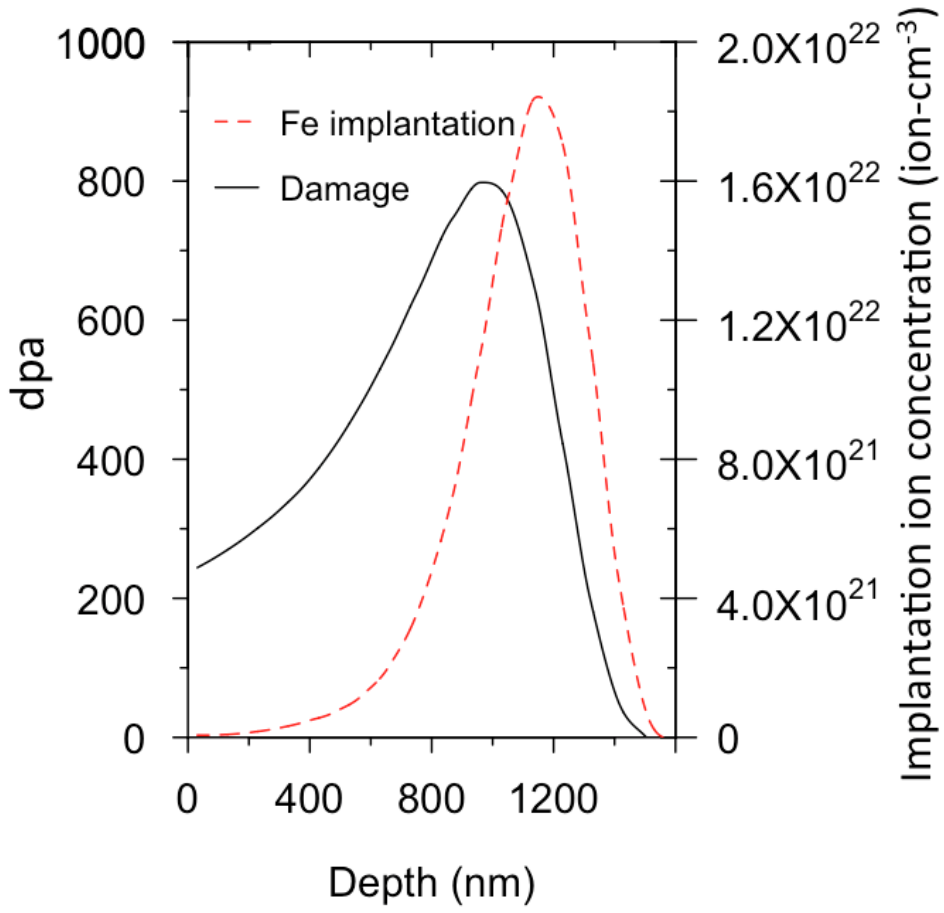

Figure 1: SRIM calculation of 3.5 MeV self-ion irradiation into pure Fe to 800 dpa maximum, using a displacement threshold energy of 40 eV and the Kinchin-Pease option.

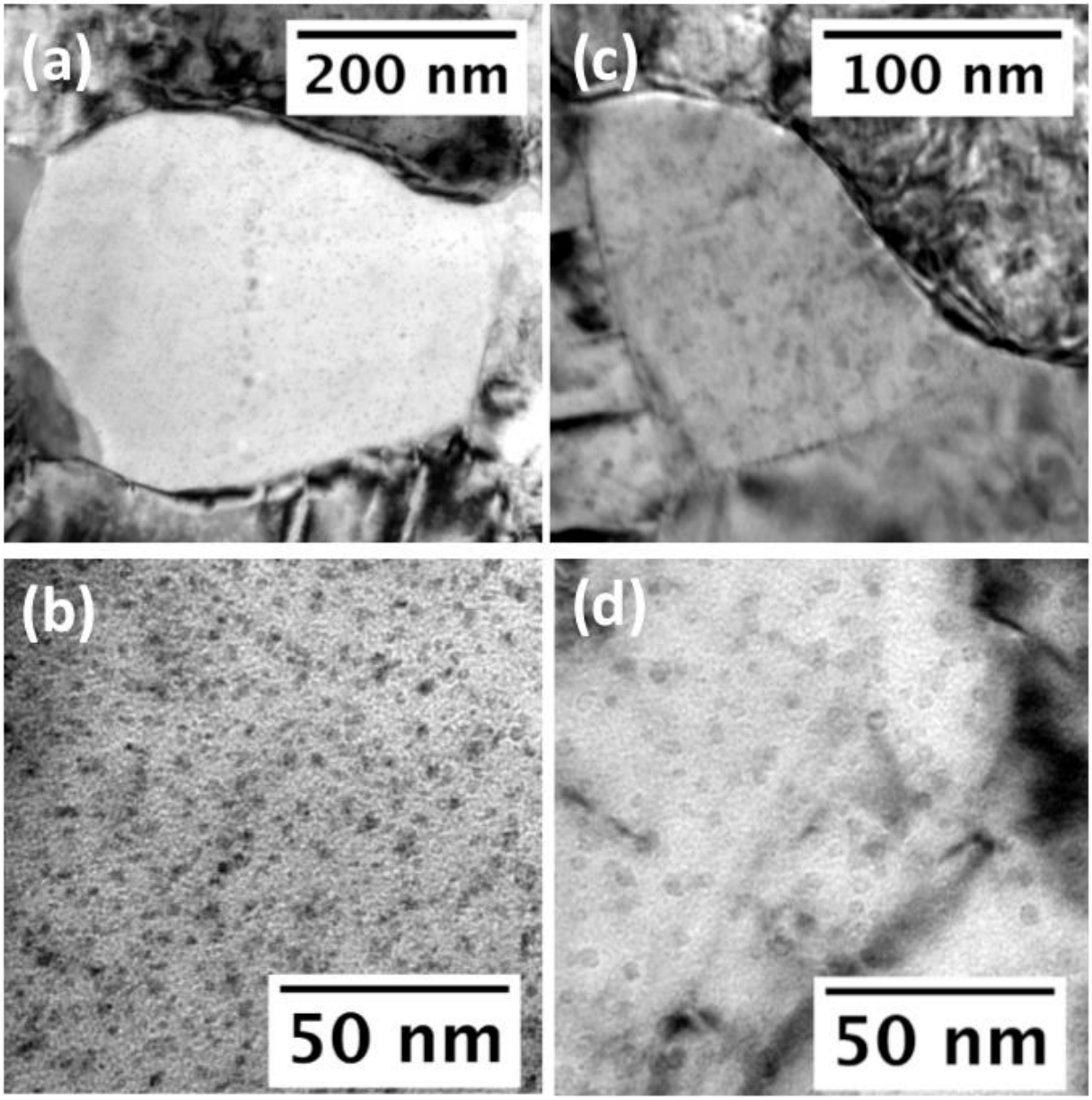

Figure 2: TEM micrographs of unirradiated samples having dispersoids in (a-b) a typical ferrite grain and (c-d) a typical tempered martensite grain.

Tempered martensite and ferrite grains were found to have different dispersoid distributions. As shown in Fig 2b, dispersoids in one ferrite grain are more uniform in size and more homogeneously distributed. In contrast, dispersoids in tempered martensite phase as shown in Fig 2d have large size variation even within one grain. The difference is statistically compared in Fig. 3, which was generated by measuring at least 100 randomly picked dispersoids from multiple grains in each of the ferrite and tempered martensite phases. The tempered martensite phase exhibits coarser dispersoids compared to the ferrite phase. In ferrite, while most dispersoids have diameter less than 5 nm, larger dispersoids were found in the transformed ferrite. Similar coarse distributions of dispersoids in tempered martensite and transformed ferrite phases were also observed in 9Cr and other 12Cr ODS [8, 26, 34]. It has been suggested that the disturbance of interfacial coherency between dispersoid and matrix, during phase transformation, results in the coarsening of dispersoids via interfacial energy minimization [6, 27, 35]. Therefore fine dispersoids were more likely to exhibit coherency with the matrix than larger dispersoids. In both phases, the dispersoid density varies significantly from grain to grain. The average dispersoid density in tempered martensite and ferrite phases were measured to be ~6×10^{16} cm^{-3} and ~1.6×10^{17} cm^{-3}, respectively. Energy-dispersive X-ray spectroscopy (EDS) analysis of dispersoids of sizes ranging from ~3 nm to ~30 nm in diameter showed an yttrium-titanium ratio (Y/Ti) of between ~1:1 and ~2:1.

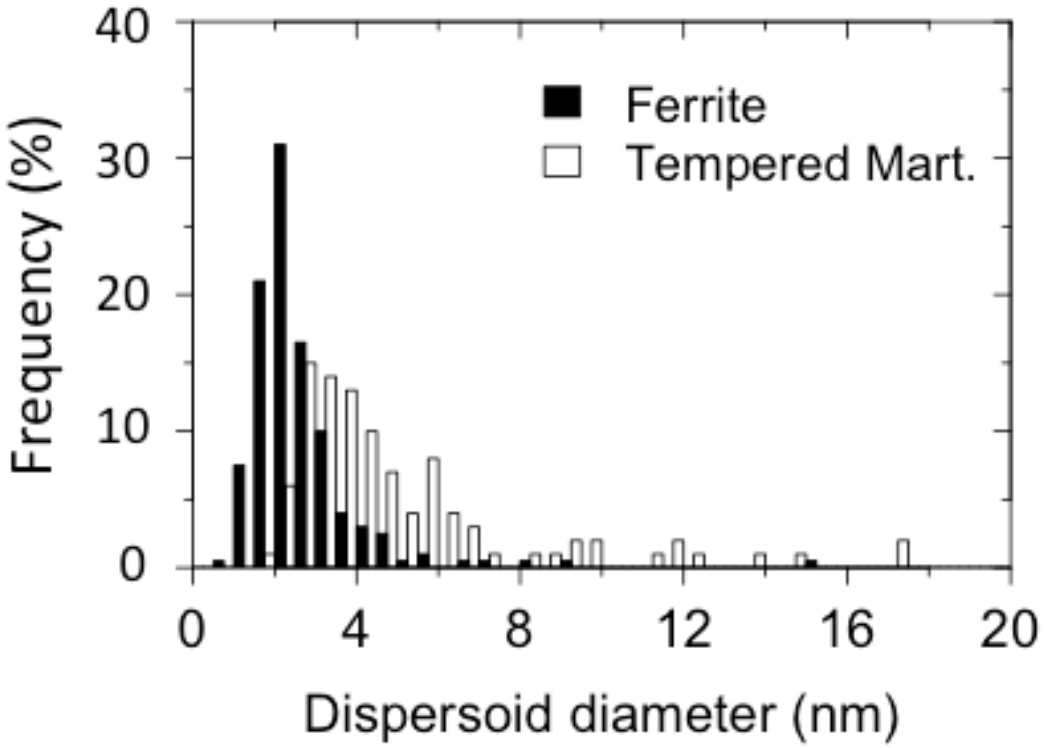

Figure 3: Size distribution of dispersoids in ferrite and tempered martensite grains in the before irradiation.

Figure. 4 shows bright field and weak beam dark field TEM micrographs of a tempered martensite grain. Dislocations and dispersoids have a non-uniform distribution and wide range in size. The dark field micrograph suggests that a coherent or semi-coherent relationship exists between most of the fine dispersoids and the matrix, as illustrated by the dashed arrow, while coarse dispersoids do not exhibit coherency, as illustrated by the solid arrow. This conclusion was later confirmed using high resolution TEM (HRTEM).

Figure 5 shows diffraction patterns and HRTEM micrographs of a ~3 nm dispersoid in a ferrite grain imaged at the $[012]_\alpha$ zone axis. The diffraction pattern in Fig. 5a shows coherency between dispersoids and the matrix, which are confirmed by HRTEM images in Figs. 5b-d. As marked by dashed lines in Fig. 5b, the nano-particle exhibited two planar directions clearly visible. The two plane-to-plane distances were measured to be 0.24 nm, and the angle between them was measured be to 61º. These agree with the 0.23 nm interplanar distance and 61.73º inter-direction angle of (331) and $(31\bar{3})$ planes of $Y_2Ti_2O_7$, suggesting a coherency of $(32\bar{1})_d \parallel (001)_\alpha$ and $[5\bar{6}3]_d \parallel [012]_\alpha$ between fine dispersoids and the ferrite matrix.

Figure. 6 shows diffraction patterns and HRTEM taken at $[011]_\alpha$ zone axes of a tempered martensite grain. Weak diffraction spots shown in Fig. 6a indicate that lattice coherency between fine dispersoids and the matrix exists, similar to fine dispersoids in ferrite phase. Figures. 6b-d correspond to a dispersoid with a diameter of ~6 nm. As shown in Figs. 6b-c, the coherency between the dispersoid and matrix is different from that of finer dispersoids. Two interplanar spacings were measured to be 0.28 nm and 0.27 nm with an angle of 86° between them, matching the (330) and (221) planes of orthorhombic Y_2TiO_5. Therefore interface coherency of $(151)_d \parallel (011)_\alpha$ and $[114]_d \parallel [011]_\alpha$ is suggested. For dispersoids larger than 10 nm in diameter, no coherency was observed.

b) Dispersoid shrinkage and stability

Figures 7a-d were obtained from the 400 peak dpa sample, presented as a panoramic TEM micrograph showing dispersoids starting from the irradiated surface to a depth beyond the peak damage (the dpa peak is located at ~ 1000 nm). Only grains of the tempered martensite phase are shown in Fig. 7d. Both depth (bottom) and the corresponding local dpa values (top) are provided. The enlarged TEM images of three local regions correspond to the near-surface region, the half peak-dpa region and the end of damage region, respectively. In comparison with the bulk unirradiated region, overall, dispersoid sizes within the irradiated region are reduced. Similar observations have been reported in previous studies on Ni^{2+} ion irradiated 9Cr ODS and 14YWT, whereas rastered beams were used [8, 36]. In addition, as shown in Figs. 7b-c, the highly irradiated region (in Fig. 7b) shows higher dispersoid density compared to regions receiving lower dpa (in Fig. 7c). Compared to unirradiated samples, the dispersoid density in tempered martensite was observed to increase due to irradiation by a factor of ~1.5.

The mean dispersoid sizes in samples after 100, 200, 400 and 800 peak dpa irradiation are plotted as a function of depth from irradiated surface in Fig. 8. The solid lines denote the size range of dispersoid distribution in unirradiated tempered martensite grains, and the dash lines denote the range of dispersoid sizes in unirradiated ferrite grains. One important finding is that

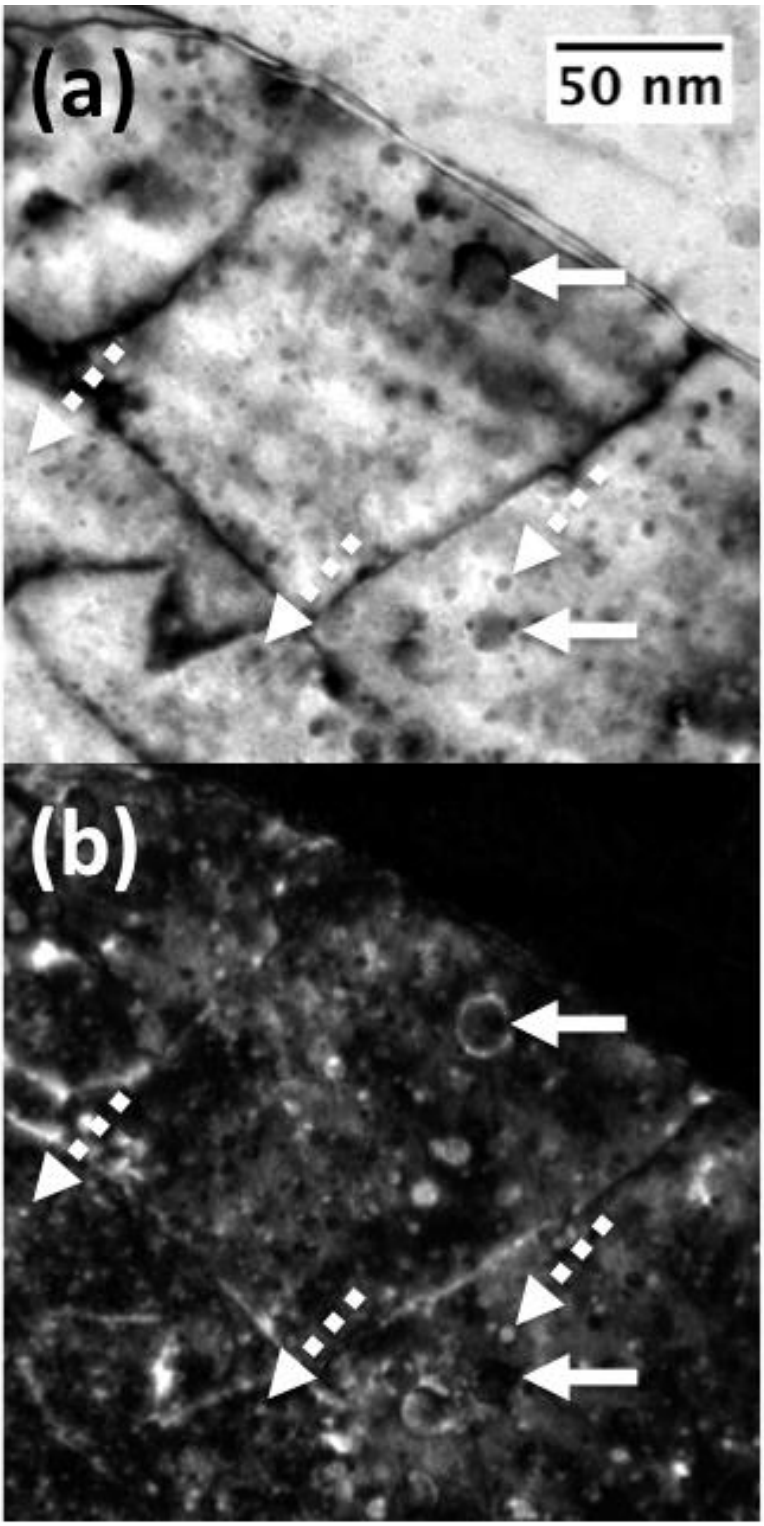

Figure 4: (a) Bright field TEM image and (b) weak beam dark field TEM image of an unirradiated tempered martensitic grain obtained near $\boldsymbol{g}_{110}$.

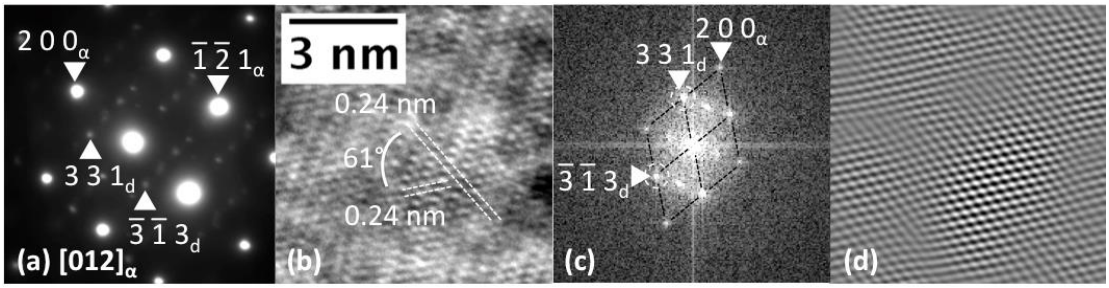

Figure 5: (a) Diffraction pattern of an unirradiated ferrite grain, (b) HRTEM micrograph of a dispersoid in this grain, (c) FFT diagram of the micrograph in (b), (d) FFT filtered image derived from diffraction spots circled in (c).

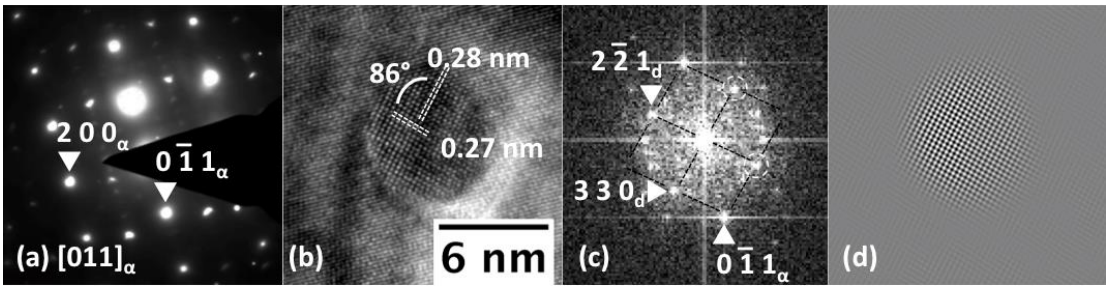

Figure 6: (a) Diffraction pattern of an unirradiated tempered martensite grain, (b) HRTEM micrograph of an dispersoid in this grain, (c) FFT diagram of the micrograph in (b), (d) FFT filtered image derived from diffraction spots circled in (c).

dispersoid sizes were reduced after irradiation and approached to ~2-2.5 nm in irradiated region (≤1000 nm), regardless of different dpa rates at different depths.

Figure 9a shows two neighboring ferrite and tempered martensite grains at ~750 dpa region in the 800 peak dpa irradiated sample. Figures 9b-c are higher-magnification TEM micrographs showing dispersoids in the ferrite and tempered martensite grains, respectively. Figure. 9d summarize size distributions of dispersoid in two phases after irradiation. Dispersoids in tempered martensite grains underwent a dramatic shrinkage. In both phases, most, if not all, dispersoids larger than 5 nm were removed by irradiation. In the ferrite phase, while there was a barely noticeable size change in the fine dispersoids, the dispersoid density dropped ~20%. Decrease in density and sustainment in size of the fine dispersoids in ferrite phase agrees with observations in neutron irradiated MA957 [13, 37], while loss of larger dispersoids in the tempered martensite phase agrees with previous studies by Allen, et al. on Ni irradiated 9Cr ODS [8]. It is important that in the present study, dispersoids of different sizes were confirmed to have different stability in the same dual-phase alloy.

Beyond 1200 nm, where the dpa level rapidly drops to zero, a plateau of dispersoid diameter appears at ~4-5 nm, a range close to the mean dispersoid diameter in the pre-irradiation condition. The dispersoid size distribution in the radiation-free zone is the same as it is in pre-irradiation condition, suggesting that observed size difference in the irradiated region results from irradiation effects, instead of thermal annealing effects.

To further illustrate the evolution of dispersoid populations with increasing damage level, an analysis of dispersoid size was carried out, limited to the 400 nm to 700 nm depth range, to minimize compositional changes resulting from the injected Fe atoms. The selected region corresponds to a damage level of ~ 60% of the peak dpa. Only tempered martensite data were used for this comparison. Figure. 10 shows that dispersoid shrinkage after ion irradiation essentially stops by 60 dpa; with a stable size distribution maintained thereafter. As pointed out in earlier studies, such stability of fine dispersoids can sustains ODS strength during irradiation [8, 10, 38].

c) Grain stability

Figures 11a-e show bright field cross-sectional TEM micrographs of the unirradiated sample and samples irradiated to 100, 200, 400 and 800 peak dpa, respectively. The dashed lines in Fig. 11 refer to the ~1 μm region that was irradiated. Deeper regions represent structures that were thermally annealed but not irradiated. Note that the sample receiving 800 peak dpa was annealed at 475 $\circ$ C for as long as ~125 hours. No changes of grain size were noticed for both ferrite and tempered martensite phases in either the irradiated or thermally aged regions. Statistics of grain size are listed in Table 2. Compared to unirradiated samples, all grain sizes were maintained within the statistical standard deviance.

d) Void swelling

As shown in Fig. 9a, the ferrite and tempered martensite phases exhibit different swelling behavior under irradiation. In the depth of 550-800 nm, faceted voids up to 45 nm in diameter formed in the larger central ferritic grain; while no voids were observed in the surrounding tempered martensite grains. Figures 12a-c show void formation in ferrite phase and Figs. 12d-f show void formation in tempered martensite phases as a function of dose. Micrographs were taken with an under-focus of ~500 nm to image very small voids. Faceted voids were observed in ferrite phase at doses as low as 50 dpa. The void size increases with increasing dpa values. In comparison, only nano-cavities were observed in tempered martensite phase. Since void numbers in ferrite phase are quite limited, we focused on statistic analysis of voids in martensite phase only. Figures. 12g-i plot the void size distributions at 50, 200, and 400 local dpa regions, respectively. With increasing dpa values, void sizes gradually increase but are still limited to only a few nanometers only. At 400 dpa, for instance, the mean size is ~1.4 nm.

Figures. 13a and b compare the depth-dependent swelling in ferrite and tempered martensite phases, respectively. The ”spikiness” of the swelling distribution results from low statistics when void numbers are limited. Overall, the swelling in ferrite is more than one order of magnitude higher than that in tempered martensite. Note, however, that while the peak dpa occurs at a depth of ~1000 nm from the surface, the swelling at higher dpa levels disappears at ~800 nm, which is

a well-known behavior attributed to combined effects from defect imbalance and the injected interstitial [39, 40]. This behavior has been frequently observed in self-ion irradiated pure iron and other F/M steels [24, 29, 40].

F4-4 Discussion

The 12Cr dual-phase ODS alloy appears to have a very good swelling resistance under the high-dpa ion irradiation conditions employed in this study. Figure 14 plots the largest swelling values observed in the ferrite phase, as a function of local dpa where the data were extracted. These data are compared with published data from MA957, an ODS ferrite alloy [11], but this is not a single variable comparison due to differences in irradiating ion, energy and dpa rate. Nevertheless, this figure shows the rather low swelling obtained in the alloy of this study. Even more importantly, the majority of tempered martensite phase in this alloy is swelling almost negligibly, producing a very low overall swelling.

The swelling rate of ferrite phase in this ODS at the highest dpa examined was estimated to be ~0.005 %/dpa, significantly lower than the steady-state swelling rate of ~0.2 %/dpa from neutron irradiation of Fe-Cr alloys reported by Garner et al. [3,33], and the ~0.12 %/dpa steady-state swelling rate shown in a recent study of α-Fe under self-ion irradiation [24]. This suggested that the incubation period before onset of steady-state swelling has not yet been reached in the 12Cr dual-phase alloy [11, 33]. The tempered martensite phase is known to have an even longer incubation period under ion irradiation, as observed in the two-phase alloy EM12 and EP-450 [5,19, 32].

In Fig. 15, we schematically show the understanding of the effects of dispersoids on void swelling and mechanical strength. The strong resistance to void swelling probably arises from a combination of factors. First, presence of fine grain structures with high boundary area is thought to provide defect trapping and annihilation sites [4, 11, 41, 42]. Higher densities of internal boundaries characteristic of tempered martensite may be critical to the swelling resistance. The fine grain structure and internal boundaries are also known to elevate hardness in F/M steels or F/M based ODS alloys [43]. The stability of grain sizes observed in this study suggests that both swelling resistance and hardness can persist to very high irradiation, possibly as a consequence of dispersoid locking and stabilizing of grain walls. Although there is larger swelling in the ferrite grains, a trade-off between swelling resistance and strength and ductility was made by optimizing composition, heat treatment and dispersoid volume and size [26]. In ferrite grains, dispersoids are finer with a higher density. As suggested by Ukai, such ultra fine dispersoids lead to enhanced hardness, creep rupture strength and tensile strength [6]. On the other hand, tempered martensite grains having larger dispersoid and larger dispersoid distance are likely to be less hard compared to ferrite. The ferrite grains surrounding tempered martensite grains are critical to maintaining the appropriate creep rupture strength.

Second, the finely distributed dispersoids of high density appear to have enhanced the swelling resistance, probably by playing two roles, stabilizing grain structures and trapping of defects. Previous studies showed that fine dispersoids suppress growth and recrystallization of grains [44] and phase transformations [26, 34]. The drag force applied to boundaries by dispersoids has been found to be stronger for finer size dispersoids [26, 34, 45]. In addition, as

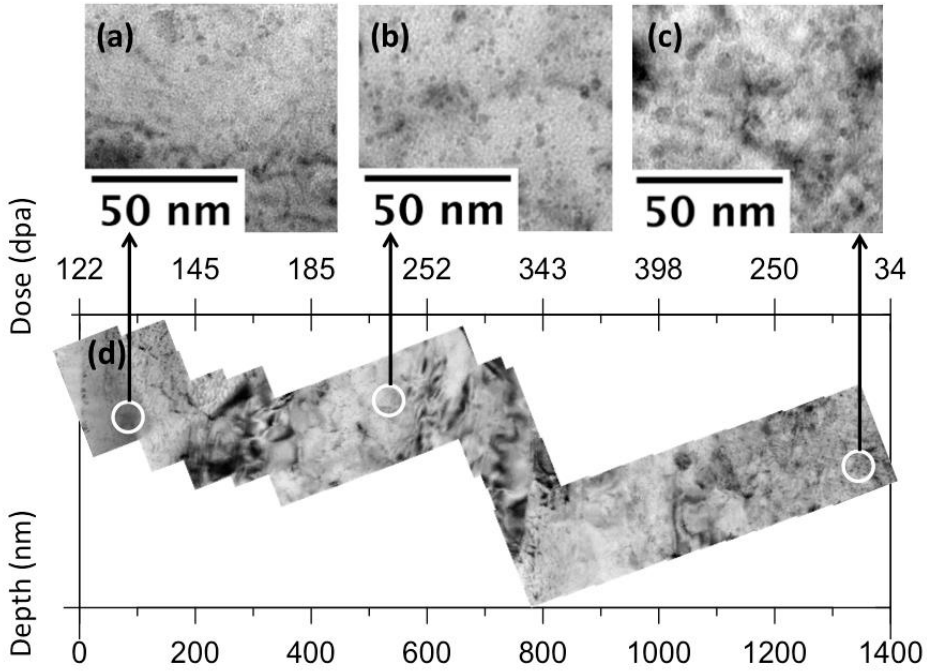

Figure 7: (a-c) TEM micrographics at near surface region, half-peak-dpa region and end of irradiation region, respectively, and (d) panoramic TEM micrographs from the 400 peak dpa sample.

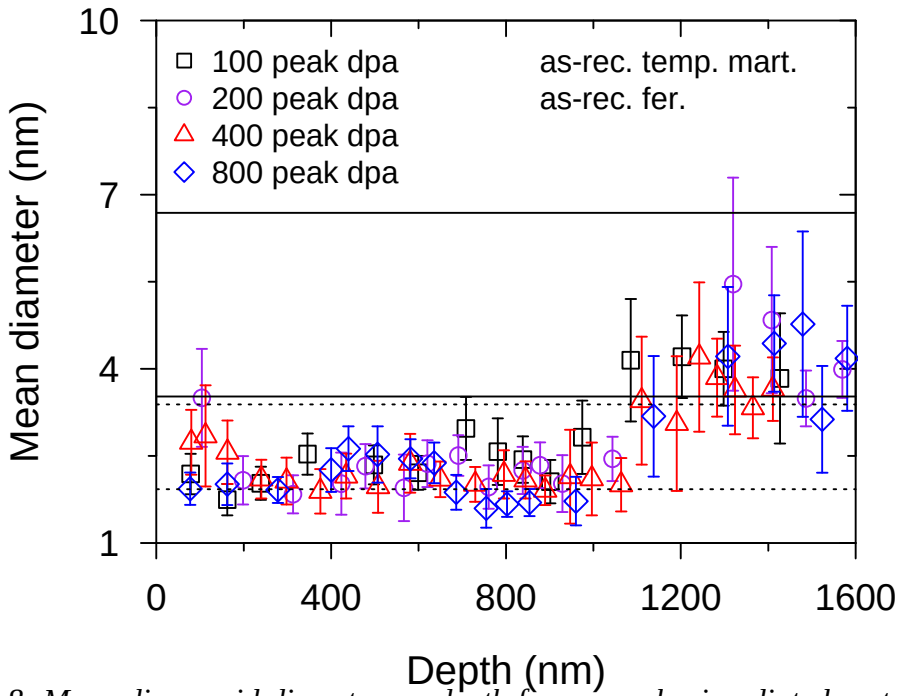

Figure 8: Mean dispersoid diameter vs. depth from samples irradiated up to peak dpa values of 100, 200, 400 and 800, with solid horizontal lines representing the range of the as-received dispersoid distribution in tempered martensite grains, and the dashed horizontal lines representing the range of the as-received dispersoid distribution in ferrite grains.

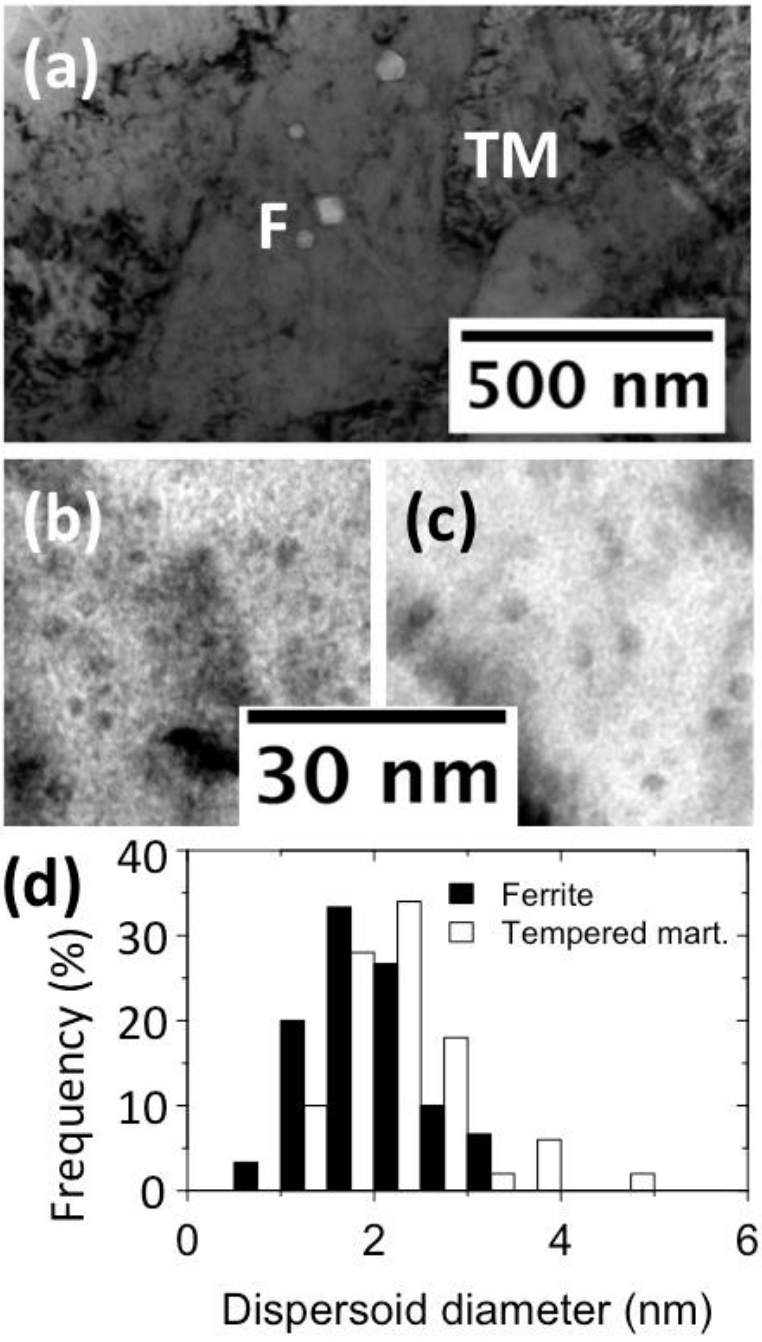

Figure 9: (a) TEM micrograph taken from the 500-1200 nm region of the 800 peak dpa sample, with F and TM referring to ferrite and tempered martensite phase, respectively, and (b), dispersoids in the ferrite grain F, and (c), dispersoids in the tempered martensite grain TM, and (d), statistic size distributions of dispersoids in irradiated ferrite and tempered martensite phases.

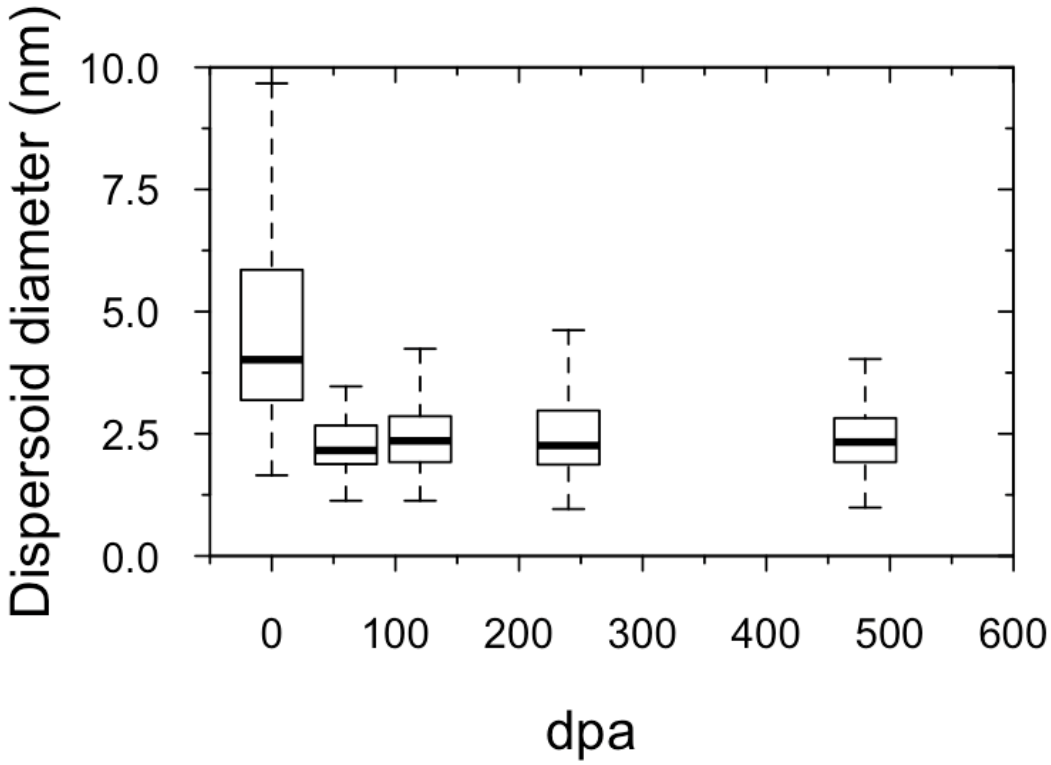

Figure 10: Dispersoid size as a function of increasing dpa in tempered martensite grains, with the bottom and top of the rectangular boxes represents the first and third quartiles of the statistic data, respectively, while the bar in the middle of the box represents the mean value.

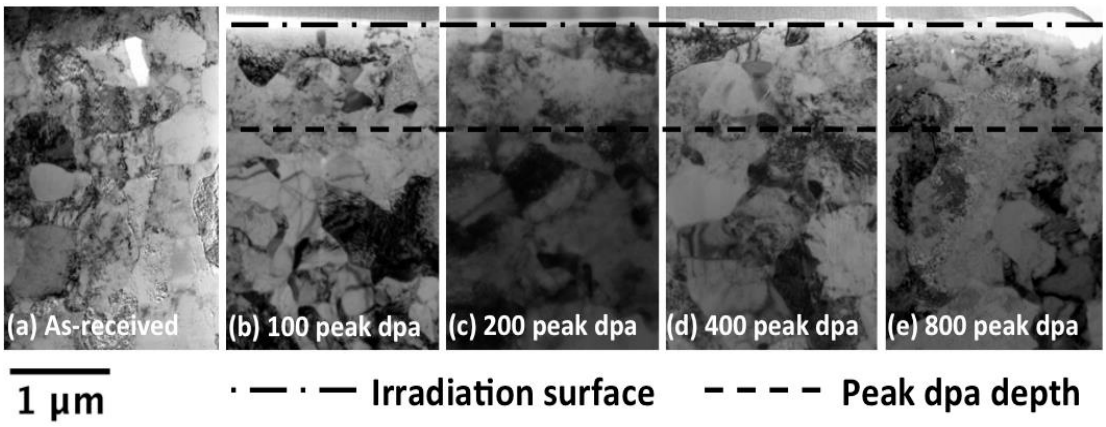

Figure 11: Bright field cross-sectional TEM micrographs of (a) unirradiated sample and (b-e) samples irradiated to 100, 200, 400 and 800 peak dpa, respectively. The dashed lines refer to the irradiated region.

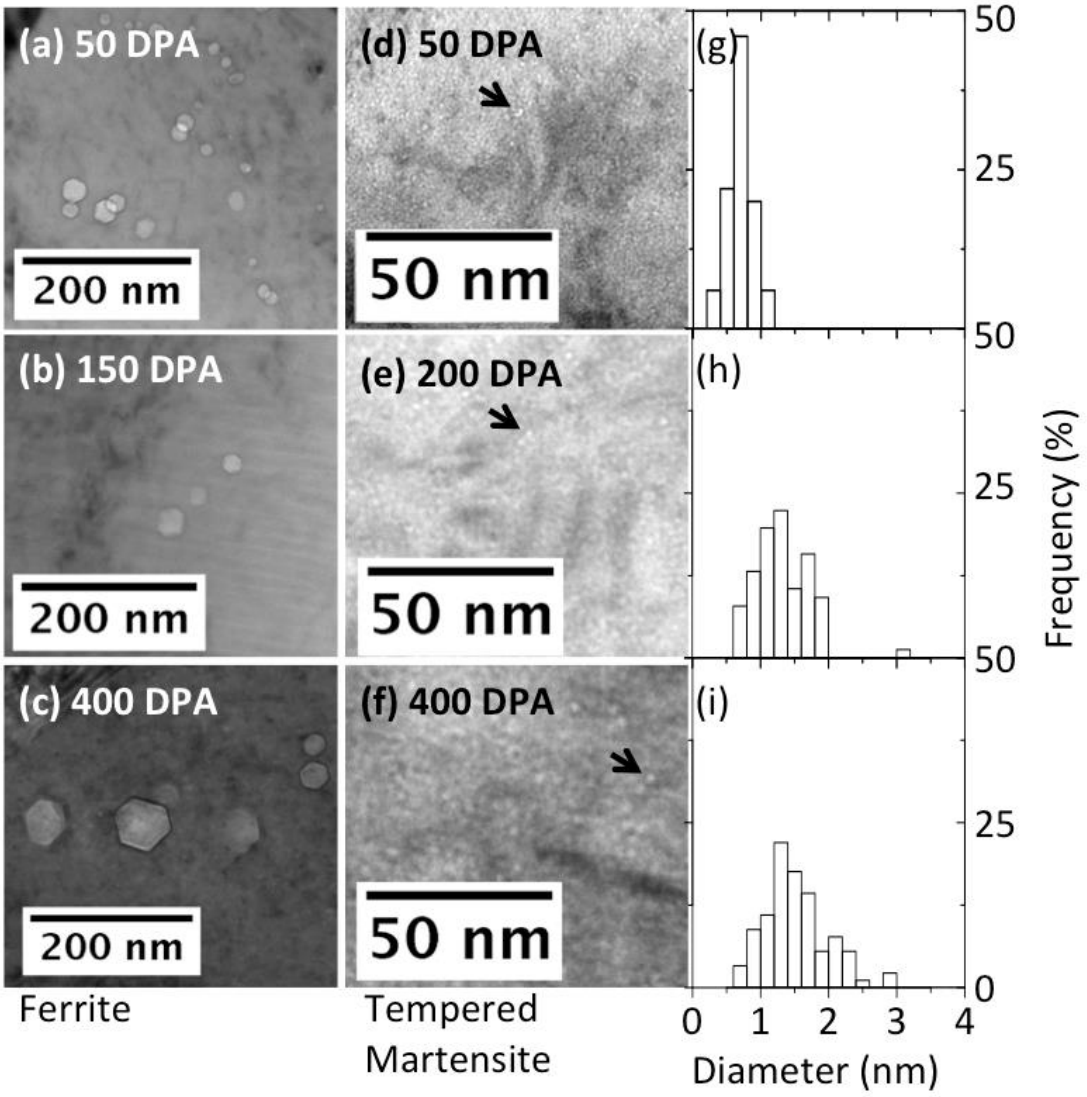

Figure 12: (a)-(c) TEM micrographs obtained at the depth of 500 nm in ferrite phases after 100, 300, 800 peak dpa irradiation, respectively, and (d-f) TEM micrographs obtained at the depth of 500 nm in tempered martensite phase after 100, 300, 800 peak dpa irradiation, respectively, with arrows highlighting some of the nano-cavities, and (g, h, i) the size distributions of nano-cavity in tempered martensite phases after irradiation corresponding to (d, e, f).

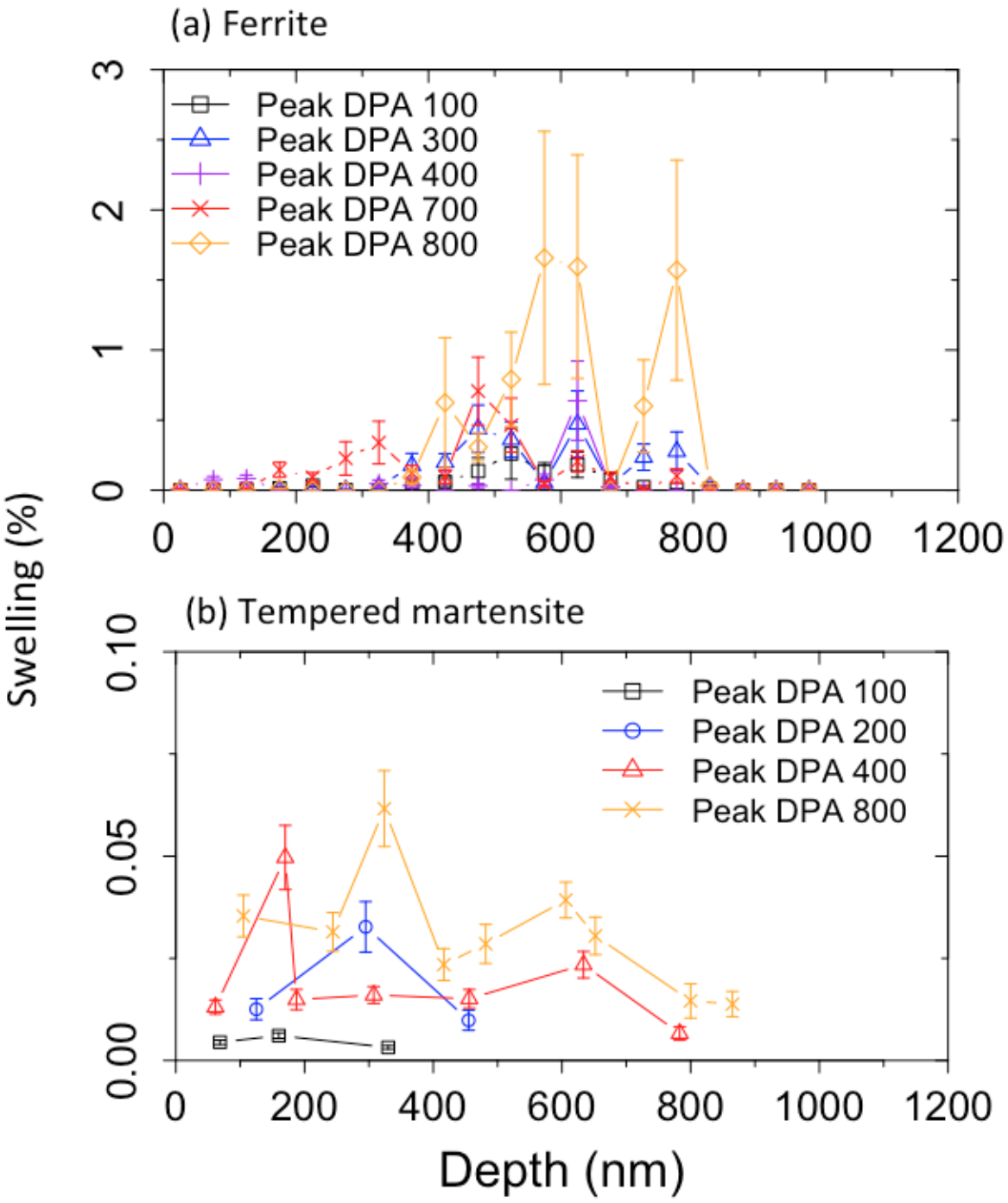

Figure 13: Swelling vs. depth distributions in (a) ferrite and (b) tempered martensite at different peak dpa levels.

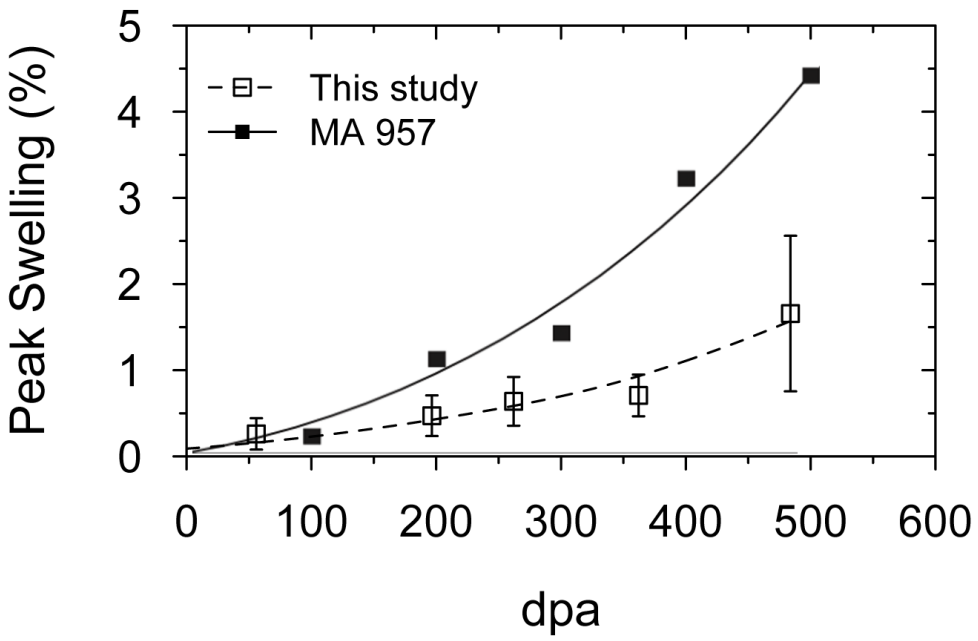

Figure 14: Maximum swelling as a function of local dpa in ferrite phase, in a comparison with swelling of s of ferritic MA957 [10]

.

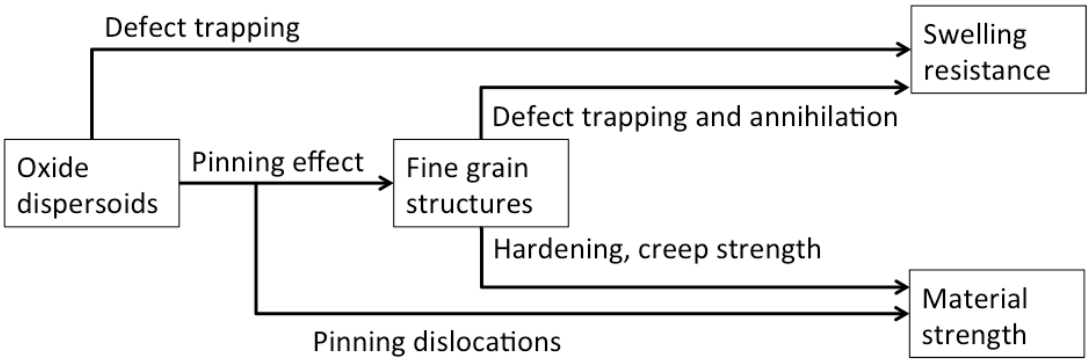

Figure 15: Schematic showing mechanisms of dispersoid effects on void swelling and mechanical properties.

reported by Allen, et al. high-density dislocation segments were observed in a 9Cr ODS alloy both before and after irradiation [9, 46]. Dispersoids were suggested to immobilize dislocations both within the grain and on the boundary walls, thereby preventing dislocation recovery under high-temperature irradiation [9, 46]. On the other hand, the interface between dispersoids and the matrix has been reported to serve as defect recombination sites [9, 11, 47]. In a spherical 200 nm tempered martensite grain with dispersoid distribution reported earlier, the ratio of dispersoid-matrix interface to grain boundary area would be approximately 7% before irradiation, which is reduced to half after irradiation, due to the loss of dispersoid. Without evaluating the defect trap strength of dispersoid-matrix interface, the dominating surface area of grain boundary in tempered martensite suggests its more important role in swelling resistance.

During irradiation, the loss of the less-frequent, larger dispersoids in the alloy of this study is insufficient to overcome the much higher density of small dispersoids, especially since the lost yttria volume appears to be partially compensated by the increased density of smaller dispersoids in tempered martensite.

The shrinkage in dispersoid size suggests the operation of a ballistic dissolution mechanism but the quickly reached equilibrium size suggests the presence of rather strong healing by re-precipitation processes. Notably, the equilibrium dispersoid size was not strongly correlated to the local dpa rate, indicating the strong influence of these healing mechanisms. This may be due in part to the strong insolubility of yttrium in the presence of excess oxygen.

Diffusion mechanisms are believed to influence the changes in dispersoid size under irradiation. Based on Russell's radiation-affected precipitation model of equilibrium phases [8, 48], it is expected that large dispersoids would shrink and small dispersoids would grow under irradiation, although large precipitates in this scenario would fall to the equilibrium size and not disappear altogether, as was observed in this study. Russell's model predicts that the equilibrium size would be dependent on dpa rate, a phenomenon which was not observed in the present study. In addition, no coherency was observed for dispersoids larger than ~10 nm in diameter and these larger dispersoids disappeared after irradiation, suggesting a correlation between dispersoid-matrix coherency and dispersoid stability. As another evidence of this correlation, dispersoids in both phases were observed to maintain coherency relationships with the matrix after irradiation, as observed in this study and others [37, 49]. Further studies are needed on the radiation response of dispersoids at different temperatures and under different dpa rates, in order to understand the mechanisms in determining the irradiation-stable size and structures of dispersoids. Focuses should be put on interface structural configuration and interface energy differences of dispersoids having different sizes, as well as atomic scale details of how interfaces interact with point defects.

In summary, high dpa Fe^{2+} ion irradiations up to 800 peak dpa were conducted on a dual-phase 12Cr ODS at 475 ºC. The alloy is very stable under irradiation with grain structures that were not significantly affected by radiation. During irradiation, dispersoids were found to reach to an equilibrium size and to change in density, while larger incoherent particles were destroyed. The equilibrium size, which was independent of dpa rate, was reached at as low as 60 dpa and was preserved to the highest irradiation level in this study. Dispersoids in ferrite grains were initially very close to the equilibrium size and therefore showed better irradiation stability than dispersoids in tempered martensite grains. There appears to be a correlation between coherency

and dispersoid stability. Void swelling was found to be much higher in ferrite grains than in tempered martensite grains, but overall the alloy was rather resistant to void swelling.

References

[1] F.A. Garner, in: Chapter 6 ”Irradiation performance of cladding and structural steels in liquid metal reactors”, volume 10A, Materials Science and Technology: A Comprehensive Treatment, VCH Publishers, 1994, pp. 419–543.

[2] R.L. Klueh, A.T. Nelson, Journal of Nuclear Materials 371 (2007) 37–52.

[3] B.H. Sencer, F.A. Garner, Journal of Nuclear Materials 283-287 (2000) 164–168.

[4] A.M. Dvoriashin, S.I. Porollo, Yu. V. Konobeev, F.A. Garner, Journal of Nuclear Materials 329-333 (2004) 319–323.

[5] F.A. Garner, L. Shao, M.B. Toloczko, S.A. Maloy, V.N. Voyevodin, in: 17th International conference on environmental degradation of materials in nuclear power systems - water reactors, Ottawa, Ontario, Canada, Aug. 9-13, 2015.

[6] S. Ukai, S. Ohtsuka, Energy Materials 2 (2007).

[7] S. Ohtsuka, S. Ukai, M. Fujiwara, T. Kaito, T. Narita, Materials Transactions 46 (2005) 487–492.

[8] T.R. Allen, J. Gan, J.I. Cole, M.K. Miller, J.T. Busby, S. Shutthanandan, S. Thevuthasan, Journal of Nuclear Materials 375 (2008) 26–37.

[9] J. Gan, T.R. Allen, B.C. Birtcher, S. Shutthanandan, S. Thevuthasan, JOM 60 (2008) 24–28.

[10] K. Mo, Z. Zhou, Y. Miao, D. Yun, H.-M. Tung, G. Zhang, W. Chen, J. Almer, J.F. Stubbins, Journal of Nuclear Materials 455 (2014) 376–381.

[11] M.B. Toloczko, F.A. Garner, V.N. Voyevodin, V.V. Bryk, O.V. Borodin, V.V. Mel’nychenko, A.S. Kalchenko, Journal of Nuclear Materials 453 (2014) 323–333.

[12] D.A. McClintock, D.T. Hoelzer, M.A. Sokolov, R.K. Nanstad, Journal of Nuclear Materials 386-388 (2009) 307–311.

[13] S. Yamashita, N. Akasaka, S. Ukai, S. Ohnuki, Journal of Nuclear Materials 367-370 (2007) 202–207.

[14] M.K. Miller, K.F. Russell, D.T. Hoelzer, Journal of Nuclear Materials 351 (2006) 261–268.

[15] S. Yamashita, S. Ohtsuka, N. Akasaka, S. Ukai, S. Ohnuki, Philosophical Magazine Letters 84 (2004) 525–529.

[16] L.L. Hsiung, M.J. Fluss, A. Kimura, Materials letters 64 (2010) 1782–1785.

[17] L.L. Hsiung, M.J. Fluss, S. Tumey, J. Kuntz, B. El-Dasher, M. Wall, B. Choi, A. Kimura, F. Willaime, Y. Serruys, Journal of Nuclear Materials 409 (2011) 72–79.

[18] S.K. Karak, J.D. Majumdar, Z. Witczak, W. Lojkowski, L. Ciupinski, K.J. Kurzydlowski, I. Manna, Metallurgical and Materials Transactions A 44A (2013) 2884–2894.

[19] P. Dubuisson, D. Gilbon, J.L. S_ran, Journal of Nuclear Materials 205 (1993) 178–189.

[20] A.G. Certain, K.G. Field, T.R. Allen, M.K. Miller, J. Bentley, J.T. Busby, Journal of Nuclear Materials 407 (2010) 2–9.

[21] R. Schäublin, A. Ramar, N. Baluc, V. de Castro, M.A. Monge, T. Leguey, N. Schmid, C. Bonjour, Journal of Nuclear Materials 351 (2006) 247–260.

[22] G.S. Was, Fundamentals of radiation materials science: metals and alloys, Springer, 2007.

[23] ASTM E521-83, Standard practice for neutron radiation damage simulation by charged-particle irradiation, volume 12.02, ASTM International, 2009.
[24] J. Gigax, E. Aydogan, T. Chen, D. Chen, Y. Wu, W.Y. Lo, Y. Yang, F.A. Garner, Journal of Nuclear Materials 465 (2015) 343-348.
[25] R.L. Klueh, D.R. Harries, High-chromium ferritic and martensitic steels for nuclear applications, ASTM International, West Conshohocken, PA, 2001.
[26] S. Ukai, Y. Kudo, X. Wu, N. Oono, S. Hayashi, S. Ohtsuka, T. Kaito, Journal of Nuclear Materials 455 (2014) 700–703.
[27] S. Ukai, Metal, ceramic and polymeric composites for various uses, ISBN 978-953-307-353-8, InTech, 2011.
[28] J.F. Ziegler, J.P. Biersack, 2013, SRIM program. URL: http://www.srim.org/.
[29] L.R. Greenwood, R.K. Smither, SPECTER: neutron damage calculations for materials irradiations, Technical Report ANL/FPP/TM-197, Argonne National Laboratory, Lemont, IL, 1985.
[30] R.E. Stoller, M.B. Toloczko, G.S. Was, A.G. Certain, S. Dwaraknath, F.A. Garner, Nuclear Instruments and Methods in Physics Research B 310 (2013) 75–80.
[31] F.A. Smidt Jr., P.R. Malmberg, J.A. Sprague, J.E. Westmoreland, Swelling behavior of commercial ferritic alloys, EM-12 and HT-9, as assessed by heavy ion bombardment, volume STP 611, ASTM International, Philadelphia, PA, 1976, pp. 227–241.
[32] V. Bryk, O. Borodin, A. Kalchenko, V. Voyevodin, V. Ageev, A. Nikitina, V. Novikov, V. Inozemtsev, A. Zeman, F.A. Garner, in: Proceedings of Accelerator Applications, Bruges, Belgium, p. 1.
[33] F.A. Garner, M.B. Toloczko, B.H. Sencer, Journal of Nuclear Materials 276 (2000) 123–142.
[34] M. Yamamoto, S. Ukai, S. Hayashi, T. Kaito, S. Ohtsuka, Journal of Nuclear Materials 417 (2011) 237–240.
[35] Y. Yazawa, T. Furuhara, T. Maki, Acta Materialia 52 (2004) 3727–3736.
[36] J. He, F. Wan, K. Sridharan, T.R. Allen, A. Certain, V. Shutthanandan, Y.Q. Wu, Journal of Nuclear Materials 455 (2014) 41–45.
[37] J. Ribis, S. Lozano-Perez, Journal of Nuclear Materials 444 (2014) 314–322.
[38] Y. Miao, K. Mo, Z. Zhou, X. Liu, K.-C. Lan, G. Zhang, M.K. Miller, K.A. Powers, J. Almer, J.F. Stubbins, Materials Science & Engineering A 625 (2015) 146–152.
[39] F.A. Garner, Journal of Nuclear Materials 117 (1983) 177–197.
[40] L. Shao, C.C. Wei, J. Gigax, A. Aitkaliyeva, D. Chen, B.H. Sencer, F.A. Garner, Journal of Nuclear Materials 453 (2014) 176–181.
[41] D. Chen, J. Wang, T. Chen, L. Shao, Scientific Reports 3 (2013).
[42] M. Song, Y. Wu, D. Chen, X. Wang, C. Sun, K.Y. Yu, Y. Chen, L. Shao, Y. Yang, K.T. Hartwig, X. Zhang, Acta Materialia 74 (2014) 285–295.
[43] M. Song, C. Sun, J. Jang, C.H. Han, T.K. Kim, K.T. Hartwig, X. Zhang, Journal of Alloys and Compounds 577 (2013) 247–256.
[44] A.O.F. Hayama, H.R.Z. Sandim, J.F.C. Lins, M.F. Hupalo, A.F. Padilha, Materials Science & Engineering A 371 (2004) 198–209.
[45] E. Nes, N. Ryum, O. Hunderi, Acta Materialia 33 (1985) 11–22.
[46] T.R. Allen, J. Gan, J.I. Cole, S. Ukai, S. Shutthanandan, S. Thevuthasan, Nuclear Science and Engineering 151 (2005) 305–312.

[47] Y. Chen, L. Jiao, C. Sun, M. Song, K.Y. Yu, Y. Liu, M. Kirk, M. Li, H. Wang, X. Zhang, Journal of Nuclear Materials 452 (2014) 321–327.
[48] K.C. Russell, Journal of Nuclear Materials 206 (1993) 129–138.
[49] M.-L. Lescoat, J. Ribis, Y. Chen, E.A. Marquis, E. Bordas, P. Trocellier, Y. Serruys, A. Gentils, O. Kaïtasov, Y. de Carlan, A. Legris, Acta Materialia 78 (2014) 328–340.

Research Highlight #5

Dispersoid stability in ion irradiated ODS alloy: temperature effect

We studied oxide dispersoid stabilities under different irradiation temperatures. Self-ion irradiations at various temperatures ranging from 325 ℃ to 625 ℃ have been carried out to a 12Cr F/M ODS alloy containing tempered-martensite structure. After irradiating up to damage levels of 200 peak dpa, we found that ODS grain structures were stable, while dispersoids shrank to equilibrium sizes. The dispersoid mean sizes increase with increasing radiation temperatures. Weak-beam dark field micrographs show that dislocations were pinned even after 625 ℃ irradiation. Most dispersoids were found to be coherent with the matrix. The evolution of dispersoid under irradiation can be understood by as a competition between radiation-driven removal and diffusion-driven recovery of dispersoid constituents, with the latter influenced by the dispersoid-matrix interface configurations. This study provides further insights into dispersoid behaviors under irradiation environment,

F5-1 Introduction

Ferritic-Martensitic (F/M) steel is a candidate for cladding materials in sodium-cooled fast reactors. F/M steel is chosen over the traditional-used austenite steel not only because of its lower thermal expansion and higher thermal conductivity, but also its overall higher radiation tolerance [1-7]. Swelling resistance of F/M steels is superior compared to austenite steels, with a steady-state swelling rate being one fifth of the latter. Swelling resistance can be further enhanced by increasing the amount of defect sinks, such as employing martensite structures, high density of grain boundary, dispersoids with additional defect-trapping interfaces [6-13]. The thermal creep resistance of F/M steel, however, is not as good as austenite steels, primarily due to the high dislocation mobility at elevated temperatures of F/M steels. Ukai et al. proposed an oxide-dispersion-strengthening (ODS) alloy design with mesoscopic optimization of ferrite/tempered martensite dual-phase and nano-scale optimization of ultra-fine oxide particles to enhance creep strength [14]. The 9Cr dual-phase ODS fabricated based on this design has already shown enhanced creep strength as well as good radiation tolerance [14-16]. Recently, a 12Cr dual-phase ODS has been designed and fabricated, exhibiting a promising mesoscopic microstructure for high temperature strength [13, 17]. Meanwhile, the superior swelling resistance, and microstructure stability of this material against high displacements per atom (dpa) radiation damage suggests it can maintain the strength under severe irradiation environment.

The stability of nano-sized dispersoids is very critical to the high temperature strength of an ODS alloy. The effect of nanoparticles is three folded. First, they serve as defect-trapping sites, which can reduce void swelling and save the material from undergoing significant volume changes; second, they stabilize the grain structure of the material; and third, they pin dislocations from moving and prevent thermal creep. Thus, it is of great importance to understand the evolution of nano-sized dispersoids under various irradiation conditions. Previous studies on ODS show that dispersoids can shrink and/or dissolve [13, 15, 18, 19], coarsen and/or grow [20-22], undergo amorphization [23-25] or undergo no changes [26-28] under neutron and ion irradiations of different conditions. More systematic studies should be carried out to provide solid data and understandings of the behavior of dispersoids under irradiations. This study showed some details of nanoparticle changes after irradiations at different temperatures, which shed some light on the topic of radiation response of nano- structures in ODS. On the other hand, the radiation tolerance of the unique 12Cr dual-phase ODS was tested to show the potential of

this material to maintain its strength in a high irradiation environment at different elevated temperatures.

F5-2 Experimental details

The 12Cr ODS dual-phase alloy investigated in this study was supplied by the Department of Material Science and Engineering, Hokkaido University, Japan. As reported by Ukai et. al [17], the sample was normalized at 1050 ℃ for 60 minutes and tempered at 800 ℃ for 60 minutes. The two phases, i.e., tempered martensite and ferrite, have a ratio of ~4:1 [13], which was controlled through nickel content [17]. Y-Ti-O dispersoids have been observed in both phases with distinct distributions [13]. The chemical composition of this alloy can be found in Table 1, where "Ex. O" stands for excess oxygen, a critical factor for nano-scale structure control [14].

Figure 1a shows the damage profile of 3.5 MeV Fe self-ion calculated using SRIM code [29]. The displacement threshold energy of Fe matrix was set to 40 eV, and the Kinchin-Pease option was used [30, 31]. The solid black line represents dpa rate, which has a peak value of 1.74×10-3 dpa per second at the depth of ~1000 nm. The dashed red line represents the injected Fe flux, whose maximum value is ~ 3.8 × 1016 ion/cm3⁄s, given that a 200 ± 10 nA Fe2+ defocused beam was used to conduct irradiations.

Irradiation was carried out using a 1.7 MeV Tandetron accelerator. The beam condition and pre-irradiation sample preparation can be found elsewhere [13, 32]. Three elevated temperatures, i.e., 325 ℃, 475 ℃ and 625 ℃ were chosen as the irradiation temperature. At each temperature, irradiations of 100 and 200 peak dpa were carried out. Microstructure of irradiated samples was investigated using a 200 keV Technai F20 Supertwin transmission electron microscope (TEM). The TEM specimens were prepared using a Tescan LYRA-3 focused-ion-beam (FIB) and secondary-electron-microscope (SEM).

F5-3 Results and discussions

a) Microstructure stability

Figure 2 shows the grain structures of samples before and after irradiations at various temperatures. In Fig. 2b-d, no obvious grain-size changes were observed due to irradiation at 325-625°C, when compared to Fig. 2b. In addition, no obvious changes were found in either ferrite or tempered martensite structures in irradiated regions, exhibiting the radiation stability of both phases. Being able to maintain the mesoscopic structures under irradiations at elevated temperatures is very important to retaining the enhanced creep strength of this material [14]. On the other hand, no void swelling was observed except for 475°C sample. At 475 ℃, more swelling occurs in ferrite grains than in tempered martensite grains, which has been reported earlier [13]. It is well known that void swelling peaks at an intermediate temperature below the melting point temperature, due to the reduction of defect mobility and the stability of vacancy loops at lower temperatures, and the vacancy flux being counterbalanced by the enhanced emission of vacancies from voids at higher temperatures [4, 33].

b) Dispersoid size changes due to irradiation

Figure 3 shows TEM micrographs obtained in tempered martensite grains of samples receiving 100 and 200 peak dpa at different temperatures. Each micrograph was taken at the depth of 500 nm from the

irradiating surface, so the local dpa of the regions of observation is approximately half of the peak dpa as labeled. Nano-sized dispersoids are shown as gray spots in the conventional bright field images as a result of Z- and diffraction contrast. Compared to the unirradiated sample shown in Fig. 3a, the size of dispersoids reduced due to ion bombardment. In addition, Fig. 3b-g shows that the dispersoid size is smaller at lower irradiation temperature.

Dispersoid size changes are clearly caused by ion irradiation damage. We compared the depth dependent size changes with SRIM calculation in Fig. 1b, for different temperatures and different radiation damage levels. At each temperature, dispersoid size data points of different damage levels appear to converge. On the other hand, higher irradiation temperatures result in larger dispersoids on average. The dispersoid size begins to increase beyond ~1000 nm, which is aligned with peak damage region simulated by SRIM, as shown in Fig. 1a. From the depth of ~1000 nm to the depth of ~1600 nm, as dpa values quickly reduce to zero, mean dispersoid sizes increase back to that of as-received condition.

Figure 4 plots the mean dispersoid size as a function of local dpa, where dispersoid size data were taken from the depth of 400-700 nm from the irradiation surface. The temperature-dependent radiation-induced change in dispersoid size is demonstrated. In addition, at each temperature, it appears that the mean dispersoid size is approaching an equilibrium value beyond a dpa of 60. This suggests that at a certain stage, back-diffusion and recovery of dispersoids can counterbalance the removal of dispersoid atoms due to irradiation; and a steady-state of dispersoid distribution would be achieved.

c) Dispersoid density and coherency

To enhance the diffraction contrast, a near two-beam condition was achieved, and bright field (BF) and weak beam dark field(WBDF) images were taken from randomly chosen tempered martensite grains within regions receiving radiation damage levels of ~60-70 dpa at various temperatures, as shown in Fig 5. With **g**110 excited, WBDF images show prominent features such as coherent dispersoids and dislocations with burger's vectors not perpendicular to **g**110. Semi-coherent dispersoids were observed after 625 °C irradiation, as shown in the inserted figures in Fig 5c with misfit Moiré fringes. Semi-coherent dispersoids were not observed in any of the lower temperature irradiated samples. Arrows in Fig 5 highlights dislocations pinned by dispersoids in the matrix, which suggests that the pinning effect of dispersoids provides enhancement to creep resistance by preventing dislocation migration at elevated temperatures up to 625°C.

Number densities of coherent dispersoid can be obtained using WBDF images as they highlight coherent particles. Coherent dispersoid density in tempered-martensite grains before irradiation was measured to be $6.6 \pm 1.2 \times 10^{16}\ cm^{-3}$. As shown in Table 2, the density appeared to slightly increase after 475°C irradiation and decrease after 625°C irradiation. Total dispersoid density, regardless of their coherency, was also estimated for samples before and after irradiation, by using BF micrographs. 325°C irradiated sample was not included in table 2, because of the formation of high-density defects that will be explained later. The fraction of coherent dispersoid number to total dispersoid number is reduced in 625°C irradiated sample compared to as-received and 475°C irradiated sample, as shown in table 2.

Figure 6 plots distributions of dispersoid in size before and after receiving irradiation at different temperatures, obtained from BF and WBDF micrographs of multiple randomly picked tempered-

martensite grains in irradiated regions, using at least 100 particles for each category. Agreeing with observations from conventional BF micrographs, dispersoids were found to shrink in size after irradiation, with the broadness of size distribution decrease with decreasing irradiation temperature. Comparing coherent and total distributions in Fig. 6a, it is evident that larger dispersoids tend to be incoherent while most of the smaller dispersoids are coherent. After irradiation at 475°C, the coarse and incoherent dispersoids seemed to disappear as shown in Fig. 6c; however, more larger and incoherent dispersoids were found after 625°C irradiation, as shown in Fig. 6b.

Figure 7a and 7b presents WBDF micrographs near **g**002 and **g**110 of one tempered martensite grain receiving ~65 dpa at 325°C, respectively. Compared to microstructures from higher-temperature irradiations shown in Fig. 5eg, features shown in Fig. 7ab are finer and denser, whose distribution is plotted in Fig. 7c. These features most likely include the so-called black spot damages, interstitial and dislocation loops (as shown in the inserted micrograph in Fig. 7b), yttria dispersoids, and other precipitates based on previous observations in F/M steels and ODS irradiated under similar conditions [18, 34-39]. Although it is impossible to distinguish yttria from other features due to its ultra-fine size after irradiated at 325°C, the size distribution of yttria is part of the distribution shown in Fig. 7c. Compared to results of higher temperature irradiations in Fig. 6bc, the dispersoid, if it remains in the matrix after 325°C self-ion irradiation, has a distribution peaks at a smaller size and narrower range.

d) Dispersoid distribution and creep resistance

The correlation of dispersoid coherency and dispersoid size has been reported in ODS alloys [13, 40-42]. In general small dispersoids tend to have various coherency relationships to matrix [13, 40] while large dispersoids tend to be semi-coherent [41] and eventually lose coherency as they become larger [13, 40, 41]. From a thermodynamic interpretation, this correlation is a result of the minimization of free energy [40]. The free energy of an ideal spherical dispersoid can be described as a sum of interfacial energy and elastic energy. The interfacial energy of a spherical particle with radius r is $4\pi r2 \cdot \gamma i$, where γi is the unit-area interface energy. For an incoherent dispersoid, the elastic energy is negligible compared to interfacial energy, given the elastic moduli of the matrix and the dispersoids are relatively close [43]. For a coherent dispersoid, however, the strain energy introduced due to the lattice misfit δ should be considered as $4\pi r3\diagup3 \cdot 4\delta2\mu$ [44]. Given that coherent interface has a smaller γi, a competition between interface energy and elastic energy leads to smaller dispersoids taking coherency while larger dispersoids not.

Figure 6a exhibits the trend of incoherency in larger dispersoids, which agrees to the discussions on thermodynamics above. On the other hand, the coherent dispersoid distribution of radiation-free samples in tempered martensite, shown as white bars in Figure 6a, is similar to the dispersoid distribution in radiation-free ferrite phase as earlier reported [13]. This suggests that during material fabrication and prior to γ-α transformation [17], dispersoids might have an identical distribution in both phases with most of them being small and coherent. Dispersoids which lost their coherency during γ-α transformation coarsened through Ostwald ripening [14, 45, 46], a kinetic process also believed to occur during high-temperature annealing or irradiation [22]. As a result, the distribution of total dispersoids in tempered martensite phase is broadened by including coarse incoherent dispersoids.

In a summary, compared to the irradiation free sample, dispersoids were found to shrink after irradiation, approaching to an equilibrium size that is related to irradiation temperatures. We found that dispersoid-matrix coherency plays an important role in determining dispersoid sizes at different irradiation temperatures. The complexity of dispersoid coherence is due to the higher interface energy of semi-coherent/incoherent dispersoids compared to coherent dispersoids.

References

[1] S.J. Zinkle, G.S. Was, Acta Materialia 61 (2013) 735–758.
[2] S.J. Zinkle, J.T. Busby, Materials Today 12 (2009).
[3] R.L. Klueh, A.T. Nelson, Journal of Nuclear Materials 371 (2007) 37–52.
[4] F.A. Garner, in: Chapter 6 "Irradiation performance of cladding and structural steels in liquid metal reactors", volume 10A, Materials Science and Technology: A Comprehensive Treatment, VCH Publishers, 1994, pp. 419–543.
[5] L.K. Mansur, A.F. Rowcliffe, R.K. Nanstad, S.J. Zinkle, W.R. Corwin, R.E. Stoller, Journal of Nuclear Materials 329-333 (2004) 166–172.
[6] F.A. Garner, M.B. Toloczko, B.H. Sencer, Journal of Nuclear Materials 276 (2000) 123–142.
[7] F.A. Garner, L. Shao, M.B. Toloczko, S.A. Maloy, V.N. Voyevodin, in: 17th International conference on environmental degradation of materials in nuclear power systems - water reactors.
[8] P. Dubuisson, D. Gilbon, J.L. Séran, Journal of Nuclear Materials 205 (1993) 178–189.
[9] B.H. Sencer, F.A. Garner, Journal of Nuclear Materials 283-287 (2000) 164–168.
[10] M. Song, Y. Wu, D. Chen, X. Wang, C. Sun, K.Y. Yu, Y. Chen, L. Shao, Y. Yang, K.T. Hartwig, X. Zhang, Acta Materialia 74 (2014) 285–295.
[11] D. Chen, J. Wang, T. Chen, L. Shao, Scientific Reports 3 (2013).
[12] M.B. Toloczko, F.A. Garner, V.N. Voyevodin, V.V. Bryk, O.V. Borodin, V.V. Mel'nychenko, A.S. Kalchenko, Journal of Nuclear Materials 453 (2014) 323–333.
[13] T. Chen, E. Aydogan, J.G. Gigax, D. Chen, J. Wang, X. Wang, S. Ukai, F.A. Garner, L. Shao, Journal of Nuclear Materials 467 (2015) 42–49.
[14] S. Ukai, S. Ohtsuka, Energy Materials 2 (2007) 26–35.
[15] T.R. Allen, J. Gan, J.I. Cole, M.K. Miller, J.T. Busby, S. Shutthanandan, S. Thevuthasan, Journal of Nuclear Materials 375 (2008) 26–37.
[16] J. Gan, T.R. Allen, B.C. Birtcher, S. Shutthanandan, S. Thevuthasan, JOM 60 (2008) 24–28.
[17] S. Ukai, Y. Kudo, X. Wu, N. Oono, S. Hayashi, S. Ohtsuka, T. Kaito, Journal of Nuclear Materials 455 (2014) 700–703.
[18] J. He, F. Wan, K. Sridharan, T.R. Allen, A. Certain, V. Shutthanandan, Y.Q. Wu, Journal of Nuclear Materials 455 (2014) 41–45.
[19] I. Monnet, P. Dubuisson, Y. Serruys, M.O. Ruault, O. Kaïtasov, B. Jouffrey, Journal of Nuclear Materials 335 (2004) 311–321.
[20] S. Yamashita, N. Akasaka, S. Ukai, S. Ohnuki, Journal of Nuclear Materials 367-370 (2007) 202–207.
[21] S. Yamashita, N. Akasaka, S. Ohnuki, Journal of Nuclear Materials 329-333 (2004) 377–381.
[22] M.-L. Lescoat, J. Ribis, Y. Chen, E.A. Marquis, E. Bordas, P. Trocellier, Y. Serruys, A. Gentils, O. Kaïtasov, Y. de Carlan, A. Legris, Acta Materialia 78 (2014) 328–340.
[23] D. Kaomi, A. Motta, M. Kirk, in: Transactions of the American Nuclear Society, volume 98, Anaheim, CA.
[24] M.-L. Lescoat, I. Monnet, J. Ribis, P. Dubuisson, Y. de Carlan, J.-M. Costantini, J. Malaplate, Journal of Nuclear Materials (2011).
[25] V.A. Skuratov, Journal of Nuclear Materials 442 (2013) 449–457.
[26] N. Akasaka, S. Yamashita, T. Yoshitake, S. Ukai, A. Kimura, Journal of Nuclear Materials 329-333 (2004) 1053–1056.

[27] H. Kishimoto, K. Yutani, R. Kasada, O. Hashitomi, A. Kimura, Journal of Nuclear Materials 367-370 (2007) 179–184.
[28] H. Kishimoto, R. Kasada, O. Hashitomi, A. Kimura, Journal of Nuclear Materials 386-388 (2009) 533–536.
[29] J.F. Ziegler, J.P. Biersack, 2013, Srim program. URL: http://www.srim.org/.
[30] L.R. Greenwood, R.K. Smither, SPECTER: neutron damage calculations for materials irradiations, Technical Report ANL/FPP/TM-197, Argonne National Laboratory, Lemont, IL, 1985.
[31] R.E. Stoller, M.B. Toloczko, G.S. Was, A.G. Certain, S. Dwaraknath, F.A. Garner, Nuclear Instruments and Methods in Physics Research B 310 (2013) 75–80.
[32] J. Gigax, E. Aydogan, T. Chen, D. Chen, Y. Wu, W.Y. Lo, Y. Yang, F.A. Garner, Journal of Nuclear Materials (submitted).
[33] G.S. Was, Fundamentals of radiation materials science: metals and alloys, Springer, 2007.
[34] D.S. Gelles, Journal of Nuclear Materials 233-237 (1996) 293–298.
[35] R. Schäublin, D.S. Gelles, M. Victoria, Journal of Nuclear Materials 307-311 (2002) 197–202.
[36] R. Schäublin, A. Ramar, N. Baluc, V. de Castro, M.A. Monge, T. Leguey, N. Schmid, C. Bonjour, Journal of Nuclear Materials 351 (2006) 247–260.
[37] P.J. Maziasz, R.L. Klueh, J.M. Vitek, Journal of Nuclear Materials 141-143 (1986) 929–937.
[38] O. Anderoglu, J. Van den Bosch, P. Hosemann, E. Stergar, B.H. Sencer, D. Bhattacharyya, R. Dickerson, P. Dickerson, M. Hartl, S.A. Maloy, Journal of Nuclear Materials 430 (2012) 194–204.
[39] J. Ribis, S. Lozano-Perez, Journal of Nuclear Materials 444 (2014) 314–322.
[40] Y. Miao, K. Mo, B. Cui, W.Y. Chen, M.K. Miller, K.A. Powers, V. McCreary, D. Gross, J. Almer, I.M. Robertson, J.F. Stubbins, Materials Characterization 101 (2015) 136–143.
[41] P. Dou, A. Kimura, T. Okuda, M. Inoue, S. Ukai, S. Ohnuki, T. Fujisawa, F. Abe, Journal of Nuclear Materials 417 (2011) 166–170.
[42] X. Mao, K.H. Oh, S.H. Kang, T.K. Kim, J. Jang, Acta Materialia 89 (2015) 141–152.
[43] K. Mo, Z. Zhou, Y. Miao, D. Yun, H.-M. Tung, G. Zhang, W. Chen, J. Almer, J.F. Stubbins, Journal of Nuclear Materials 455 (2014) 376–381.
[44] D.A. Porter, K.E. Easterling, M.Y. Sherif, Phase transformations in metals and alloys, 3rd ed., CRC Press, 2006.
[45] S. Ukai, Metal, ceramic and polymeric composites for various uses, ISBN 978-953-307-353-8, InTech, 2011.
[46] Y. Yazawa, T. Furuhara, T. Maki, Acta Materialia 52 (2004) 3727–3736.

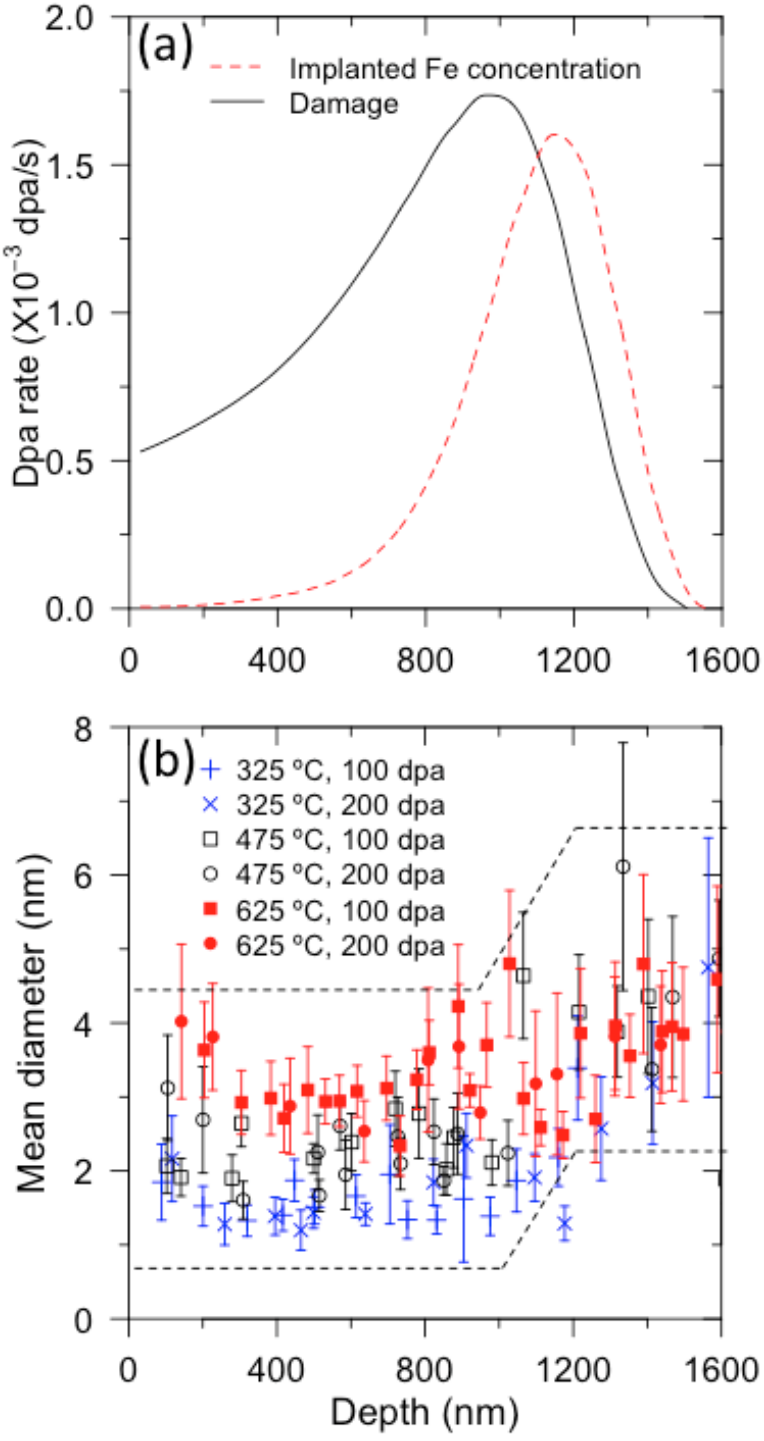

Figure 1: (a) SRIM simulation of 3.5 MeV self-ion irradiation of pure Fe, using a displacement threshold energy of 40 eV and the Kinchin-Pease option, (b) mean dispersoid diameter in tempered martensite phase as a function of depth, under different irradiation conditions.

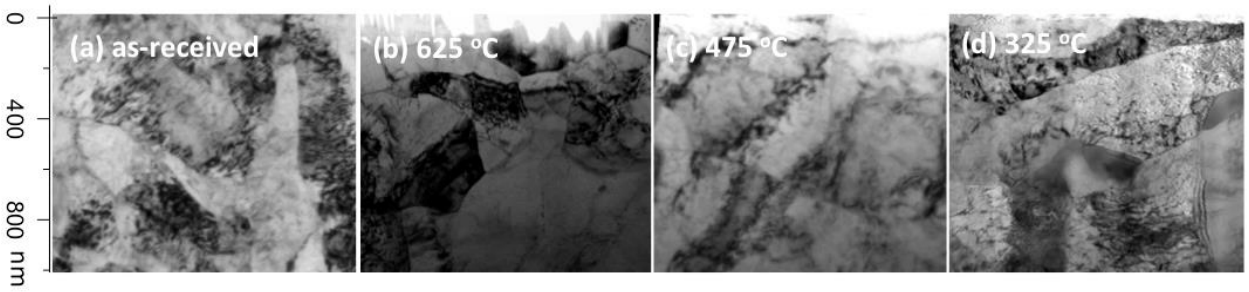

Figure 2: (a) Grain structure of as received sample, (b-d) irradiation surface (top) to peak dpa region (bottom) of samples receiving 200 peak dpa at 625 ◦ C, 475 ◦C and 325 ◦C, respectively.

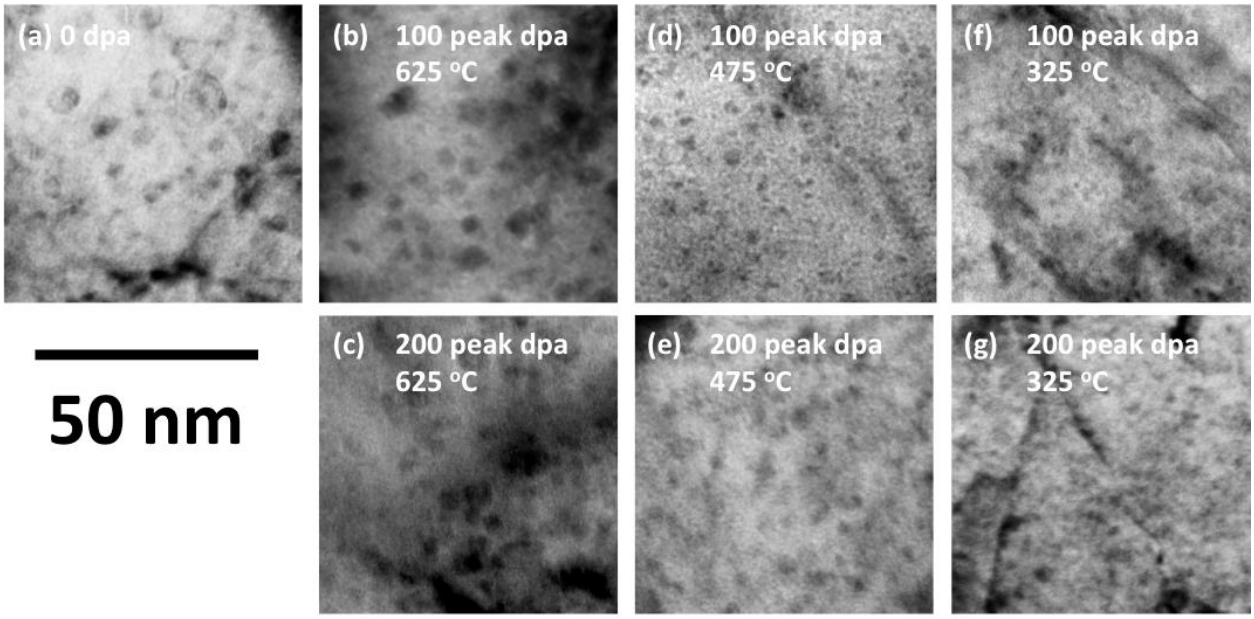

Figure 3: Bright field micrographs of dispersoids in tempered martensite phase under different irradiation conditions: (a) unirradiated sample, (b-c) 100 and 200 peak dpa samples irradiated at 625 ◦C, (d-e) 100 and 200 peak dpa samples irradiated at 475 ◦C, (f-g) 100 and 200 peak dpa samples irradiated at 325 ◦C

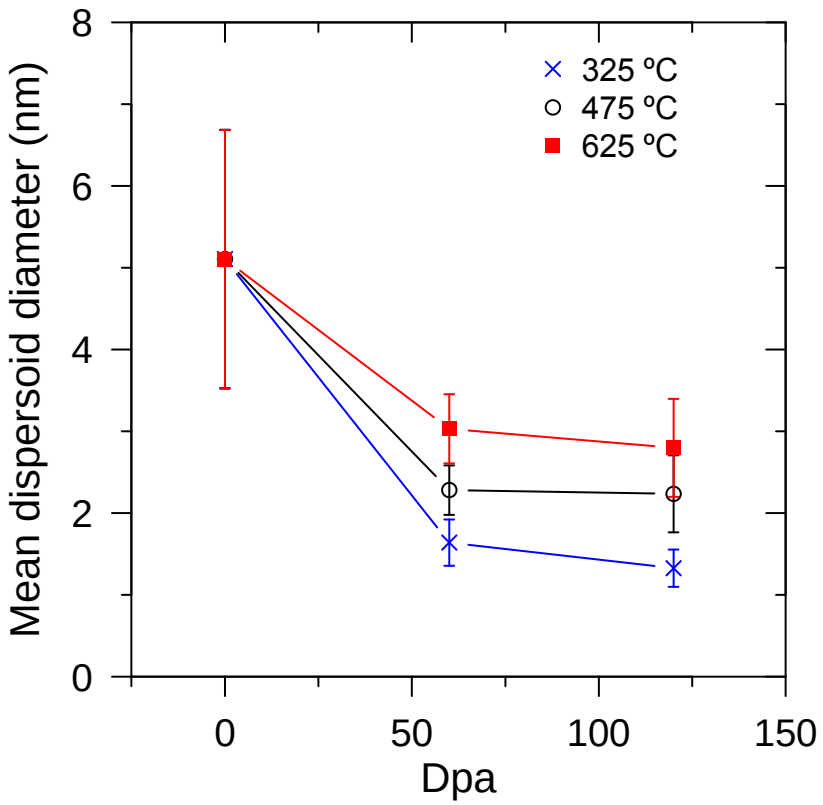

Figure 4: Mean dispersoid size as a function of local dpa for different irradiation temperatures, generated using data obtained from 400-700 nm depth

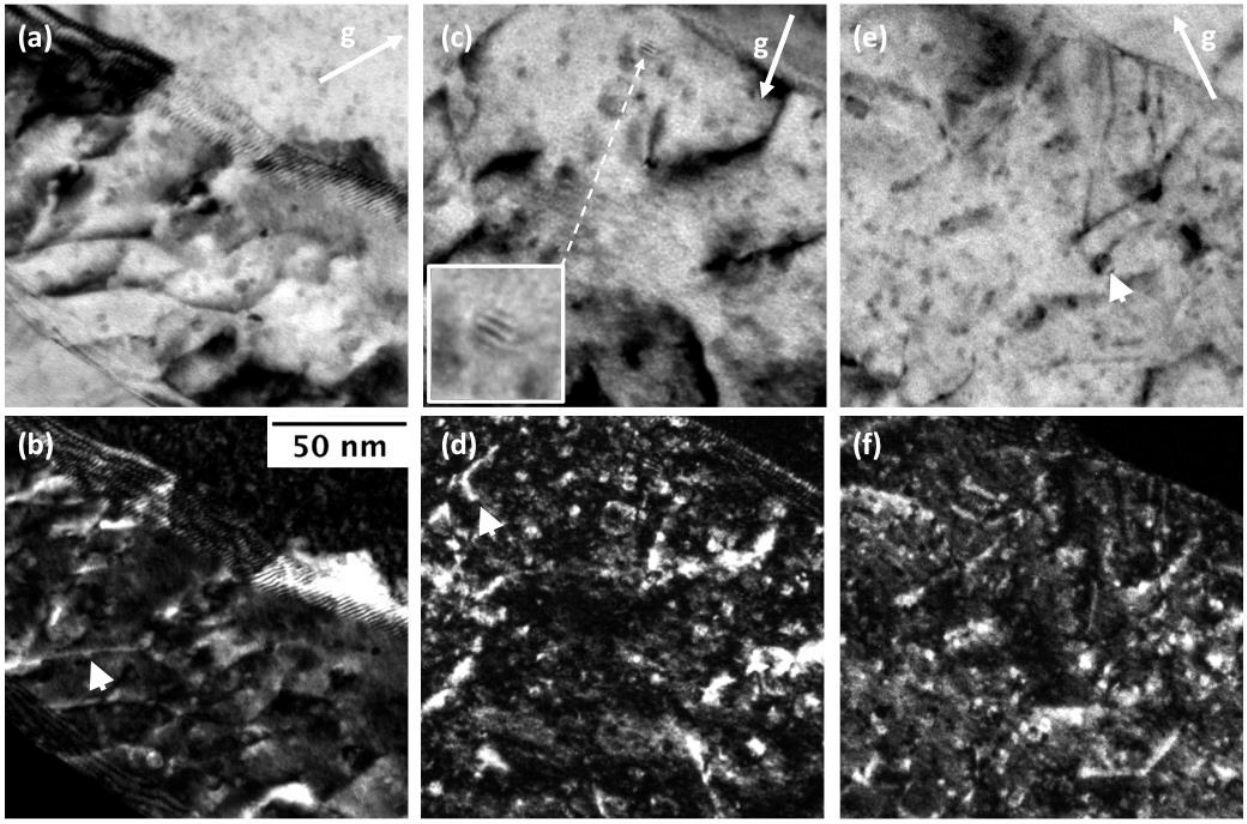

Figure 5: Bright field and weak beam dark field micrographs of tempered martensite grains obtained near $\mathbf{g}_{110}$: (a-b) unirradiated sample, (c-d) 625 ◦ C irradiated sample with ~65 dpa, (e-f) 475 ◦C irradiated sample with ~65dpa

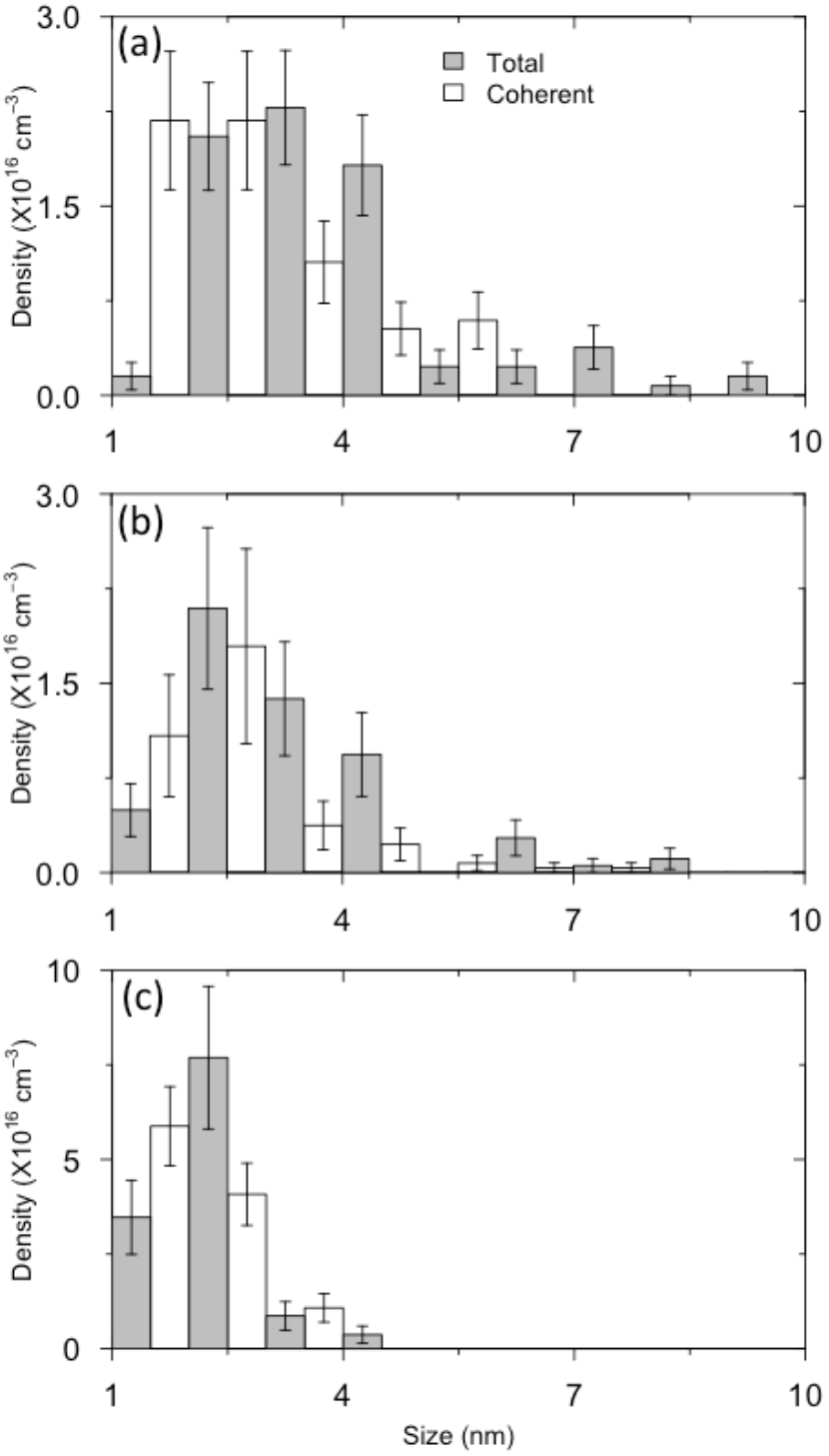

Figure 6: Size distributions of total and coherent dispersoid in tempered martensite phase: (a) unirradiated sample, (b) 625 ◦C irradiated sample, (c) 475 ◦C irradiated sample

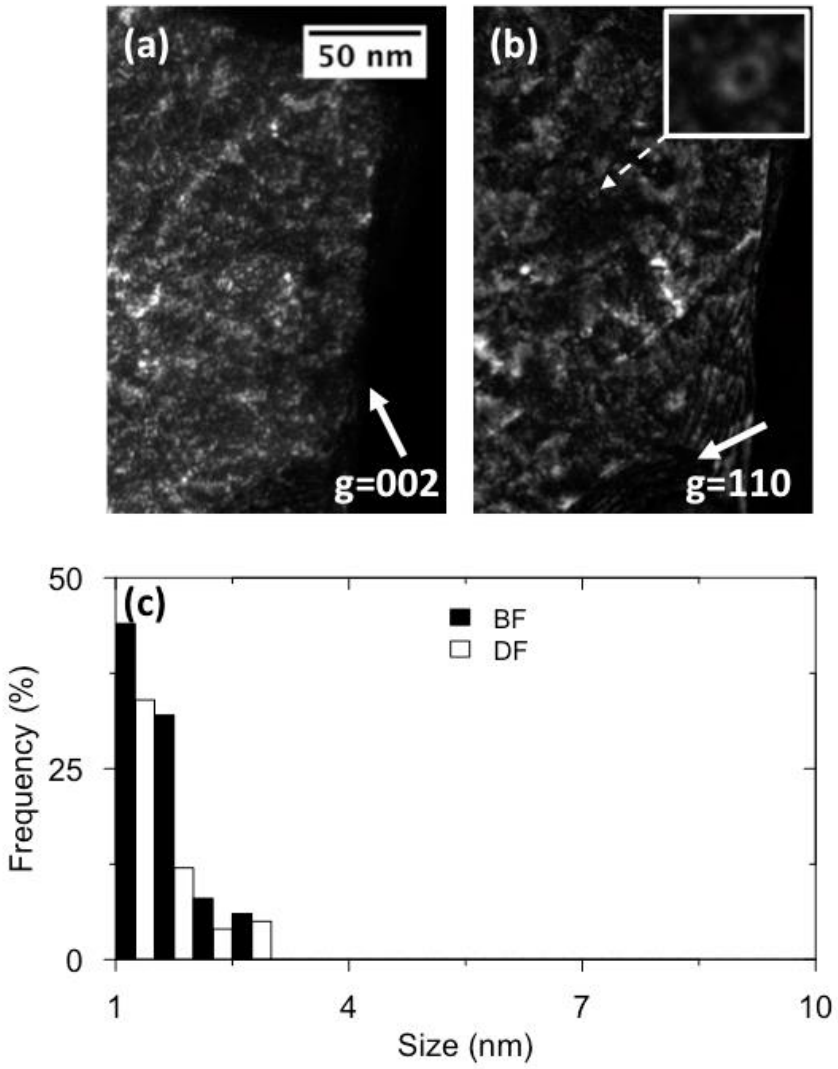

Figure 7: WBDF micrographs near (a) $\mathbf{g}_{002}$ and (b) $\mathbf{g}_{110}$ from a tempered-martensite grain receiving ~65 dpa at 325 ◦C, respectively; and (c) Feature size distribution obtained from BF and WBDF micrograph

Table 1: Chemical composition of the 12Cr ODS alloy investigated in this study

Component:	Fe	C	Cr	Ni	W	Ti	N	Ar	Y_2O_3	Ex. O
Weight, %:	85.74	0.16	11.52	0.34	1.44	0.28	0.007	0.006	0.36	0.144

Table 2: Dispersoid densities in tempered martensite grains, generated from a depth of ~ 500 nm from the irradiated surface for 100 peak dpa irradiated samples.

unit: $10^{16} cm^{-3}$	As-received	625°C irradiated	475°C irradiated
Total dispersoid ρ_t	7.6 ± 0.6	5.4 ± 1.4	12.4 ± 2.6
Coherent dispersoid ρ_c	6.6 ± 1.2	3.7 ± 1.5	11.4 ± 1.2
ρ_c:ρ_t	87%	69%	92%

Research highlight #6

Dispersoid stability in ion irradiated ODS alloy: dpa rate effect

The radiation response of oxide dispersoids in a Hf-doped oxide-dispersion-strengthened (ODS) alloy was studied by using 3.5 MeV Fe^{2+} self-ion irradiation at 475°C. The size changes of coherent and incoherent dispersoids were studied as a function of depth. Although there was up to 2.6 times of difference in local displacements-per-atom (dpa) rate at different characterization depths, the sizes of coherent and incoherent dispersoids did not show a noticeable dependence on dpa rate at depths up to the peak dpa. In order to explain the experimental observations, the diffusion of solute atoms (dissolved from dispersoids) must take into consideration defect-assisted-diffusion mechanisms. A high dpa rate results in enhanced dispersoid dissolution. On the other hand, dispersoid recovery is increased due to defect-assisted diffusion. Therefore, the two effects are balanced, leading to a relative insensitivity of dispersoid size to dpa rate. The study further shows that both coherent and incoherent dispersoids shrink during irradiation but the final equilibrium sizes of coherent dispersoids are smaller than that of incoherent dispersoids, arising primarily from a difference of their interfacial energies. The incoherent dispersoids undergo more significant volume reduction under irradiation than coherent dispersoids do.

F6-1. Introduction

Oxide-dispersion-strengthened (ODS) alloys represent one class of candidate alloys with promising application in nuclear reactors due to their good creep resistance and high temperature strength [1-4]. The oxide dispersions help to stabilize grain boundaries, block dislocation motion, and act as possible defect sinks for point defect trapping and defect annihilation [2,7,8]. However, the superior performance of ODS alloys, in general, depends on the stability and structural morphologies of the dispersoids. Numerous studies have shown that under ion irradiation, dispersoids are not stable in their sizes, densities, volume fractions or chemical compositions [5, 6, 9-16]. Wharry et al. summarized a wide variety of irradiation-induced changes under different irradiation conditions including both dispersoid shrinkage and growth, suggesting that multiple active mechanisms influencing dispersoid irradiation evolution [10]. Recent studies have brought insights into the complicated nature of dispersoid stability under irradiation [11, 12, 14], such as cascade morphology effect and dose rate effect [11], chemical composition effect [12], and dissolution-reprecipitation mechanism [14]. Swenson et al. conducted a study comparing neutron, proton and heavy ion irradiation for the dose rate effects in dispersoid stability [11]. Their study has four orders of magnitude in dose rates, and the dose rate effect is coupled with different cascade morphologies[11]. Therefore, it is valuable to investigate the dose rate effects by using one single particle type, which is the motivation of the present study.

The dispersoid evolution under irradiation is governed by two competing effects: dispersoid dissolution due to damage cascade recoiling and recovery arising from back-diffusion. The shrinkage of dispersoids under irradiation is described by [17].

$$\frac{dr}{dt} = -K\psi \qquad 1)$$

where r is the dispersoid radius, t is time, K is the dpa (displacements per atom) rate, ψ is a parameter to describe the efficiency of damage cascades to dissolve dispersoids.

The dissolution of dispersoids leads to a concentration increase in the matrix surrounding dispersoids. Driven by a concentration gradient, back-diffusion of recoiled solutes tends to increase the dispersoid size. When these two competing effects are balanced, dispersoid sizes approach to an equilibrium value, r_e, as calculated by [18].

$$r_s = \frac{D}{K\psi} \cdot \frac{c - c_r}{c_p - c_r} \quad (2)$$

where D is the solute diffusion coefficient influenced by radiation-induced defects, c is the solute concentration in the matrix, c_p is the solute concentration in the dispersoid, c_r is the solubility limit at the dispersoid-matrix interface. The solubility limit at the interface is expressed as [18]

$$c_r = c_\infty \exp\left(\frac{2\gamma_i \upsilon_{at}}{kTr}\right) \quad (3)$$

where c_∞ is the solubility for a flat interface (r=∞), γ_i is the unit interfacial energy at the dispersoid-matrix interface, υ_{at} is the average atomic volume in the dispersoid, T is the temperature, and k is the Boltzmann constant.

If Eq. 2 is the only effect governing the dispersoid evolution under irradiation and if diffusivity D is not affected by dose rates, a strong dose-rate dependency of dispersoid size should have been observed. However, this was not observed in earlier studies [6]. Hence, it is suggested that D needs to consider dose rate effect, which can counterbalance dispersoid dissolution and let dispersoid diameters become insensitive to dose rate effects.

Heavy ion irradiation can induce solute redistribution and has been modelled via rate theory [19,20]. Solute migration mediated by defects produced by irradiation (i.e. vacancies and self-interstitial atoms) was shown to result in solute gradients that, in some cases, mirror irradiation-induced defect profiles. The sensitivities of both dispersoid dissolution and solute migration to dpa rates can be well tested in ion irradiation experiments through depth profiling of void evolution. Although the magnitudes of dpa rate difference are limited, the study has certain advantage of minimizing beam-heating effects, since only one beam current is used. Therefore, we utilized heavy ion irradiation in the present study to examine the oxide evolution in an Hf-doped ODS alloy. The Hf-doped alloy is specifically selected since it is extreme swelling resistant, which minimizes the complexity from dispersoid-void interactions.

F6-2. Experimental procedure

An Hf-doped ferritic ODS alloy fabricated by Kobelco Research Company was used in this study. The details of fabrication procedure are reported elsewhere [21]. First, the ferritic steel powder and Y_2O_3 powder are mechanically alloyed and agitated for up to 48 hrs under argon gas atmosphere. Then, it is degassed at high temperature in 0.1 Pa vacuum for 2 hrs, followed by hot extrusion at 1423 K. Hf was intentionally added for dispersoid refinement [22]. The chemical composition of this alloy is provided in Table I. The alloy was cut into specimens of 5 mm×3 mm×2mm, and mechanically polished down to a 0.7 mm thickness by using SiC paper (down to 4000 grit). The final polishing step used a 0.04 micron alumina suspension. The sample was then electropolished at room temperature using a mixture of 7% perchloric acid and 93% acetic acid. The graphite cathode and the sample were biased at a voltage of 2 V and separated at a distance of 4 cm. A magnetic stirring bar was kept spinning while polishing, and the total polishing time was 20 sec.

The specimen was irradiated at 475°C by 3.5 MeV Fe^{2+} ions to a fluence of 9.54×10^{16} ions/cm^2, equivalent to 100 peak dpa, based on the Stopping and Range of Ions in Matter (SRIM) [30]. The SRIM calculation uses the Kinchin-Pease option and an Fe displacement threshold energy of 40 eV [31]. The temperature was selected since it is close to maximum swelling temperature of ferritic alloys [23-26]. The beam was static as the best practice to avoid the rastering/pulse beam effect [27]. The beam spot was

about 6 mm×6 mm and the current was controlled to be ~200 nA. Liquid nitrogen cold traps located in the beam line and target chamber were used during irradiation to keep high vacuum (<10^{-8} torr). To reduce beam-induced carbon contamination, multiple beam deflectors were used to filter the carbon contaminants off the Fe beam trajectories. Details of these instrumental setups to reduce beam contamination can be found elsewhere [28,29].

Irradiated samples were characterized by transmission electron microscopy (TEM) with TEM specimens prepared by using the focused ion beam (FIB) lift-out technique. The FIB specimen size was ~10 μm × ~7 μm × ~200 nm in the first-stage of preparation. Then 30 keV Ga beam was changed to 5 keV for the second-stage fine thinning to a thickness of ~100 nm. TEM characterization was performed using 200 keV FEI Tecnai G2 F20 Super-Twin and FEI Tecnai F20, and FIB was performed using Tescan Lyra-3. Bright field (BF), weak beam dark field (WBDF), scanning transmission electron microscopy (STEM) – high angle annular dark field (HAADF) and electron energy loss spectroscopy (EELS) were used to characterize the samples. Dispersoids size measurement is challenging for ultra-fine dispersoids (< 1 nm) due to the resolution limit of TEM. Atom probe tomography (APT) is more appropriate to characterize small dispersoids. Recent comparison studies suggest that sizes and densities of small oxide dispersoids measured by TEM and APT are comparable to each other [9]. The dispersoid sizes in the present study, although small, are still in the reliable characterization capability of TEM. Furthermore, TEM is critical for the present study in order to check coherency of dispersoids.

Table I Composition of Hf-doped ODS alloy (wt.%)

Fe	Cr	C	Si	Mn	P	S	W	Al	Ti	Hf	Y_2O_3	Ex. O
Bal.	15.44	0.024	0.03	0.01	<0.005	0.002	1.80	3.90	0.12	0.59	0.33	0.10

F6-3. Results

Figs. 1a and 1b compare TEM cross-sectional micrographs before and after irradiation. The upper white dashed lines designate the sample surface and lower white dashed line in Fig. b defines the end of the ion bombarded region. The red solid line and red dashed line superimposed on Fig. b are the dpa profile and the Fe implant profile, respectively, calculated by using the SRIM code [29]. There are no noticeable changes in grain morphologies after irradiation. The inset in Fig. 1a shows typical oxide dispersoid morphologies in the as-received condition. Dispersoid size in the unirradiated specimen (Fig. 1a) were measured to be 5.3±1.1 nm, while the dispersoid sizes were measured to be 4.9±0.7 nm in the region beyond the ion range in the irradiated specimen (Fig. 1b). Hence, thermal annealing (corresponding to depths beyond the bombarded region) does not significantly change the dispersoid size. In both samples, there are large particles exhibiting either white contrast or dark contrast. The large particles (>100 nm) of white contrast are Hf-Ti-O, while the large particles (>50 nm) of dark contrast are Al_2O_3. Ar gas bubbles over 50 nm diameter were occasionally observed in the matrix as well. These particles and bubbles were introduced during alloy fabrication and their densities are very low. Hence, they are not subjects of interest in the present study.

Fig. 2 shows a TEM cross-sectional micrograph of an irradiated sample, superimposed with the SRIM dpa and Fe implant profiles. The dpa peaks at a depth of ~1000 nm and the Fe implant peaks at ~1200 nm. In order to study the local dpa rate effect, five locations (as marked by black dashed lines) at depths of 250 nm (6.71×10^{-4} dpa/s), 650 nm (1.19×10^{-3} dpa/s), 1000 nm (1.73×10^{-3} dpa/s), 1200 nm (1.06×10^{-3} dpa/s), and 2000 nm (0 dpa/s) are characterized.

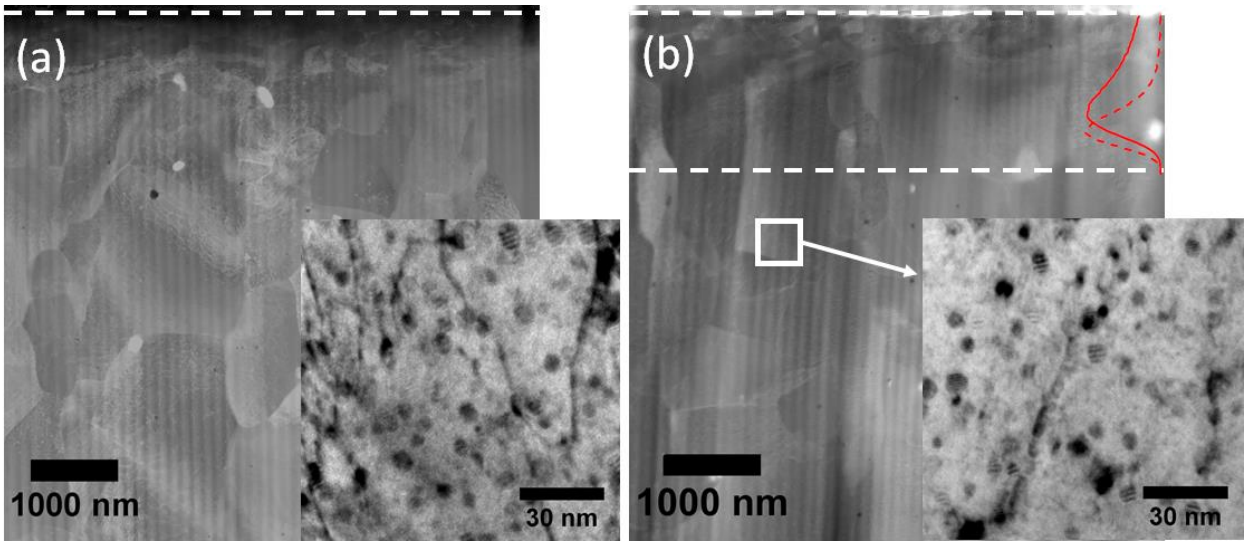

Figure 1 – STEM-HAADF and TEM BF micrographs of Hf-doped ODS (a) before irradiation and (b) after 100 peak dpa irradiation. SRIM calculation of dpa (red solid line) and Fe implant (red dashed line) are superimposed in (b). Two white dashed lines in (b) refer to boundaries of the damaged region.

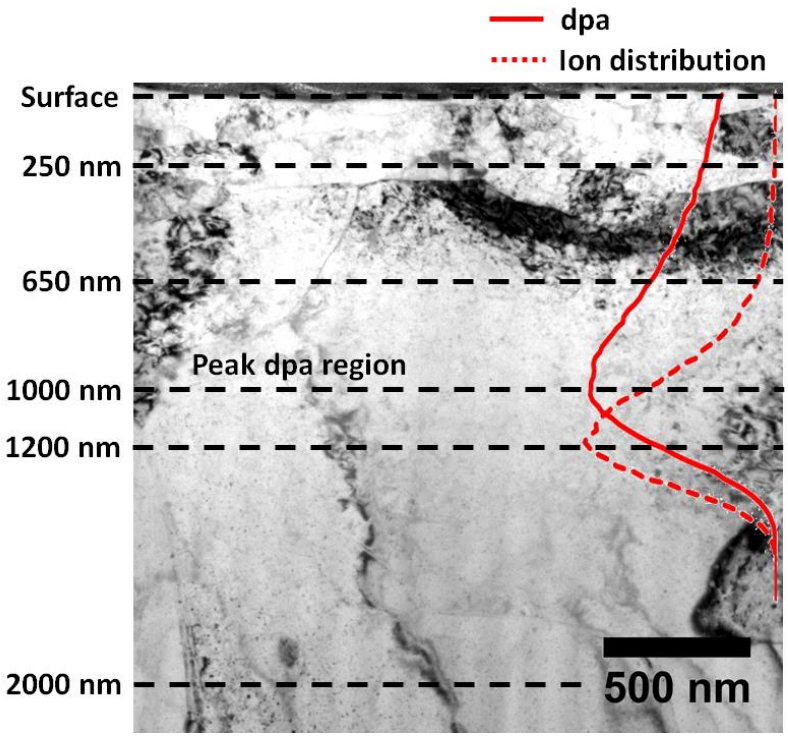

Figure 2 – TEM bright field image of 100 peak dpa irradiated Hf-doped ODS. Five different depth regions are characterized, as marked by black dashed lines. SRIM-calculated dpa and Fe ion distribution profiles are superimposed.

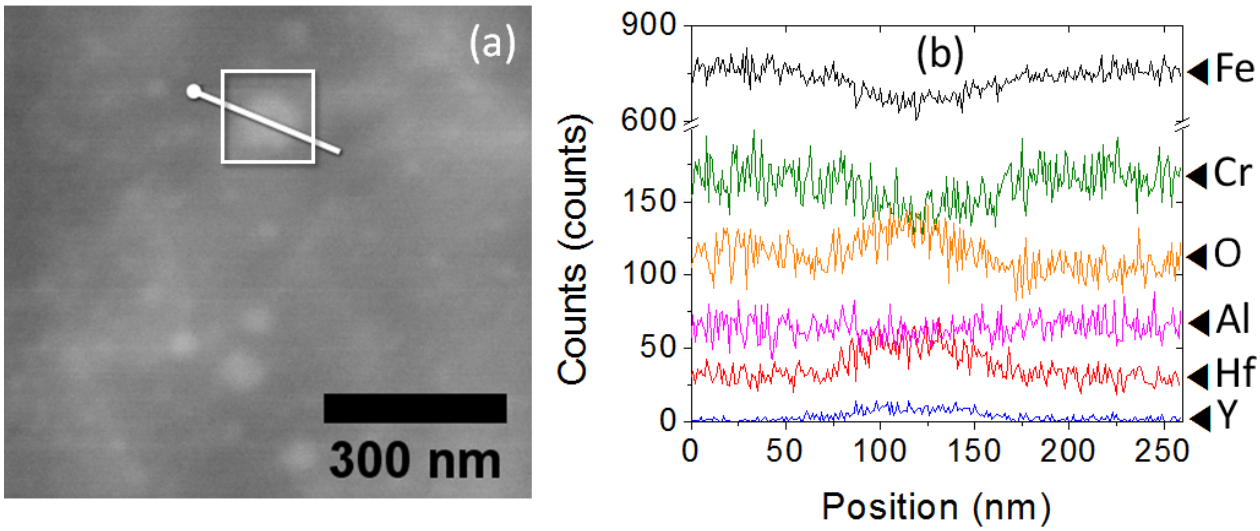

Figure 3 – (a) STEM-HAADF image of an oxide particle with a line referring to the path of composition scanning analysis (white line), and a square referring to the area profiling analysis (white square), (b) EDS line scan results from white line. All results were obtained from an unirradiated sample.

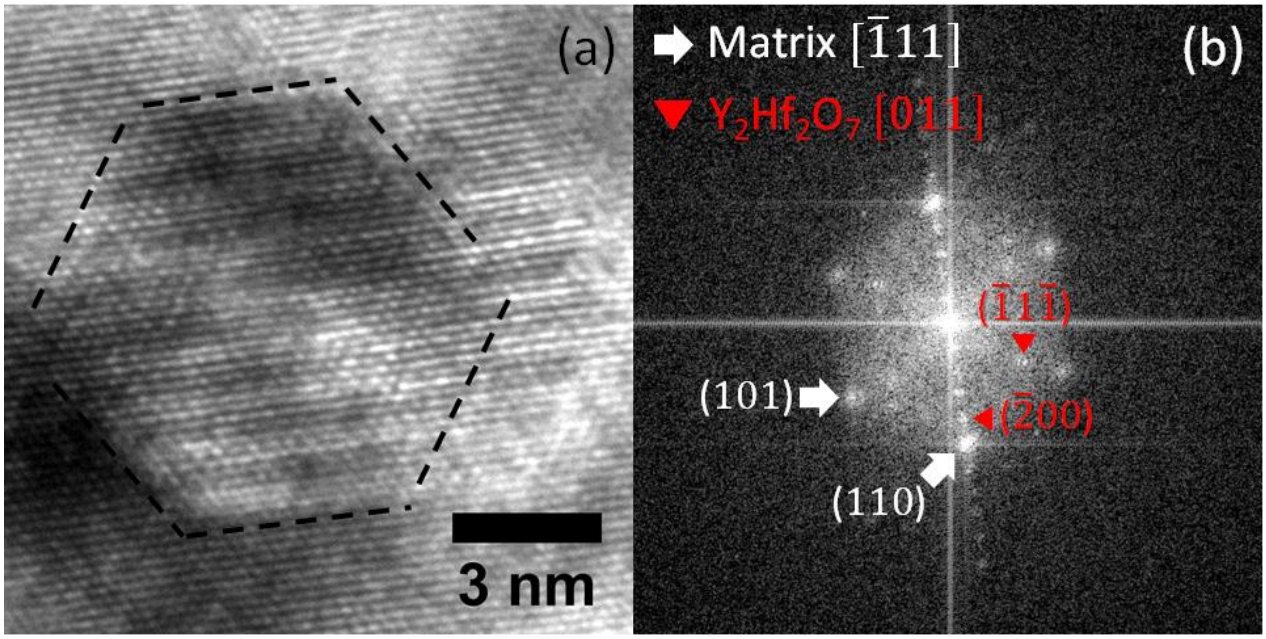

Figure 4 – (a) HRTEM image of a dispersoid in an unirradiated sample with dispersoid-matrix interfaces marked by black dashed lines and (b) the corresponding Fast Fourier Transformation (FFT) image.

Dispersoids in the unirradiated sample were analyzed with EDS and HRTEM for chemical composition and structural information. HRTEM is useful to tell interfacial coherency of dispersoids and matrix. Recent studies have shown that the chemical composition of dispersoid plays an important role in the microstructure and radiation stability of the materials [11-13,37]. Fig. 3a shows a STEM-HAADF image of the oxide particle and EDS analysis. As shown in Fig. 3b, the Fe and Cr yields are slightly decreased within the particle, and the yield from Al statistically fluctuates without a conclusive compositional variation. O, Hf, and Y enrichments were observed within the particle.

Fig. 4a shows a high resolution TEM (HRTEM) micrograph of an oxide particle of ~8 nm in diameter, taken from the $[\bar{1}11]$ zone axis of the matrix. The particle has a faceted morphology, which is a sign of developing coherent interfaces. Fig. 4b shows the corresponding Fast Fourier Transform (FFT) image, with the patterns of the matrix marked with white arrows and the patterns of the particle marked with red triangles. The patterns of the particle suggest a fluorite structure of $Y_2Hf_2O_7$. The FFT pattern also shows matrix-oxide interface coherency of $(110)_{Matrix}//(\bar{2}00)_{Particle}$, and $[\bar{1}11]_{Matrix}//[011]_{Particle}$.

Fig. 5a plots the damage and Fe implant profiles, with arrows marking the regions locally characterized by TEM. Figs. 5b-f show the bright field and dark field micrographs at depths of 250 nm, 650 nm, 1000 nm, 1200 nm and 2000 nm, respectively. The above depths correspond to 39 dpa (at 250 nm, 6.7×10^{-4} dpa/s), 69 dpa (at 650 nm, 1.2×10^{-3} dpa/s), 100 dpa (at 1000 nm, 1.7×10^{-3} dpa/s), 61 dpa (at 1200 nm, 1.1×10^{-3} dpa/s), and 0 dpa (at 2000 nm). The particles having dark contrast in the bright field TEM images are oxide dispersoids. Similar to the previous studies by Chen et al. [6], when the $\mathbf{g}_{110}$ direction is excited, dispersoids coherent to (110) of the matrix appear as bright features in the dark field imaging. Both dispersoid types appear dark or gray in the bright field images, but only coherent dispersoids appear bright in the dark field images. Hence, the comparison between bright field and dark field images can differentiate coherent and incoherent dispersoids. Note that, as we selected one of the six (110) planes by selecting one specific $\mathbf{g}_{110}$ direction to check the coherency, there is a possibility that some coherent dispersoids may not show up in the dark field image. However, as both coherent and incoherent dispersoid diameters are smaller than 10 nm, we assumed that all six (110) planes will develop the same coherency with the matrix, and one dark field image taken from one specific $\mathbf{g}_{110}$ direction can represent other five directions. For large dispersoids in Fig. 5f, they appear with Moiré fringes, suggesting a slight lattice mismatch of the dispersoid to $(110)_M$. These semi-coherent dispersoids also appear as bright in the dark field images. In comparison with the dispersoids at 2000 nm, which is beyond the Fe range, all dispersoids within the irradiated regions are smaller.

The dispersoid size distributions at different depths are summarized in Fig. 6. At a depth of 2000 nm, corresponding to 0 dpa, Fig. 6e shows both incoherent and coherent dispersoids having wide size distributions from ~3 nm to ~8 nm. At the same depth, the incoherent dispersoids distributions are peaked at a size of ~6 nm while the coherent ones are peaked at ~3.5 nm. Within the irradiated regions, both types of dispersoids shrunk in comparison with dispersoids at 2000 nm depth (0 dpa). The mean sizes of incoherent dispersoids are systematically larger than that of coherent dispersoids.

Fig. 7a summarizes the size distributions at different depths. For each depth, more than 70 oxide particles were characterized. Although ion irradiation shrinks dispersoids, incoherent dispersoids are still statistically larger than coherent dispersoids at all depths. Within the irradiation region shallower than 1000 nm, the mean sizes of dispersoids of both types do not show obvious depth (or equivalently, dpa and dpa rate) dependencies. The mean sizes of incoherent dispersoids are 1.9±0.3 nm at depth 250 nm, 1.9±0.6 nm at depth 650 nm, 1.8±0.4 nm at depth 1000 nm, 3.1±0.7 nm at depth 1200 nm, and 5.4±1.0 nm at depth 2000 nm. The mean sizes of coherent dispersoids are 1.8±0.4 nm, 1.6±0.5 nm, 1.6±0.3 nm, 2.6±0.8 nm, and 4.4±1.0 nm at the corresponding depths, respectively.

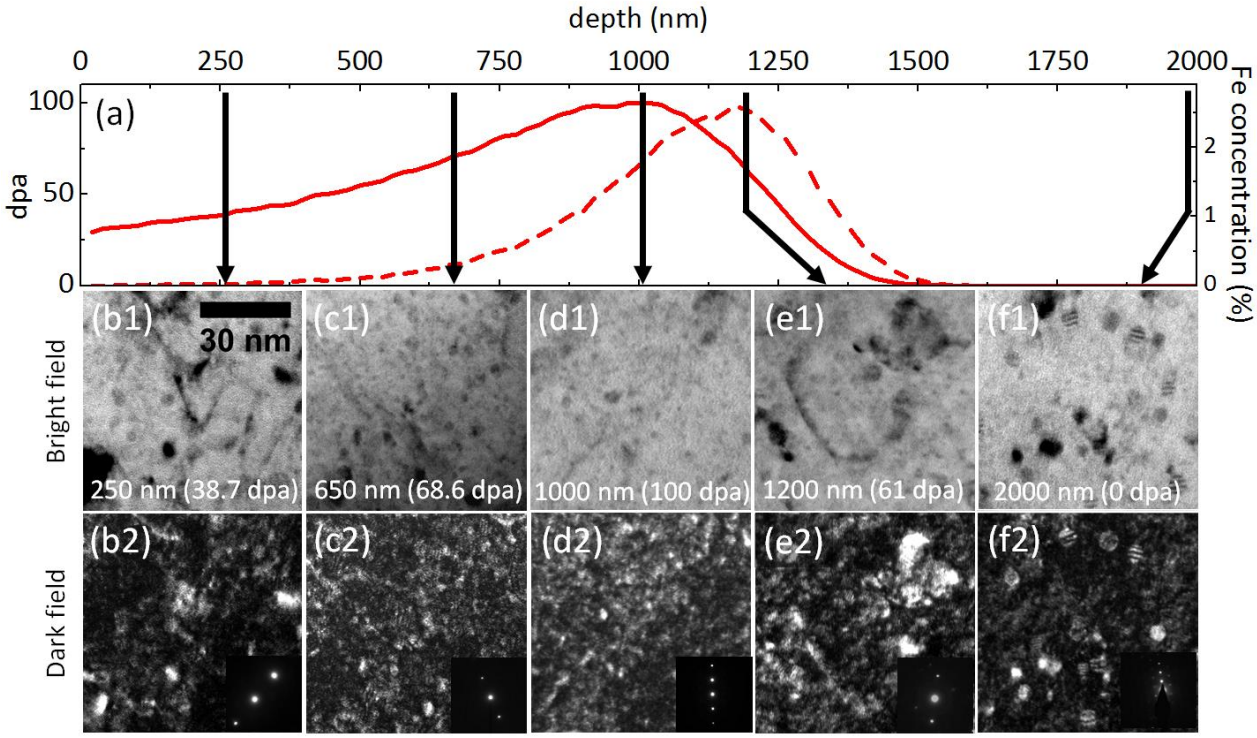

Figure 5 – (a) Dpa (red solid line) and Fe implant (red dashed line) profiles, and (b1-f1) BF micrographs at depths of 250 nm, 650 nm, 1000 nm, 1200 nm, and 2000 nm, respectively, and (b2-f2) corresponding WBDF micrographs and TEM diffraction patterns.

Fig. 7b plots the dispersoid densities as a function of depth. Coherent dispersoids are systematically denser than incoherent dispersoids. Dispersoid densities at 250 nm and 650 nm are comparable to each other (about ~5×10^{23} m^{-3} for coherent dispersoids and ~3×10^{23} m^{-3} for incoherent dispersoids for both depths). At 1000 nm corresponding to the dpa peak, the dispersoid densities are higher (~8×10^{23} m^{-3} for coherent dispersoids, and ~4×10^{23} m^{-3} for incoherent dispersoids). The total dispersoid density at 1000 nm is about 1.5 times that at 250 nm.

Fig. 7c presents the dispersoid volume fraction. The volume fractions of coherent and incoherent dispersoids are comparable to each other within the irradiated region. For the irradiated region at depths ≤1200 nm, the total dispersoid volume fractions are systematically lower than that out of the irradiation region. The missing solute atoms can either diffuse towards the surface or be dissolved into the matrix under irradiation. Due to the fact that there is no enhancement of yttrium-rich precipitates near the surface, it is most likely that these solutes are dissolved in the matrix. Based on the volume fraction difference, the atomic density of dissolved solute atoms is estimated to around 0.18 %. It is worth noting that, under irradiation, coherent particles undergo a much less significant volume reduction than incoherent particles do, suggesting that, at the irradiation temperature of 475 °C, coherent particles are more stable than incoherent particles. This agrees with results of previous studies by Chen et al. [5,6].

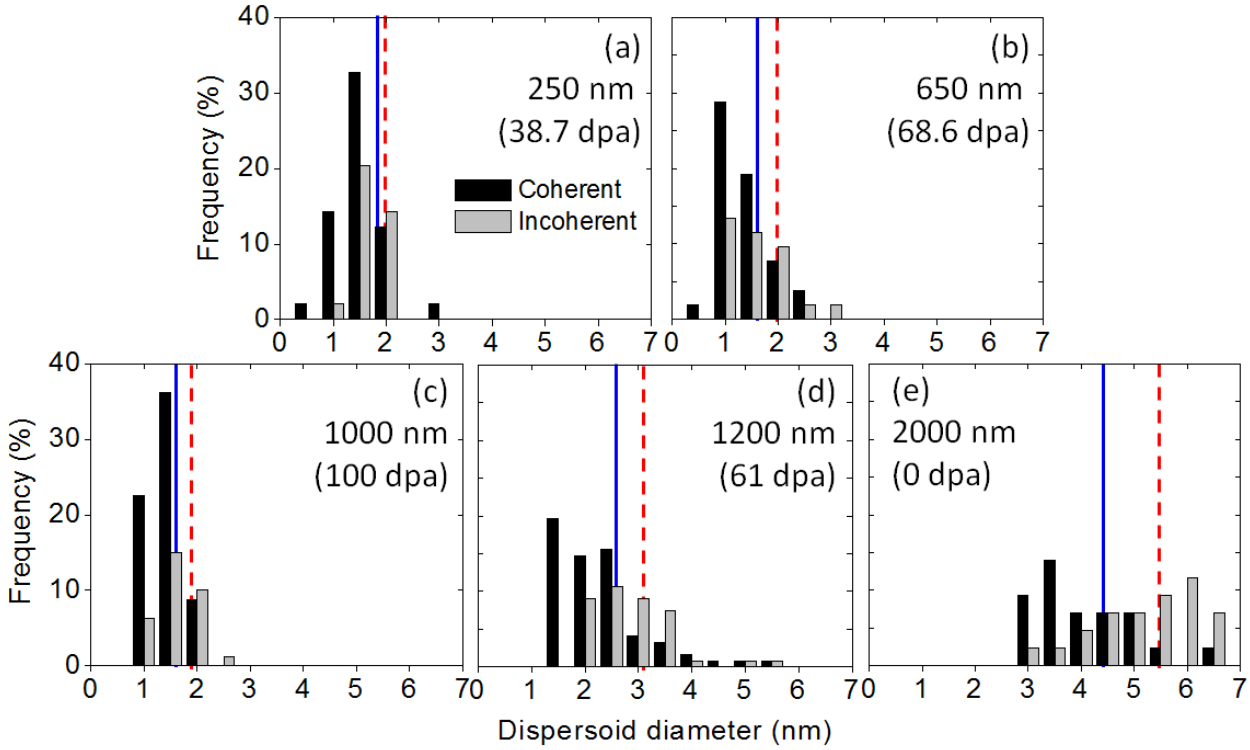

Figure 6 – Dispersoid size distributions of irradiated Hf ODS alloy at depths of (a) 250 nm (38.7 dpa), (b) 650 nm (68.6 dpa), (c) 1000 nm (100 dpa), (d) 1200 nm (61 dpa), and (e) 2000 nm (0 dpa), respectively. The dark bars refer to coherent dispersoids and the gray bars refer to incoherent dispersoids. The solid blue lines and dashed red lines refer to mean diameters of coherent dispersoids and incoherent dispersoids, respectively.

As shown in Fig. 7d, total dispersoid densities within the irradiation region (at depths ≤1200 nm) are systematically higher than that beyond the irradiated region. The total dispersoid density at 2000 nm is 7.9×10^{22} m^{-3}, while the density at 1000 nm is 1.17×10^{24} m^{-3}, larger by a factor of 15. The much higher dispersoid densities must result from nucleation of new dispersoids. The highest dispersoid density occurs at the dpa peak. Several mechanisms can contribute to this: (1) with the highest local dpa rates, the effective diffusivity of solute, according to combined Eqs. (5) and (6), is peaked. Hence the likelihood of solute clustering for forming new nucleation sites is peaked; (2) the high density of small defect clusters which form at peak dpa region may serve as nucleation sites for dispersoids; and (3) the likelihood of directly breaking large dispersoids into smaller ones is increased in the peak dpa region due to the higher density of damage cascades.

The observation that coherent dispersoids are systematically smaller than incoherent dispersoids within the irradiated region agrees with predictions of Eq. (3) in which γ_i of coherent dispersoids is smaller than that of incoherent dispersoids. The interfacial energy of coherent interfaces was reported by Ribs et al. to be 0.26 - 0.29 J/m^2 [34], while the interfacial energy of incoherent or semi-coherent interfaces was reported by Howe to be 0.3-2.5 J/m^2 energy range [35]. Using the experimentally extracted c (=0.18 %) in the present study as the upper limit of c_r (since r_s in Eq. (2) must be positive), and using the estimated c_∞ (=0.013% at 475 °C) [36], we obtain the upper limit of γ_i to be about 0.4 J/m^2 in the irradiated region and 1.0 J/m^2 in the damage-free region in the present study.

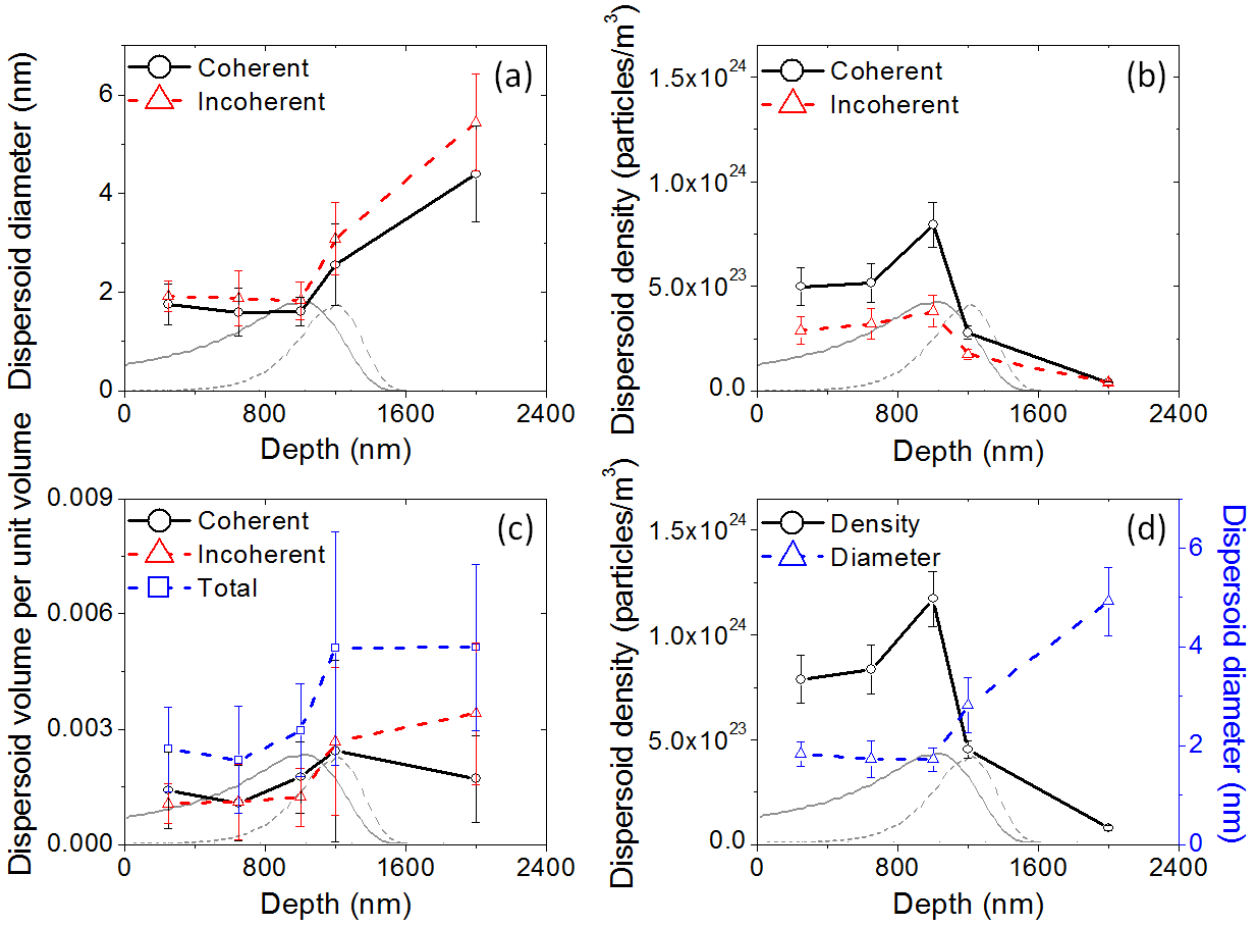

Figure 7 – Depth distributions of (a) dispersoid diameter, (b) dispersoid density, (c) dispersoid volume fraction, and (d) total dispersoid density and average diameter. Dpa (gray solid line) and Fe implant (gray dashed line) profiles are superimposed on each graph.

F6-4. Discussion

According to Eq. (2) and further assuming that D is a constant without radiation enhancement, the equilibrium dispersoid size r_e should be inversely proportional to the dpa rate K. At depths of 250 nm, 650 nm, and 1000 nm, their dpa rate ratios are 1:1.8:2.6. Figure 8 plots the dpa rates. In a comparison, experimentally measured r_e values are roughly a constant. To explain the observations, we believe that solute diffusion must be strongly defect-assisted, as explained below.

At high temperatures in the presence of defect sinks, defect annihilation at the sinks plays a dominant role in determining defect concentrations, and therefore point defect recombination does not contribute as much. Under quasi-steady state condition, local defect reactions are governed by equations [32]

$$\frac{dC_V}{dt} = K - K_{VS}C_S C_V, \text{ and } \frac{dC_I}{dt} = K - K_{IS}C_S C_I, \quad (4)$$

where C_V, C_I and C_S are vacancy, interstitial and sink concentrations, respectively. K_{VS} and K_{IS} are vacancy-sink reaction, and interstitial-sink reaction rate coefficients, respectively. Defect populations first increase linearly with irradiation time and approach to an equilibrium steady state with constant defect concentrations expressed by

$$C_{V_e} = \frac{K}{K_{VS}C_S}, \text{ and } C_{I_e} = \frac{K}{K_{IS}C_S} \quad (5)$$

On the other hand, for solute atoms which diffuse via interaction with point defects, a general expression of their diffusivity is given by [33]

$$D = f_V D_V C_V + f_I D_I C_I + \cdots \quad (6)$$

where f is a weight factor determined by both diffusion mechanism and diffusion correlation. D_V and D_I are the diffusivities of vacancies and interstitials, respectively. The defect-assisted diffusion can extend to other defect types such as di-interstitial or di-vacancy. For simplicity, we ignore the mechanisms involving defect clusters.

Combining Eqs. (2), (5) and (6), we obtain

$$r_e = \frac{f_V D_V/K_{VS} + f_I D_I/K_{IS}}{\psi C_S} \cdot \frac{c - c_r}{c_p - c_r} \quad (7)$$

Hence, there is no dependence of r_e on dpa rate *K*.

The defect sinks (C_S) can be dislocations, voids, or oxide dispersoids. In our irradiated samples, voids are not observed due to the good swelling resistance of the alloy matrix. Therefore, the most dominant sinks are the dispersoids themselves. As an approximation, we can use local total dispersoid density to represent C_S and calculate r_e by using Eq. (7). As shown in Fig. 8, the predicted r_e values are reasonably close to the experimentally measured values.

For Eq. (4), we assume a high temperature condition in which defect recombination contributes less in comparison with defect annihilation at sinks. Hence, interstitial-vacancy recombination is ignored. Even it is not a high temperature condition, Eq. 4 is still valid for the case having high density defect sinks such as dispersoids in the present case. In other words, it is valid for the condition that point defects find sinks first before they find their counterpart defects for recombination [32]. For a different and extreme case in which the temperature is low and the defect sink density is also low, defect reactions are governed by the defect creation rate and interstitial-vacancy recombination only (ignoring defect-sink interaction), the defect reaction equation and the quasi-steady state defect concentration are expressed as [32]

$$\frac{dC}{dt} = K - K_{IV}C^2$$

$$C_e\left(= C_{I_e} = C_{V_e}\right) = \left(\frac{K}{K_{IV}}\right)^{1/2} \quad (8)$$

Note in this case, the defect concentrations under quasi-steady state are proportional to $\sqrt{K}$, instead of K. After substituting C_e into Eq. (6) for *D*, Eq. (2) leads to a r_e dependence on $1/\sqrt{K}$, a dependence which is quite weak. The defect concentrations under quasi-steady states of various conditions (low temperature vs. high temperature and low sink density vs. high sink density) have been

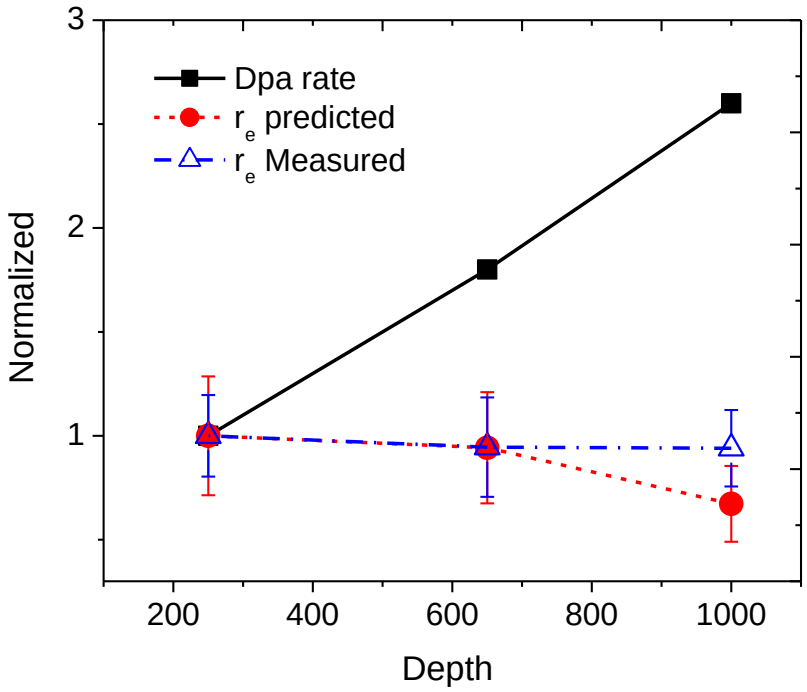

Figure 8 – Depth dependence of dpa rates, experimentally measured r_e and predicated r_e by using Eq. 7. All values are normalized to that at 250 nm.

systematically summarized by Was [32]. Various conditions lead to either a K dependence or $\sqrt{K}$ dependence of quasi-steady-state defect concentrations. Regardless of the complexity arising from variations in sink density and temperatures, the final r_e becomes either weakly dependent or completely independent of local dpa rates. In both cases discussed (Eqs. 5 and 8), we assume that quasi-steady states are reached. Our previous studies show that 3.5 MeV ion irradiation of a similar ODS alloy at 475°C leads to saturated dispersoid diameters at doses of 50 peak dpa and beyond. Hence, we believe this assumption is valid. Otherwise, dispersoids will continue to evolve under changing defect densities.

Another significant consequence of the present study is to justify the use of ion irradiation to simulate neutron irradiation. If dispersoid sizes have weak or no dependence on dpa rates, then accelerated testing using accelerated ion irradiation can more accurately predict dispersoid evolution in reactors. However, we need to point out that the currently study is limited to dpa rate differences that are less than one order of magnitude, while dpa rates in accelerator testing are typically a few orders of magnitude higher than those in reactors. Hence, more systematic comparative studies involving larger dpa rates (by adjusting beam current) are needed. Furthermore, there are many other factors affecting dispersoid morphology evolution. Void swelling, for example, may change dispersoid size and density. Small voids can act as nucleation sites of dispersoids. Since we did not observe void swelling in the Hf-doped ODS in the present study, such complexity was not considered.

Accelerator-based heavy ion irradiation in general has the complexity including, but not limited to, surface sputtering, surface defect sink effect, injected interstitials, and defect imbalance. Some effects have been recently reviewed by Zinkle and Snead [38]. Due to the fact that these effects are sensitive to detail radiation conditions, we here limit our discussions below to the condition close to the present study. For surface sputtering effect, recent studies by Jing et al. estimated a sputtered thickness of about 14 nm

by 100-peak-dpa 3.5 MeV Fe ion irradiation [39], based on sputtering yield calculated from SRIM simulations. The sputtering effect and its impact on damage profile shifting, therefore, are ignorable in the present study. As for surface defect sink effect, it is difficult to tell since the ODS alloy used in the present study is swelling resistant and we cannot observe void depletion zone. In pure Fe, 3.5 MeV Fe ion irradiation (450°C, 105 peak dpa) creates a 120 nm wide void depletion zone (based on the half width of the zone) [40]. Therefore, assuming defect migration is comparable in Fe and the ODS alloy, the shallowest characterization depth of 250 nm in the present study is away from the surface-affected zone. Under the combined effects from injected interstitials due to extra atoms implanted and defect imbalance due to spatial difference between interstitials and vacancies, void swelling is greatly suppressed at the Fe projected range. Under 100-peak-dpa 3.5 MeV Fe ion irradiation at 450°C, void swelling in pure Fe appears within the region from 120 nm to 825 nm. Therefore, our characterization depths of 250 nm and 650 nm are not affected by both the surface effect and the defect imbalance effect. We further believe the characterization depth of 1000 nm, correspond to the damage peak, is also valuable for the dose rate effect studies due to the following reason. Under defect imbalance effect, the excessive interstitials ($\Delta C = C_I - C_V$) are peaked at about 9×10^4/cm^3 per incident 3.5 MeV Fe ion [40]. This number is much lower than the damage peak (C_I, C_V) of 2.6×10^8/cm^3 [40]. Void swelling is sensitive to defect imbalance (ΔC). But the defect assisted diffusion (Eq. 6) is sensitive to defect densities (C_I, C_V), which are orders of magnitude higher than ΔC. Therefore, the defect imbalance effect (including injected interstitial) plays a weak role in influencing D.

In summary, the Hf-doped ferrite ODS alloy was irradiated using 3.5 MeV Fe^{2+} ion at 475 °C up to 100 peak dpa. The dispersoid coherencies, sizes and densities at different depths were characterized. Both coherent and incoherent dispersoid sizes shrunk in the ion range and the incoherent dispersoid sizes were larger than those of coherent dispersoids at all depths. The densities were increased in the ion range for both coherent and incoherent dispersoids and the coherent dispersoid densities were higher than those of incoherent dispersoids. Despite of the dpa rate differences at each depth, the dispersoid sizes do not show noticeable depth dependent changes in the experiment. To explain this, defect-assisted-diffusion mechanisms were introduced, showing dispersoid size has weak or no dependence on dpa rate. Although the dpa rate differences in this study were much smaller than that between the real reactor environment and the accelerator test, the present study shows the possibility of using ion irradiation to simulate neutron irradiation on studying dispersoid stability in ODS alloys.

References

[1] L.K. Mansur, A.F. Rowcliffe, R.K. Nanstad, S.J. Zinkle, W.R. Corwin, R.E. Stoller, Materials needs for fusion, Generation IV fission reactors and spallation neutron sources - similarities and differences, J. Nucl. Mater. 329-333 (2004) 166–172.
[2] G.R. Odette, M.J. Alinger, B.D. Wirth, Recent developments in irradiation-resistant steels, Annu. Rev. Mater. Res. 38 (2008) 471–503.
[3] J. Chen, P. Jung, T. Rebac, F. Duval, T. Sauvage, Y. de Carlan, M.F. Barthe, Helium effects on creep properties of Fe-14CrWTi ODS steel at 650 ºC, J. Nucl. Mater. 453 (2014) 253-258.
[4] J. Chen, P. Jung, W. Hoffelner, H. Ullmaier, Dislocation loops and bubbles in oxide dispersion strengthened ferritic steel after helium implantation under stress, Acta Mater. 56 (2008) 250-258.
[5] T. Chen, E. Aydogan, J.G. Gigax, D. Chen, J. Wang, X. Wang, S. Ukai, F.A. Garner, L. Shao, Microstructural changes and void swelling of a 12Cr ODS ferritic-martensitic alloy after high-dpa self-ion irradiation, J. Nucl. Mater. 467 (2015) 42–49.
[6] T. Chen, J.G. Gigax, L. Price, D. Chen, S. Ukai, E. Aydogan, S.A. Maloy, F.A. Garner, L. Shao, Temperature dependent dispersoid stability in ion-irradiated ferritic-martensitic dual-phase oxide-

dispersion-strengthened alloy: Coherent interfaces vs. incoherent interfaces, Acta Mater. 116 (2016) 29-42.
[7] G.R. Odette, Recent progress in developing and qualifying nanostructured ferritic alloys for advanced fission and fusion applications, JOM 66 (2014) 2427-2441.
[8] C.H. Zhang, Y.T. Yang, Y. Song, J. Chen, L.Q. Zhang, J. Jang, A. Kimura, Irradiation response of ODS ferritic steels to high-energy Ne ions at HIRFL, J. Nucl. Mater. 455 (2014) 61-67.
[9] E. Aydogan, N. Almirall, G.R. Odette, S.A. Maloy, O. Anderoglu, L. Shao, J.G. Gigax, L. Price, D. Chen, T. Chen, F.A. Garner, Y. Wu, P. Wells, J.J. Lewandowski, D.T. Hoelzer, Stability of nanosized oxides in ferrite under extremely high dose self-ion irradiations, J. Nucl. Mater. 486 (2017) 86-95.
[10] J.P. Wharry, M.J. Swenson, K.H. Yano, A review of the irradiation evolution of dispersed oxide nanoparticles in the b.c.c. Fe-Cr system: Current understanding and future directions, J. Nucl. Mater. 486 (2017) 11-20.
[11] M.J. Swenson, J.P. Wharry, Nanocluster irradiation evolution in Fe-9%Cr ODS and ferritic-martensitic alloys, JNM, 496 (2017) 24-40.
[12] X. Liu, Y. Miao, Y. Wu, S.A. Maloy, J.F. Stubbins, Stability of nanoclusters in an oxide dispersion strengthened alloy under neutron irradiation, Scripta Mater. 138 (2017) 57-61.
[13] C.M. Parish, R.M. White, J.M. LeBeau, M. K. Miller, Response of nanostructured ferritic alloys to high-dose heavy ion irradiation, JNM 445 (2014) 251-260.
[14] C. Lu, Z. Lu, X. Wang, R. Xie, Z. Li, M. Higgins, C. Liu, F. Gao, L. Wang, Enhanced radiation-tolerant oxide dispersion strengthened steel and its microstructure evolution under helium-implantation and heavy-ion irradiation, Scientific Reports 7: 40343 (2017).
[15] M.L. Lescoat, J. Ribis, Y. Chen, E.A. Marquis, E. Bordas, P. Trocellier, Y. Serruys, A. Gentils, O. Kaïtasov, Y. de Carlan, A. Legris, Radiation-induced Ostwald ripening in oxide dispersion strengthened ferritic steels irradiated at high ion dose, Acta Mater. 78 (2014) 328-340.
[16] H. Kishimoto, R. Kasada, O. Hashitomi, A. Kimura, Stability of Y-Ti complex oxides in Fe-16Cr-0.1Ti ODS ferritic steel before and after heavy-ion irradiation, J. Nucl. Mater. 386e388 (2009) 533-536.
[17] R.S. Nelson, J.A. Hudson, D.J. Mazey, The stability of precipitates in an irradiation environment, J. Nucl. Mater. 44 (1972) 318–330.
[18] C. Wagner, Theory of the ageing of precipitates by redissolution (Ostwald maturing), Z. Elektrochem 65 (1961) 581–591.
[19] K. Vortler, M. Mamivand, L. Barnard, I. Szlufarska, F.A. Garner, D. Morgan, Simulated spatial and temporal dependence of chromium concentration in pure Fe and Fe-14%Cr under high dpa ion irradiation, J. Nucl. Mater. 479 (2016) 23-35.
[20] V.A. Pechenkin, A.D. Chernova, F.A. Garner, Modeling of local changes in composition of alloys along the projected range under heavy ion irradiation, in: AccApp 2013, Belgium, 2013, p. 12.
[21] T. Okuda, M. Fujiwara, T. Nakai, K. Shibata, A. Kimura, M. Inoue, S. Ukai, S. Ohnuki, T. Fujisawa, F. Abe, Super ODS steels R&D for fuel cladding of next generation nuclear systems, 3; Development of high performance attrition type ball mill, Proc. Int. Conf. on Advanced Power Plant, Tokyo, Japan, May 10-14 (2009) Paper 9229.
[22] T. Furukawa, S. Ohtsuka, M. Inoue, T. Okuda, F. Abe, S. Ohnuki, T. Fujisawa and A. Kimura: Proc. Int. Conf. on Advanced Power Plant, Tokyo, Japan, May 10–14 (2009) Paper 9221.
[23] F.A. Garner, M.B. Toloczko, B.H. Sencer, Comparison of swelling and irradiation creep behavior of fcc-austenitic and bcc-ferritic/martensitic alloys at high neutron exposure, J. Nucl. Mater. 276 (2000) 123-142.
[24] F.A. Smidt Jr., P.R. Malmberg, J.A. Sprague, J.E. Westmoreland, Swelling behavior of commercial ferritic alloys, EM-12 and HT-9, as assessed by heavy ion bombardment, vol. STP 611, ASTM International, Philadelphia, PA, 1976, pp. 227-241.
[25] J.G. Gigax, H. Kim, T. Chen, F.A. Garner, L. Shao, Radiation instability of equal channel angular extruded T91 at ultra-high damage levels, Acta Mater. 132 (2017) 395-404.

[26] J.G. Gigax, T. Chen, Hyosim Kim, J. Wang, L.M. Price, E. Aydogan, S.A. Maloy, D.K. Schreiber, M.B. Toloczko, F.A. Garner, L. Shao, Radiation response of alloy T91 at damage levels up to 1000 peak dpa, J. Nucl. Mater. 482 (2016) 257-265.
[27] J.G. Gigax, E. Aydogan, T. Chen, D. Chen, Y. Wu, W.Y. Lo, Y. Yang, F.A. Garner, The influence of beam rastering on the swelling of self-ion irradiated pure iron at 450°C, J. Nucl. Mater. 465 (2015) 343-348.
[28] J.G. Gigax, H. Kim, E. Aydogan, F.A. Garner, S. Maloy, L. Shao, Beam-contamination-induced compositional alteration and its neutron-atypical consequences in ion simulation of neutron-induced void swelling, Mater. Res. Lett., in press.
[29] L. Shao, J.G. Gigax, D. Chen, H. Kim, F.A. Garner, J. Wang, M.B. Toloczko, Standardization of accelerator irradiation procedures for simulation of neutron induced damage in reactor structural materials, Nucl. Instr. Meth. Phys. Res. B, in press.
[30] J.F. Ziegler, M.D. Ziegler, J.P. Biersack, SRIM – the stopping and range of ions in matter, Nucl. Instr. Meth. Phys. Res. B 268 (2010).
[31] R.E. Stoller, M.B. Toloczko, G.S. Was, A.G. Certain, S. Dwaraknath, F.A. Garner, On the use of SRIM for computing radiation damage exposure, Nucl. Instr. Meth. Phys. Res. B 310 (2013) 75-80.
[32] G.S. Was, Fundamentals of Radiation Materials Science: Metals and Alloys, Springer, 2007 p.218.
[33] M. Nastasi, J. Mayer, J.K. Hirvonen, Ion-solid interactions: fundamentals and applications, Cambridge University Press, New York, 1996.
[34] J. Ribis, Y. de Carlan, Interfacial strained structure and orientation relation- ships of the nanosized oxide particles deduced from elasticity-driven morphology in oxide dispersion strengthened materials, Acta Mater. 60 (2012) 238–252.
[35] J.M. Howe, Interfaces in materials, Wiley-Interscience, 1997.
[36] H. Okamoto, Journal of Phase Equilibria 16 (1995) 473–473.
[37] C. Lu, Z. Lu, R. Xie, Z. Li, C. Liu, L. Wang, Effect of Y/Ti atomic ratio on microstructure of oxide dispersion strengthened alloys, Materials Characterization 134 (2017) 35-40.
[38] S.J. Zinkle and L.L. Snead, Opportunities and limitations for ion beams in radiation effects studies: Bridging critical gaps between charged particle and neutron irradiations, Scripta Materialia 143 (2018) 154-160.
[39] J. Wang, M.B. Toloczko, N. Bailey, F.A. Garner, J. Gigax, L. Shao, Modification of SRIM-calculated dose and injected ion profiles due to sputtering, injected ion buildup and void swelling, Nucl. Instrum. Methods in Phys. Res. B 387 (2016) 20-28.
[40] L. Shao, C.C. Wei, J. Gigax, A. Aitkaliyeva, D. Chen, B.H. Sencer, F.A. Garner, Effect of defect imbalance on void swelling distributions produced in pure iron irradiated with 3.5 MeV self-ions, J. Nucl. Mat. 453 (2014) 176-181.

Research highlight #7

Molecular dynamics simulations of oxide particles in Fe

Molecular dynamic simulations (MD) of Y2O3 in bcc Fe, along with transmission electron microscopy (TEM) observations, were used to understand the structure of Y2O3 nano-clusters. The study showed that Y2O3 nano-clusters of size below 2 nm were completely disordered. Y2O3 nanoclusters above 2 nm, however, form with a core-shell structure, with a shell thickness of 0.5-0.7 nm that is independent of nanocluster sizes. The Y2O3 nano-clusters were surrounded by off-lattice Fe atoms, further increasing the stability of these nano-clusters. TEM was used to corroborate our simulation results and showed a crossover from a disordered nano-cluster to a shell-core structure.

F7-1 Results and discussions

To simulate the stability and configuration of the Y_2O_3 nano-particles, an Y_2O_3 cluster was placed at the center of a Fe matrix. For small Y_2O_3 NCs (1-5 nm in diameter) a MD block with $40 \times 40 \times 40$ unit cells (containing 128,000 atoms) was used, but for the larger clusters (greater than 5 nm) a block with $64 \times 64 \times 64$ unit cells (containing 525,000 atoms) was used. The systems were relaxed using the conjugant gradient method and then raised temperature to 600 K for 15 ps with the NVT (constant atoms, volume and temperature) canonical ensemble, in order to identify the minimum energy configuration of the Y_2O_3 NCs. The interactions between atoms are described using the Buckingham potential [1], but are connected to the repulsive potential of Ziegler, Biersack, and Littmark (ZBL) for short range interactions. The lattice constant, determined for α-Fe, is 0.2855 nm, is in good agreement with DFT calculations [1]. Further details on the interatomic potential can be found in reference [1]. For this study, we have modified the interatomic potential to include the charges for the Y and O atoms. By adding the charges, the Y_2O_3 particles tend to be more stable because the charge hinders the movement of the O atoms. The simulation was carried out using the LAMMPS code [2]. Periodic boundary conditions are applied in all three directions, and a time step of 5 fs was used. Ovito software was used to visualize the data and determine the structure [3], and VMD was used to determine atom counts [4].

Y_2O_3 has a cubic structure with space group Ia-3 [5]. The Y atoms occupy the 8(b) sites and 24(d) sites and the O atoms are located on the 48(e) general sites. Experimental Y_2O_3 has a lattice constant of 1.06 nm [5]. In testing the Y_2O_3 structure, our model underestimated the lattice parameter and the most stable structure occurred with a lattice constant of 0.95 nm. Due to the complexity of O atoms, it is impossible to model O-O relation perfectly using a pairwise function; however, the overall trends for the system are not affected greatly because of the overall small percent of O in the system [1]. The stability of Y_2O_3 was tested in a box of size 10 x 10 x 10 unit cells, with a total of 80,000 atoms by relaxing the system, raising the temperature to 600 K for 15 ps, and then quenching to 0 K with the NVT canonical ensemble. Common neighbor analysis and coordination approach were applied to determine the Y_2O_3 structure. The common neighbor analysis on the Y atoms suggested a fcc structure of Y_2O_3 and the radial distribution function for pure Y_2O_3 is used to compare to the Y_2O_3 in the Fe system.

A 12 nm diameter was used as the cut off in the present study because that is the point where Klimiankou showed that Y_2O_3 particles would move from a spherical shape to a faceted one [6]. In order to keep charge neutrality of the system, several Y or O atoms near the Fe-cluster interface are removed from the system, which is dependent of its size. For the NCs, the system was first relaxed using the

conjugate gradient algorithm, followed by a structure annealing at 600 K and then quenched back to 0 K. For the larger cluster sizes the system was just relaxed, based on no significant changes in the smaller cluster systems during structure annealing and quenching back to 0 K.

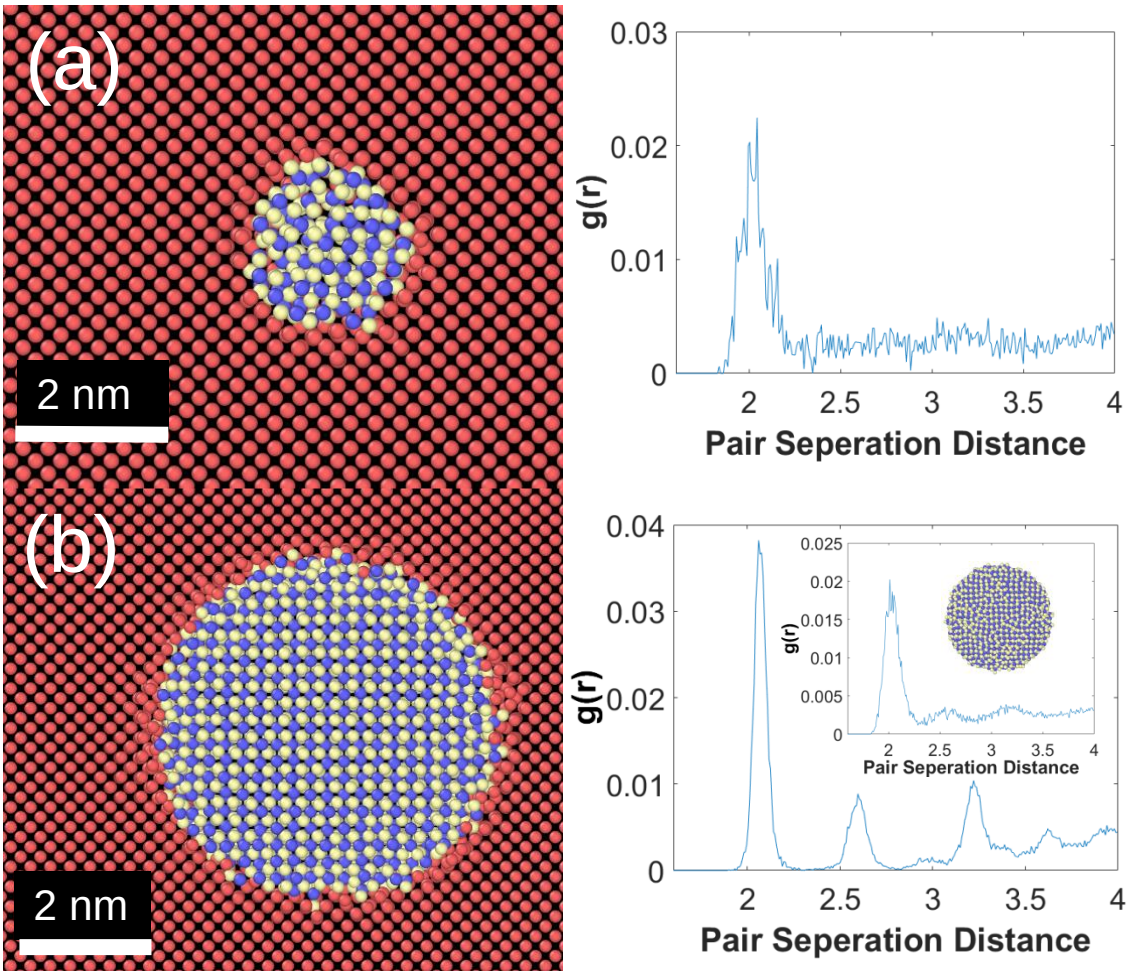

Figure 1. (a) Cross section of Fe embedded with a 2 nm oxide particle and (b) cross section of Fe embedded with a 5 nm oxide c particles. The corresponding radial distribution functions of the oxide core are given.

A TEM observation has been conducted on a 9Cr-ODS alloy with a nominal composition of Fe–9Cr–1.5W–0.4Mn–0.1Ta–0.2V–0.3Y_2O_3 (mass %). 9Cr-ODS alloy was prepared by MA in a planetary high-energy ball mill at room temperature for 50 h in an argon-gas atmosphere. The ball-to-powder weight ratio was 10:1. Followed by hot isostatic pressing, the samples ran at 1373 K under a pressure of 200 MPa for 2 h. TEM samples were prepared by focused ion beam (FIB) lift-out method on the mechanical polished raw 9Cr-ODS alloy, using FEI Helios Nanolab Dualbeam workstation. Scanning TEM (STEM) was employed to characterize the structure of nano-clusters of Y_2O_3 using a double Cs-Corrected STEM (JEOL 3100R05) operated at 300 keV.

Common neighbor analysis determined the structure of the Y_2O_3 NCs. The crystal structure consists of a spherical Y_2O_3 structured region surrounded by a disordered region in which the atoms cannot be identified to form a particular crystal structure. For the clusters below 2 nm, the entire NCs were disordered. For the Y_2O_3 clusters between the sizes of 2 nm and 12 nm, the relaxed atomic configurations of Y_2O_3 NCs consist of a structured core of cubic Y_2O_3 surrounded by a disordered region. Both the disordered and structured regions have near stoichiometric Y_2O_3, but the disordered region separates the structured core from the Fe matrix, thus forming a core-shell structure. Figure 1(a) shows a cross section of a 2 nm cluster in Fe matrix, along with the radial distribution of the NC. Both the atomic configuration and the radial distribution indicate that the entire NC is disordered without a crystalline structure. The radial distribution consists of only a single major peak, and shows the typical systems without periodicity and liquid-like structure. Figure 1(b) shows an image of a 5 nm cluster (the cross section, and the radial distribution of the structured region, where the inset in the right corner shows the atomic arrangement of the Y_2O_3 shell and its corresponding radial distribution). The center of the NC has a cubic Y_2O_3 structure, and the radial distribution peaks occur at the same places compared to the pure Y_2O_3 system. Within the shell, the radial distribution is similar to that shown in figure 1(a) with a single major peak, and the atoms in the shell also appear to be disordered.

In figure 2, the disorder fraction of atoms, which is defined as a ratio of number of atoms in the disordered region to that of the structured core, is plotted versus the diameter of the Y_2O_3 NCs. The NCs smaller than 2 nm are completely disordered. The thickness of the disordered region imposed in figure 2 does not change significantly with increasing the size of NCs, and remains almost constant (roughly 0.5-0.7 nm). High-resolution high angle annual dark field (HAADF) characterization has been conducted to understand the atomic structures of the nano-clusters, particular for clusters smaller than 5 nm in 9Cr-ODS. The contrast of HAADF imaging is sensitive to the atomic number and mass density [7]. Thus NCs generally show darker contrast compared to the surrounding ferritic matrix because of the enrichment of the O elements. Figure 3 shows a typical Y_2O_3 nano-cluster with a diameter of 2 nm. High resolution HAADF image was taken with the electron incidence parallel to the bcc $[111]_{matrix}$ direction.

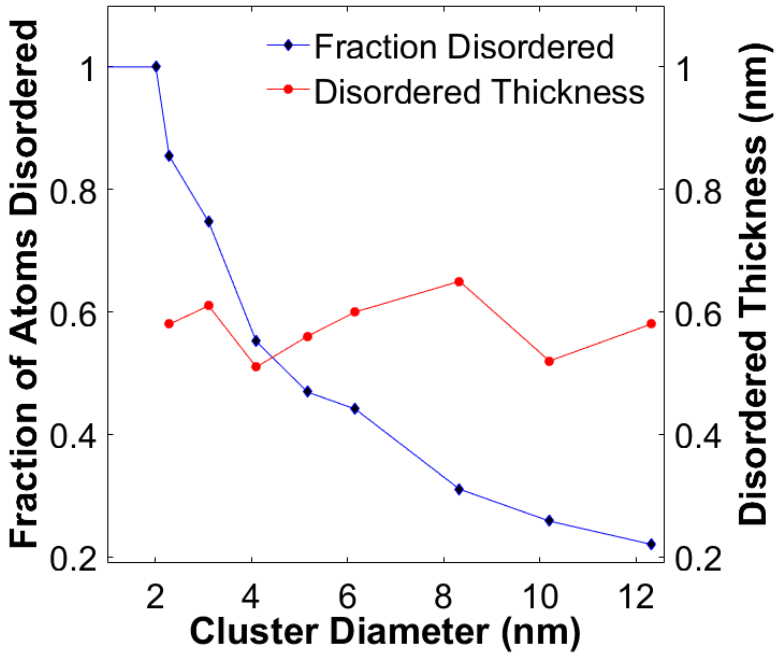

Figure 2. The disordered fraction of Y and O atoms in the shell regions as compared to those in the core regions along the left y-axis and the thickness of the disordered region along the right y-axis.

From figure 3, it is clear that no distinct lattice structure has been observed in this nano-cluster, indicating that atomic species are randomly distributed within the cluster without forming a typical crystal structure, particularly at the core of the cluster. In an ODS alloy without Ti, the oxides generally tend to form larger Y_2O_3 clusters, as compared with Y-Ti-O ODS. However, this study demonstrates that very small Y_2O_3 NCs can be formed in the 9Cr-ODS alloy without observed titanium in the matrix. The Y_2O_3 NC in figure 3 displays faceted interfaces along low-index planes of the matrix. Similar faceting has been reported by Brandes in a Y-Ti-O ODS steel [7]. Brandes also found small nano-sized Y-Ti-O clusters which were amorphous as revealed from high-resolution TEM images [7]. Based on these observations, it is believed that the small Y-O cluster in the present study probably appears to be amorphous, which is consistent with our simulation results. Figure 2 also shows that the disorder fraction decreases with increasing size of Y_2O_3 NCs. Since the thickness of the disordered region remains roughly the same, the number of ordered atoms increases with increasing size of Y_2O_3 NCs, causing a decrease in the disordered fraction. Figure 2 clearly shows that the core, the structured region, rapidly increases with increasing size when the diameter is larger than 2 nm. There exists a crossover from completely disordered NCs to a core-shell structure.

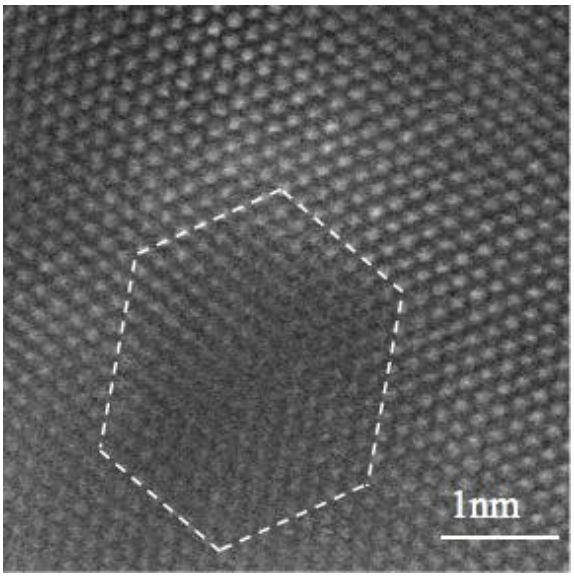

Figure 3. High resolution HAADF image of a 2 nm Y2O3 cluster.

All of the particles, with a structured core, are surrounded by a disordered shell with a thickness between 0.5-0.7 nm, whereas the experiments have shown a shell thickness between 1-1.5 nm. The difference in thickness may stem from the fact that our current model does not include Cr and V, major elements, commonly found in the shell [8]. Without these elements in our model, there are less interactions for the O atoms and instead can only interact with the Y and Fe atoms. Although the shell of NCs is thinner compared to the experimental data, our data shows that the strain introduced on the NCs due to the mismatch between the Fe matrix and the NCs may lead to the formation of the shell, which is an energy preferred structure. At the boundary between the Y_2O_3 particle and the Fe matrix, the Fe atoms are slightly disturbed and off their lattice locations. These off-lattice atoms may increase the irradiation strength of these particles, by attracting the number of interstitial atoms, thus creating a protective sink. This phenomena is similar to grain boundaries and dislocations that act as a sink for defects [9], though the operating mechanisms are slightly different. A TEM image of a 20 nm Y_2O_3 characterized by HAADF in Fig. 4(a) shows nano-sized oxides distributed in ODS matrix. High-resolution HAADF image in Fig.

4(b) clearly reveals a disordered shell between matrix and large yttria particles, as demonstrated by FFT images in Fig. 4(c) for Y_2O_3, (d) for the disordered layer and (e) for the ferritic matrix. TEM observation is qualitatively consistent with our MD simulation, i.e. the Y_2O_3 NCs consist of a structured core of cubic Y_2O_3 surrounded by a disordered region, which cannot be identified as a particular crystalline structure.

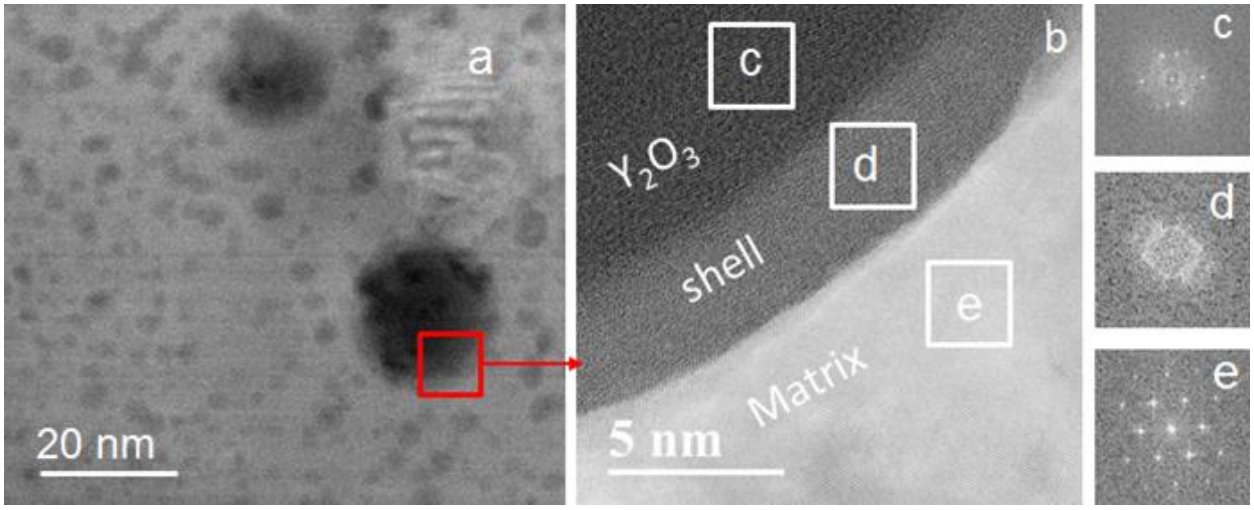

Figure 4. (a) HAADF image shows nano-sized oxides distributed in ODS matrix. (b) High-resolution HAADF image shows a disordered shell between matrix and a large yttria particle (c) FFT image from yttrium. (d) FFT image from disordered layer. (e) FFT image from ferritic matrix.

In a summary, we combine computer simulations and experiments to study the structure of Y_2O_3 precipitates in α Fe. The results show that Y_2O_3 NCs are disordered when their size is below 2 nm, while the larger clusters form a core-shell structure, with a thickness of 0.5-0.7 nm that is independent of their size. It is of interest to find that there exists a crossover from the completely disordered NCs to core-shell structures. It is expected that a slight disturbances in the Fe atoms surrounding the Y_2O_3 particles may further increase the irradiation strength of these particles, thus increasing irradiation resistance. TEM images also demonstrate the crossover from disordered NCs to core-shell structures, and the results are qualitatively consistent with the MD simulations. Although the thickness of the disordered shell is smaller compared to the experimental data available, these results provide the atomistic-level understanding of Y_2O_3 NCs structures in α Fe.

References

[1] K.D. Hammond, H.-J. Lee Voigt, L.A. Marus, N. Juslin, B.D. Wirth, J. Phys. Condens. Matter 25 (2013) 55402–13.
[2] S. Plimpton, J. Comput. Phys. 117 (1995) 1–19.
[3] A. Stukowski, Modell. Simul. Mater. Sci. Eng. 18 (2010) 015012.
[4] W. Humphrey, A. Dalke, K. Schulten, J. Mol. Graphics 14 (1996) 33–38.
[5] F. Hanic, M. Hartmanová, G.G. Knab, A.A. Urusovskaya, K.S. Bagdasarov, Acta Crystallogr. Sect. B Struct. Sci. (1984).

[6] M. Klimiankou, R. Lindau, A. Möslang, J. Nucl. Mater. 249 (2003) 381–387.
[7] M.C. Brandes, L. Kovarik, M.K. Miller, M.J. Mills, J. Mater. Sci. 47 (2012) 3913–3923.
[8] M. Klimenkov, R. Lindau, A. Möslang, J. Nucl. Mater. 386-388 (2009) 553–556.
[9] M.A. Tschopp, M.F. Horstemeyer, F. Gao, X. Sun, M. Khaleel, Scr. Mater. 64 (2011) 908–911.

Research highlight #8

Irradiation of rare earth oxide particle strengthened alloys

Using an alternate rare earth (RE) oxide in ODS alloys can significantly reduce costs. In this new approach, an alloy with a nominal composition of Fe–14Cr–1Ti–0.3Mo–0.5La2O3 (wt.%) was developed and was termed as 14LMT. In addition to altering the RE constituent in the chemical composition, the traditional consolidation methods such as HIP and extrusion were replaced by spark plasma sintering (SPS). The sintered samples were irradiated by Fe^{2+} ions to 10, 50 and 100 dpa at 30 °C and 500 °C. Microstructural characteristics of the irradiated samples were studied using different microscopy techniques. Overall morphology and number density of the nanofeatures remained unchanged after irradiation. Average radius of nanofeatures in the irradiated sample (100 dpa at 500 °C) was slightly reduced. The study shows the promise to use yttrium-replaced ODS alloys for future alloy development.

F8-1 Introduction

Improvements in efficiency, safety and sustainability of the advanced nuclear reactors require fuel cladding materials and structural components that possess superior mechanical properties and microstructural stability under extreme conditions including high radiation damage (about 200 displacement per atom or dpa) and high temperatures (about 700 °C) [1–4]. Nanostructured ferritic steels (NFSs), which is a unique sub-class of oxide dispersion strengthened (ODS) steels, are considered potential candidate materials for fuel cladding applications in Gen-IV fission reactors due to their high radiation resistance and high creep strength at elevated temperatures [5,6]. NFSs such as MA957 (Fe–14Cr–1Ti– 0.25Mo–0.25Y2O3) and 14YWT (Fe–14Cr–0.4Ti–3W–0.25Y2O3) are typically produced by mechanical alloying (MA) of pre-alloyed or elemental powder mixture and subsequent powder consolidation via hot extrusion or hot isostatic pressing (HIP) [3,7]. Microstructure of a NFS contains a high number density of thermally stable dispersion strengthening nanofeatures (also known as nanoclusters or NCs) enriched in Y–Ti–O or Y–Al–O that are resistant to radiation damage up to 800 °C [8]. These nanofeatures, approximately 2–5 nm in diameter, provide high tensile and creep strength at elevated temperatures and appear to trap helium in fine bubbles limiting void swelling [3,9,10]. Stability of oxide particles under irradiation is critical.

It is known that collision cascades can eject solute atoms from oxide particles and change their physical characteristics. Irradiation experiments are required in order to understand the stability of particles. Since neutron irradiation experiment was outside the scope of the present study, the developed ODS alloys was exposed to self-ion (Fe^{2+}) irradiation. Subsequently, the irradiated material was characterized by transmission electron microscopy, atom probe tomography and nanoindentation.

F8-2 Experimental details

All powders were procured from American Elements Inc., except the Mo powder that was procured from Micron Metal Powder Inc. The starting constituent powders including Fe (99.9 wt.%, average powder size of 40 μm), Cr (99.8 wt.%, average powder size of 5 μm), Ti (99.7 wt.%, average powder size of 26 μm), La2O3 (99.99 wt.%, average powder size of 40 nm) and Mo (99.9 wt.%, average powder size of 1–2 μm) were mixed in the nominal proportion of Fe–14Cr–1Ti–0.3Mo–0.5La2O3 (wt.%). High-energy ball milling was performed in an air-cooled Spex 8000 M mixer/mill for 10 h using 316 stainless

steel balls (8 mm in diameter) as the milling media. High energy ball milling was performed at a speed of 1725 r.p.m. with lateral movement. The vial was vibrated at an amplitude of 50 mm and frequency of 20 Hz during milling. A milling batch consisted of 100 g steel balls and 10 g powder giving a ball to powder ratio (BPR) of 10:1. The milled powder was consolidated via SPS. A TriGemini cylindrical graphite die with an inner diameter of 12.7 mm and an outer diameter of 38 mm was used. The inner surfaces of the dies and radial surfaces of punches were covered with a graphite foil (0.25 mm in thickness) to facilitate removal of the sintered specimens. In order to inhibit the diffusion of carbon from the punches and graphite foil to the powder mixture, a thin niobium foil (thickness of 0.06 mm) was placed between the powder and the graphite foils. The dies were wrapped in a graphite felt with 4 mm thickness to minimize heat loss by thermal radiation. The milled powder was sintered at 950 °C for 45 min under vacuum. A pulsed DC current with pattern of 12–2 (current on for 12 ms and off for 2 ms), a heating rate of 100 C/min and a pressure of approximately 80 MPa (10 kN force) were used. The final product was in the form of a disk with diameter of 12.5 mm and thickness of 8 mm.

Prior to irradiation, specimens with diameter of about 12 mm and thickness of 1 mm were mechanically thinned using standard metallographic procedures of grinding and polishing followed by a final polish in a vibratory polisher using 0.05 μm alumina slurry for up to 48 h. The specimens were irradiated with iron ions (Fe^{2+}) at the Texas A&M Ion Beam Laboratories using 1.7 MV Tandetron accelerator. The specimens were irradiated to 10, 50 and 100 dpa, at temperatures of 30 °C and 500 °C, respectively. Samples were mounted on a heating stage using silver paint. Sample temperatures were adjusted by changing the current of a resistance heater, through a feedback system linked to thermocouples attached on sample surfaces. The beam uniformity and heating were monitored by using an infrared camera. Due to complexity from thermal electron emission, the beam intensity was monitored by a Faraday cup positioned before the heat stage. Considering that thermal annealing at 500 °C only may lead to structural evolutions, one control sample was added to the heat stage without exposure to the ion beam. The dpa peak is about 0.9 μm below the surface. The microstructural analysis was focused on the region at the depth of about 400 nm to 800 nm. The selection of this region considers the necessity to avoid the surface defect-depleted region due to defect sink property of a free surface and the region affected by defect imbalance [11].

F8-3 Results and discussions

The TEM bright field (BF) micrograph in Fig. 1(a) exhibits a representative view of the irradiation damage layer, protective Pt layer and the analyzed region in 14LMT alloy. The TEM BF micrographs in Fig. 1(b–g) show representative microstructures of 14LMT alloy unirradiated and irradiated. The microstructure in Fig. 1(b–g) consisted primarily of nanograins with a high density of grain boundaries, dislocations and precipitates. The grain structure including grain size remained unchanged after irradiation at 30 and 500 C up to 100 dpa, and no recrystallization or grain growth were observed after irradiation at higher temperature. The analysis of selected area diffraction (SAD) patterns showed neither the formation of any radiation-induced particles or new phases nor was there evidence of an amorphous phase or the formation of voids.

The dislocation structures in the unirradiated condition, irradiated conditions at 30 C for 100 dpa, unirradiated at 500 °C and irradiated at 500 °C for 10, 50 and 100 dpa are all shown in Fig. 2(a–f), respectively. The micrographs were obtained under two-beam conditions close to a major zone axis. A high density of dislocations and nano-sized dark dots were identified. There was no evidence of

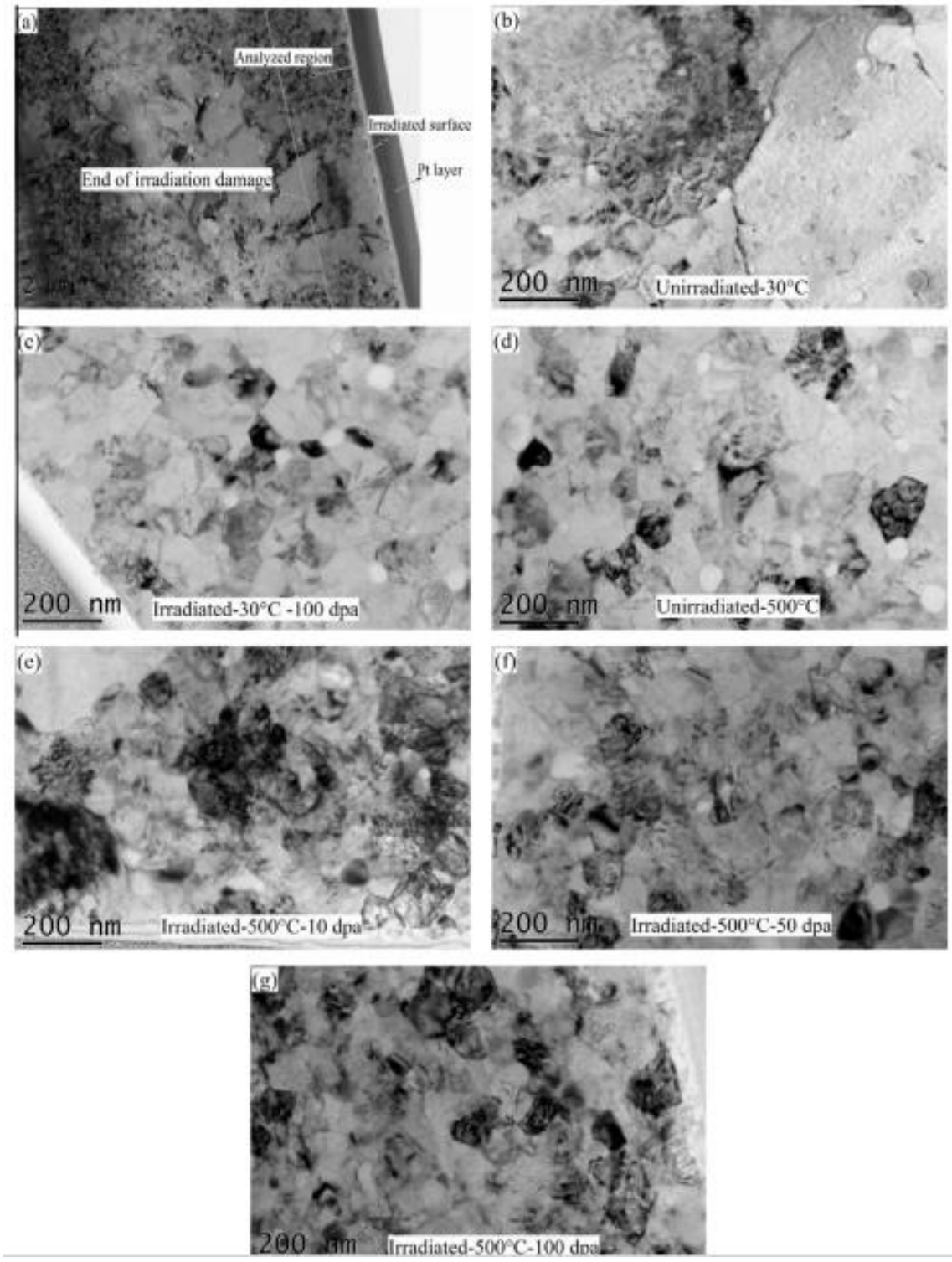

Fig. 1 TEM micrographs of 14LMT alloy: (a) the irradiation damage and analyzed region, (b) unirradiated, (c) irradiated at 30 C for 100 dpa, (d) unirradiated at 500 C, (e) irradiated at 500 C for 10 dpa, (f) irradiated at 500 C for 50 dpa and (g) irradiated at 500 C for 100 dpa.

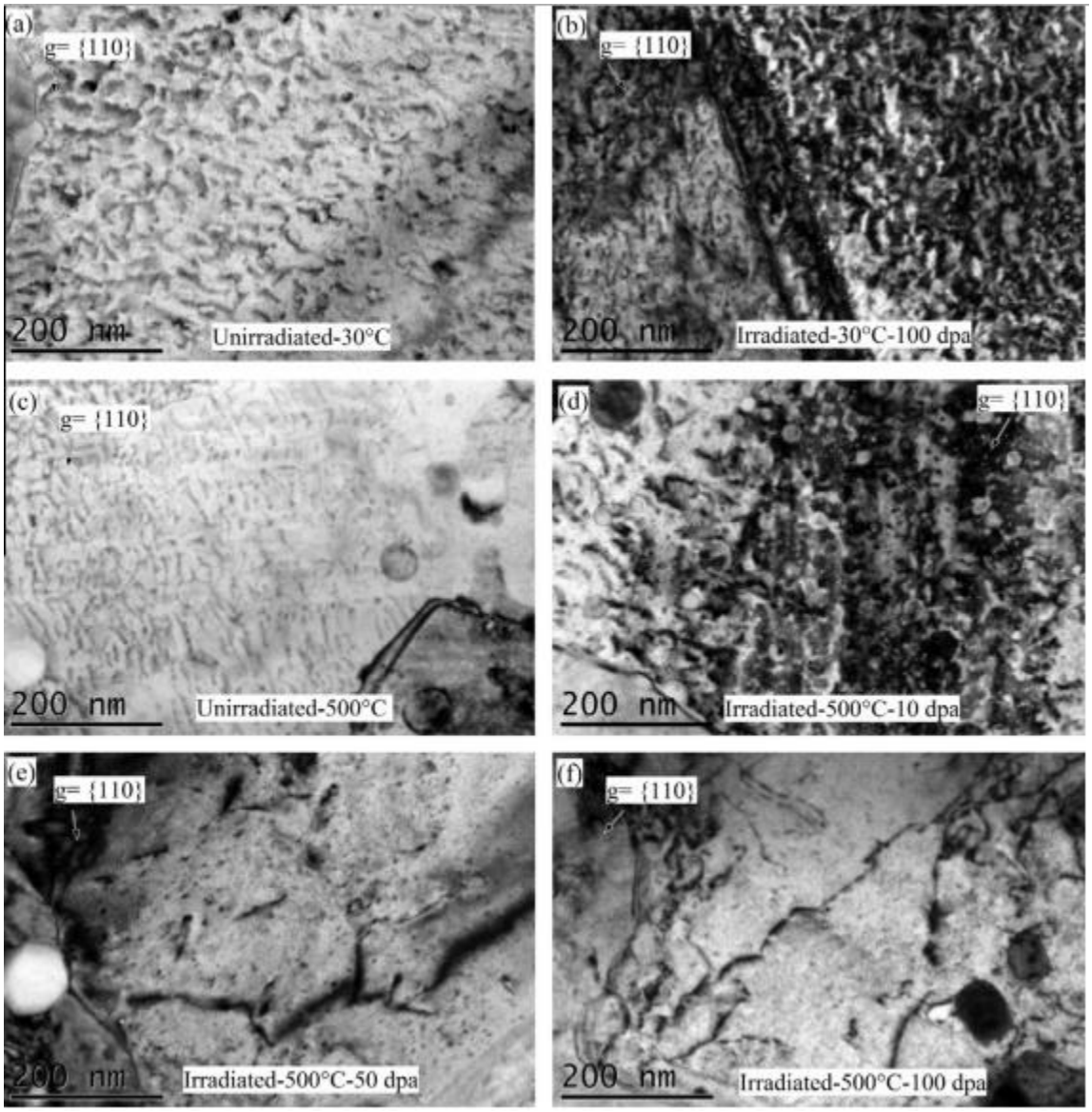

Fig. 2. TEM images of dislocations in 14LMT alloy: (a) unirradiated, (b) irradiated at 30 C for 100 dpa, (c) unirradiated at 500 C, (d) irradiated at 500 C for 10 dpa, (e) irradiated at 500 C for 50 dpa and (f) irradiated at 500 C for 100 dpa.

dislocation loops or tangled networks. All the micrographs were obtained at similar beam conditions (g = {011}). The ‘‘dark dots’’ in the unirradiated sample shown in Fig. 2(a), could be due to FIB artifacts. The dislocation density increased with higher ion doses regardless of irradiation temperature. The changes in dislocation density under irradiation are attributed to the high surface stresses caused by the high dose of implanted surfaces during the ion irradiation process. In unirradiated samples, a slight reduction in dislocation density was observed at 500 °C due to thermal dislocation annihilation, but the recovery was not extensive since the dislocations were pinned by nanoparticles as will be shown later. Dislocations that are effectively pinned by nanoparticles along with a high density of grain boundaries could provide strong sink sites for radiation induced point defects such as vacancies and interstitials [4,14].

The oxide particles of 14LMT alloy before and after irradiation are shown in Fig. 3(a–f). No strong contrast was observed between the nanoparticles and the matrix in the BF mode. However, the particle size did not undergo any significant irradiation coarsening or refining. In summary, the matrix/particles interface, shape, morphology and size of the particles did not show significant changes under Fe ion irradiation to 100 dpa. Particle size distribution histograms of the unirradiated and irradiated samples are shown in Fig. 4(a–f). In order to provide ample statistical data, at least 300 particles were used to generate the histograms. No significant particle size reduction was observed as indicated in Fig. 4(a–f). However, the fraction of particles smaller than 2 nm at higher doses appeared to be more obvious after irradiation at 500 °C than at 30 °C. Higher magnification micrographs were utilized for constructing the plots shown in Fig. 4(a–f), and mainly focused on the smallest particles. Particles larger than 36 nm were not included in the plots even though they were observed in some of the micrographs obtained at lower magnification. Furthermore, due to the resolution limit of the TEM and FIB sample preparation, particles smaller than 1 nm were not easily detected.

Fig. 5(a) shows a high angle annular dark field (HAADF) STEM micrograph obtained at a relatively low magnification. Both the irradiated region (from surface to 1.6 lm depth) and the analyzed region are marked. The nanoparticles distributed in the irradiated samples were clearly observed in the Z-contrast micrographs shown in Fig. 5(b–d). No significant change in morphology or chemical composition of the particles was noted in the Z-contrast micrographs. Fig. 5(e) shows an energy dispersive spectroscopy (EDS) spectrum of a 10 nm particle from the samples irradiated at 500 °C with 100 dpa dose whereas Fig. 5(f) shows an EDS spectrum obtained from the matrix of the same sample showing strong peaks of Fe and Cr. The particle was composed of Fe, Cr, La and O. Because the oxide particles were located in a foil thicker than the particle size, the EDS data included matrix information. The larger particles were primarily Cr–Ti-oxide or La–Cr-oxide and did not show any irradiation induced alteration in the chemical composition. The 14LMT unirradiated sample (500 °C) and 14LMT sample irradiated at 500 °C for 100 dpa were analyzed by the energy filtered TEM (EFTEM) method. The EFTEM micrographs in Fig. 6(a–h) show particles that were enriched in Ti and O but depleted of Fe. The particles smaller than 10 nm were enriched in La, but it was difficult to resolve in EFTEM due to sample thickness. The nanoparticles in both unirradiated and irradiated specimens appeared to remain chemically stable. The main contribution of nanoparticles is to enhance mechanical strength at high temperature by stabilizing subgrains and dislocation configurations. Secondly, these particles can inhibit and suppress void swelling along with the ferritic structure. Furthermore, the rastering mode of irradiation utilized in this study is not expected to produce detectable void swelling.

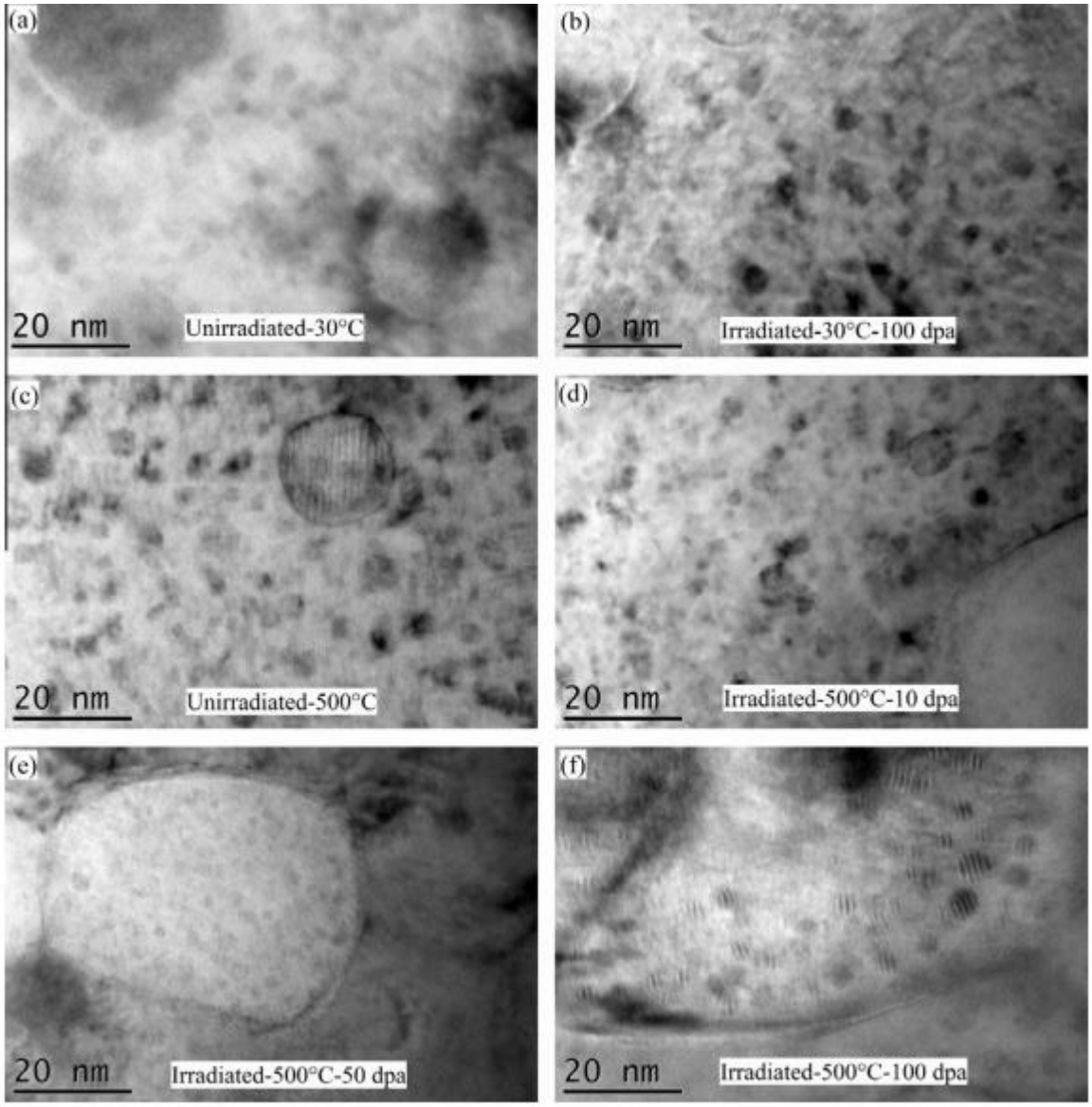

Fig.3. TEM images of the oxide particles observed in 14LMT alloy: (a) unirradiated, (b) irradiated at 30 C for 100 dpa, (c) unirradiated at 500 C, (d) irradiated at 500 C for 10 dpa, (e) irradiated at 500 C for 50 dpa and (f) irradiated at 500 C for 100 dpa.

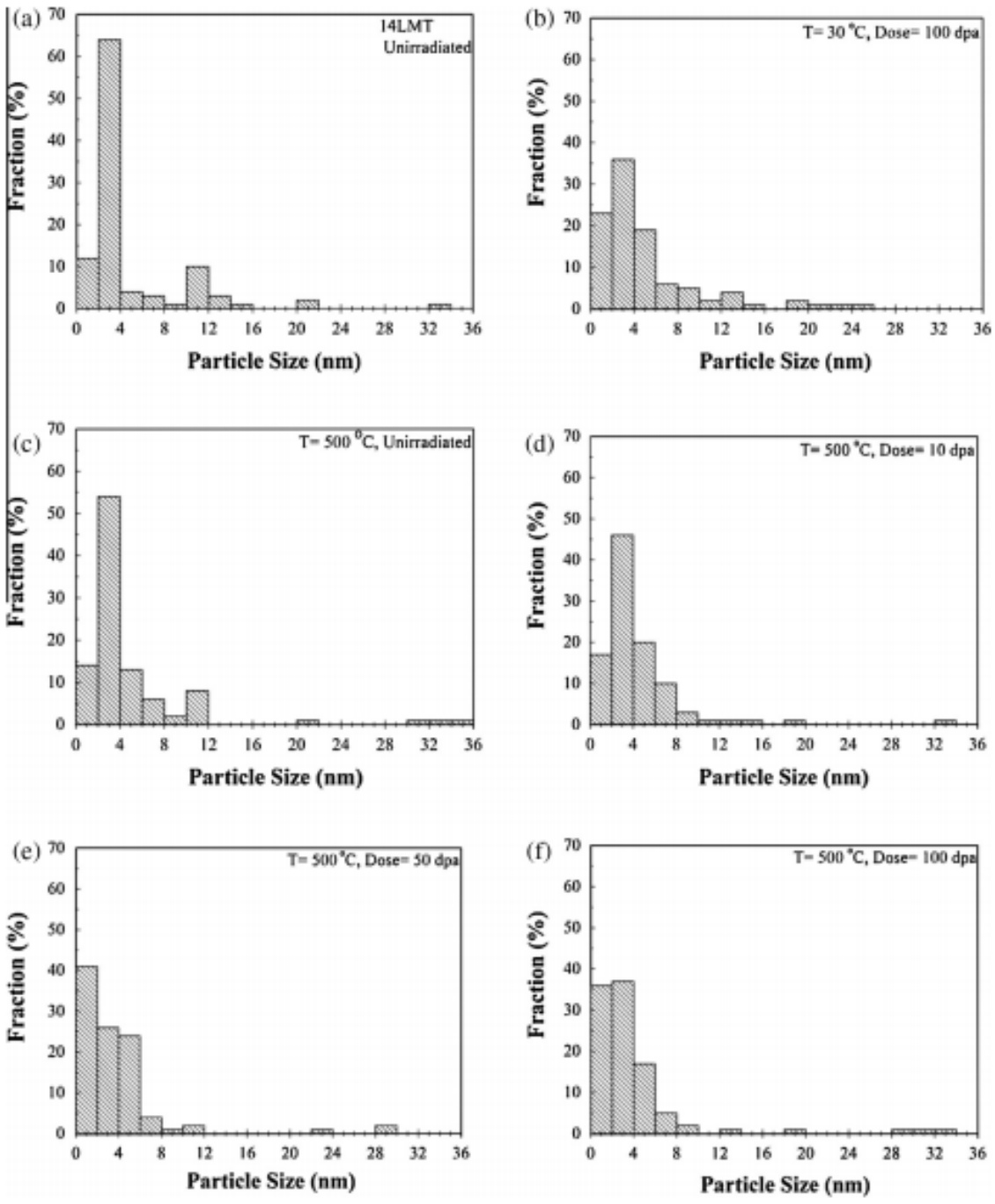

Fig. 4. Particle size (radius) distribution for 14LMT samples: (a) unirradiated, (b) irradiated at 30 C for 100 dpa, (c) unirradiated at 500 C, (d) irradiated at 500 C for 10 dpa, (e) irradiated at 500 C for 50 dpa and (f) irradiated at 500 C for 100 dpa.

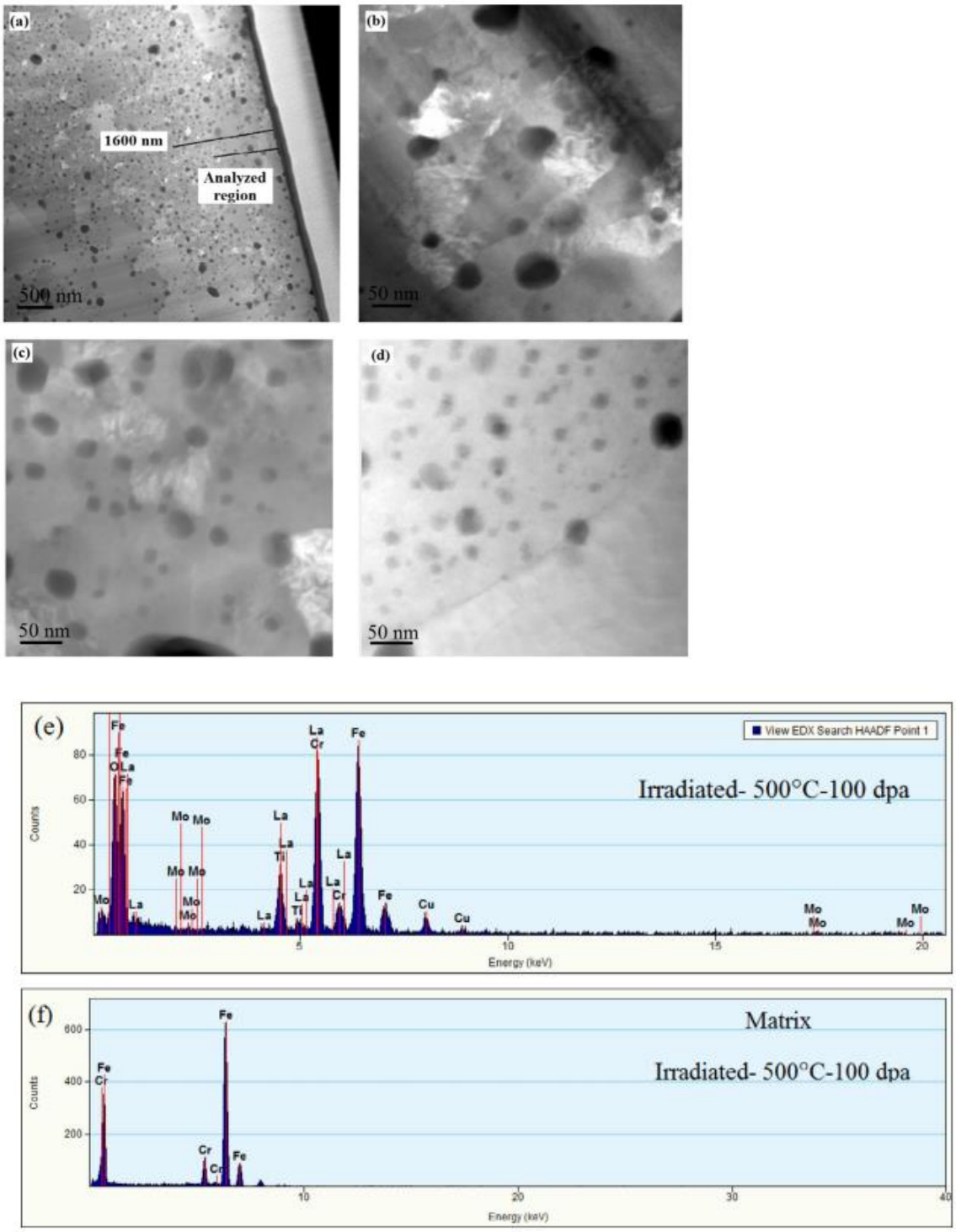

Fig. 5. HAADF STEM micrograph overall view of the specimen: (a) the overview of the sample, (b) unirradiated, (c) unirradiated at 500 C, (d) irradiated at 500 C for 100 dpa, (e) an EDS spectrum from oxide particles in sample irradiated at 500 C for 100 dpa and (f) an EDS spectrum from matrix in sample irradiated at 500 C for 100 dpa.

In order to study possible element segregation under ion irradiation, we performed atom probe tomography (APT). High resolution TEM (HRTEM) micrographs combined with APT maps of the NCs are shown in Fig. 7(a–e). Number density of the Cr-, Ti-, La-, O-enriched NCs in the 14LMT alloy (unirradiated) was estimated to be 1.2×10^{24} m^{-3} with an average Guinier radius of 1.5 ± 0.3 nm. The HAADF STEM micrographs obtained from NCs and some larger oxide particles along with APT results of 14LMT sample irradiated at 500 C for 100 dpa are shown in Fig. 7(f–j). Number density of the Cr-, Ti-, La-, O-enriched NCs in the 14LMT sample irradiated at 500 °C for 100 dpa was estimated to be 1.2×10^{24} m^{-3} with an average Guinier radius of 1.3 ± 0.2 nm. The average atomic composition of NCs was slightly affected by ion irradiation. The concentration of Fe, Mo and Ti in NCs slightly decreased, and the concentration of Cr and La in NCs showed an increase after irradiation at 500 °C. During the formation of collision cascades at 500 °C, the solute atoms, such as Cr and Ti, were ejected from the NCs and re-diffused from the matrix to the NCs. Certain et al. [15] suggested that under high temperature irradiation back diffusion of solutes from the matrix to the NCs becomes possible, thus leading to ‘‘dynamic stability’’ in NCs. On the contrary, the instability of NCs after irradiation at −75 °C was associated with low or no diffusion of solute atoms indicating that NCs are more (dynamically) stable at higher temperatures rather than lower temperatures. The reason for the increase in Cr concentration and decrease in the Ti concentration in NCs after irradiation is not clear at this point. At 500 °C the diffusion coefficient of Cr in α-Fe is approximately 2.5 times greater than that of Ti in a-Fe. For Cr diffusion in α-Fe, Q = 55,400 ± 700 cal/mol and Do = 0.64 ± 0.07 cm^2 s^{-1} [16] and for Ti diffusion in a-Fe, Q = 59,200 cal/mol and Do = 3.15 cm^2s^{-1}[17]. The difference in diffusivities seems relevant to the observed difference in Cr and Ti concentrations. The La + Ti:O ratio in NCs before and after irradiation was 0.98 and 1.15, respectively, implying a slight increase in La + Ti:O ratio after irradiation. For calculating La + Ti:O ratio, the influence of the matrix has been removed here. The number density of NCs remained unchanged after irradiation up to 100 dpa. The radius of NCs exhibited a slight refining after high temperature irradiation. The APT maps and the size distribution histograms of NCs in a smaller volume of 14LMT alloy unirradiated and irradiated at 500 °C with 100 dpa are presented in Fig. 8(a–h).

The size of NCs before and after irradiation did not show any significant changes except slight refinement. Size distribution histograms of NCs for both unirradiated and irradiated 14LMT alloys were constructed from several APT data sets and are illustrated in Fig. 8(d) and Fig. 8(h), respectively. The size distribution histograms for both unirradiated and irradiated alloys at 500 °C for 100 dpa were similar. However, the latter histogram showed a slight decrease in the size of NCs. Pareige et al. [18] studied the stability of NCs in 12YWT after irradiation to 0.7 dpa with 150 keV Fe ions at 300 C. The size, number density, and chemical composition of the NCs were also similar to those observed in unirradiated specimens. However, under neutron irradiation, the instability of oxide particles in terms of morphology and crystallinity might be an issue as reported by Monnet et al. [19].

In summary, heavy self-ion irradiation experiments were performed at 30 °C and 500 °C with 10, 50 and 100 dpa doses on a lanthana-bearing nanostructured ferritic steel, 14LMT. The microstructure and hardness of the irradiated samples were evaluated and compared with those of the unirradiated sample. The overall grain structure and dislocation configuration did not exhibit any significant changes from thermal treatments to 500 °C or ion irradiation. No clear evidence of dislocation loops or void swelling was found in the irradiated samples. The dislocation density constantly increased with increasing irradiation dose causing hardening across the entire irradiation damage depth. The high number density of the La–Ti–Oenriched particles could play a significant role in stabilizing the dislocation configurations by

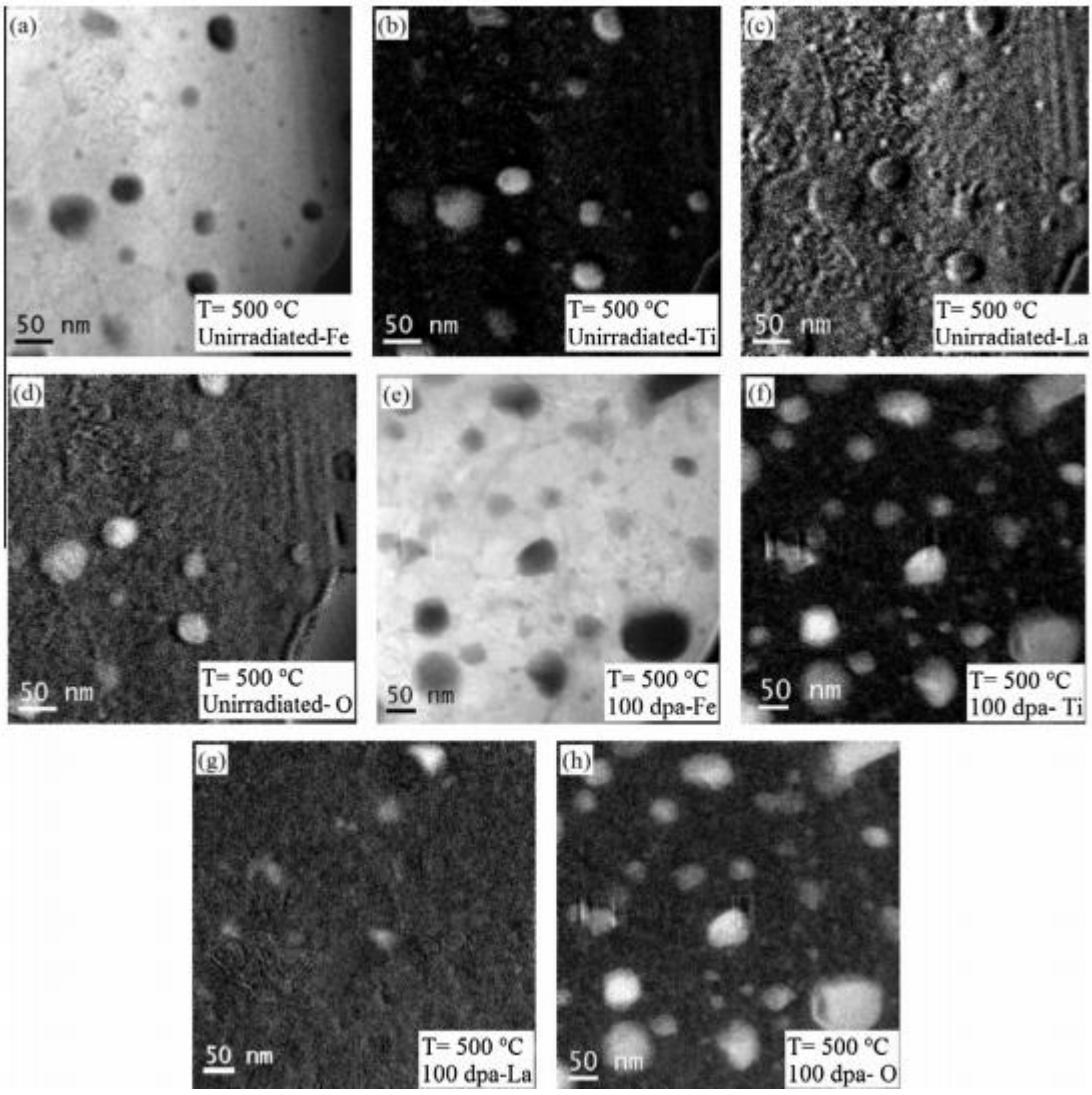

Fig.6. EFTEM maps for 14LMT alloy: (a) unirradiated – Fe, (b) unirradiated – Ti, (c) unirradiated – La, (d) unirradiated – O, (e) 100 dpa –Fe, (f) 100 dpa – Ti, (g) 100 dpa – La and (h) 100 dpa – O (the temperature condition for all micrographs was at 500 C and the energy edges used in the images are: La–M, O–K, Fe–L, Ti–L).

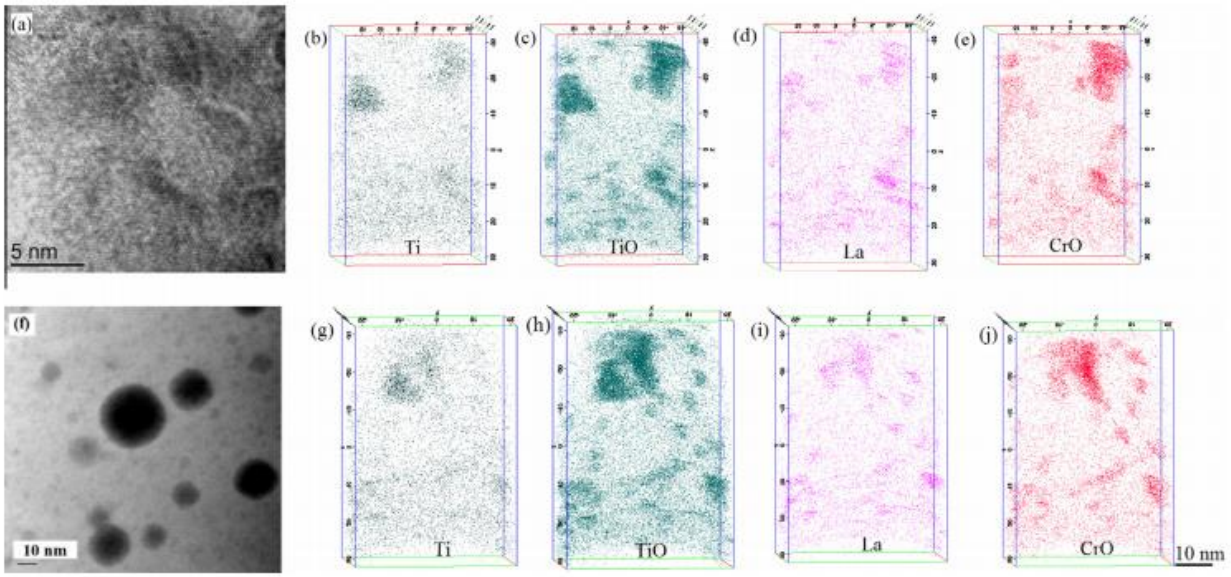

Fig.7. (a) HRTEM micrograph obtained from 14LMT unirradiated specimen prior to APT, corresponding (b) Ti map, (c) TiO map, (d) La map, (e) CrO map; (f) HAADF STEM micrograph obtained from 14LMT irradiated at 500 C for 100 dpa prior to APT, corresponding (g) Ti map, (h) TiO map, (i) La map, and (j) CrO map.

acting as sites for defect recombination. The shape, morphology and number density of NCs did not reveal any significant changes after irradiation up to 100 dpa. The radius of NCs, however, decreased slightly after elevated temperature irradiation at 500 °C and 100 dpa. The Cr and La concentration of NCs was found to be higher, and Ti concentration of NCs was lower than that of the starting material after irradiation at 500 °C and 100 dpa.

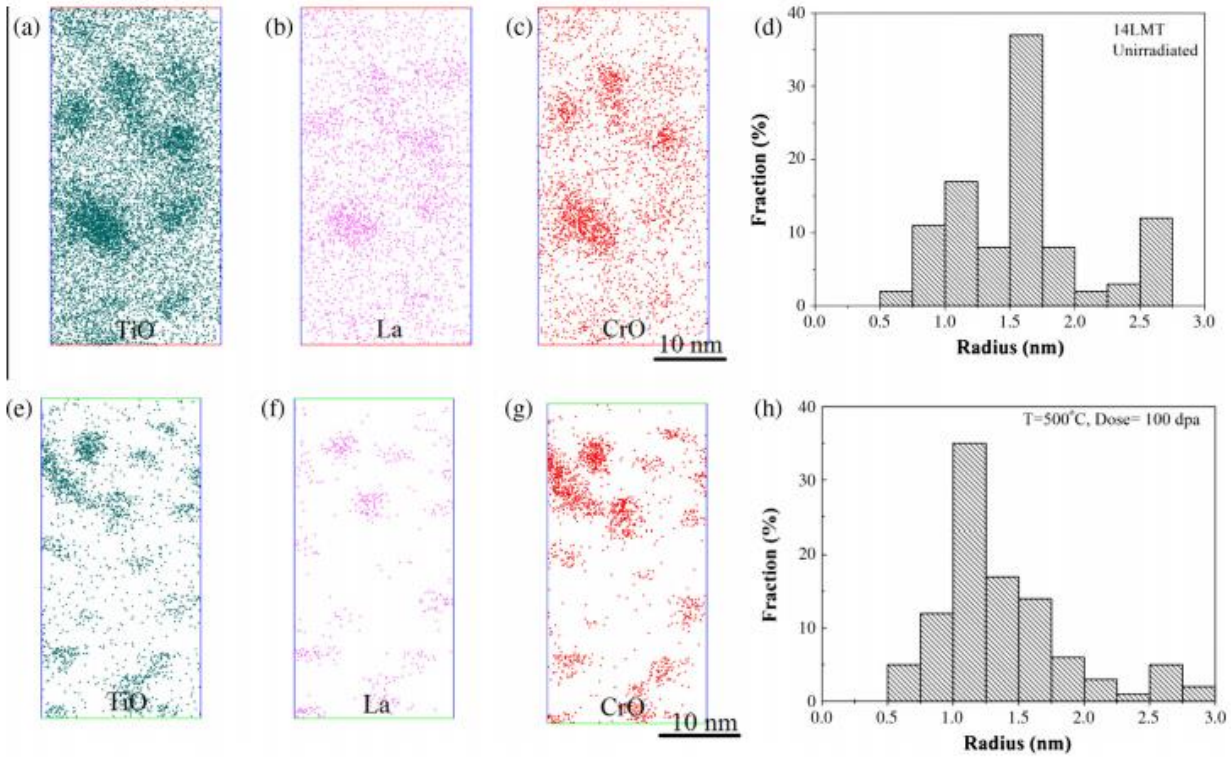

Fig.8. The APT maps of unirradiated specimen showing NCs enriched in: (a) TiO, (b) La, (c) CrO, (d) radius distribution histogram of NCs for the unirradiated 14LMT, (e) the APT maps of irradiated showing NCs enriched in (e) TiO, (f) La, (g) CrO and (h) NCs radius distribution histogram for 14LMT irradiated at 500 C for 100 dpa.

References

[1] T.R. Allen, J. Gan, J.I. Cole, M.K. Miller, J.T. Busby, S. Shutthanand, S. Thevuthasan, J. Nucl. Mater. 375 (2008) 26–37.

[2] M.K. Miller, C.M. Parish, Mater. Sci. Technol. 27 (2011) 729–734.

[3] M.J. Alinger, G.R. Odette, D.T. Hoezler, Acta Mater. 57 (2009) 392–406.

[4] N. Akasaka, S. Yamashita, T. Yoshitake, S. Ukai, A. Kimura, J. Nucl. Mater. 329– 333 (2004) 1053–1056.

[5] R.L. Klueh, P.J. Maziasz, I.S. Kim, L. Heatherly, D.T. Hoelzer, N. Hashimoto, E.A. Kenik, K. Miyahara, J. Nucl. Mater. 307 (2002) 773–777.

[6] H. Kishimoto, K. Yutani, R. Kasada, O. Hashitomi, A. Kimura, J. Nucl. Mater. 367–370 (2007) 179–184.

[7] J.J. Fisher, Patent, U.S.A., 1978.

[8] M.K. Miller, D.T. Hoelzer, E.A. Kenik, K.F. Russell, J. Nucl. Mater. 329-333 (Part A) (2004) 338–341.

[9] G.R. Odette, M.J. Alinger, B.D. Wirth, Annu. Rev. Mater. Res. 38 (2008) 471–503.

[10] S. Yamashita, S. Ohtsuka, N. Akasaka, S. Ukai, S. Ohnukiy, Philos. Mag. Lett. 84 (2004) 525–529.

[11] L. Shao, C.C. Wei, J. Gigax, A. Aitkaliyeva, D. Chen, B.H. Sencer, F.A. Garner, J. Nucl. Mater. 453 (2014) 176–181.

[12] S.J. Zinkle, P.J. Maziasz, R.E. Stoller, J. Nucl. Mater. 206 (1993) 266–286.

[13] G. Was, Fundamentals of Radiation Materials Science: Metals and Alloys, Springer, Berlin, 2007.

[14] R. Bullough, M.R. Hayns, C.H. Woo, J. Nucl. Mater. 84 (1979) 93–100.

[15] A. Certain, S. Kuchibhatla, V. Shutthanandan, D.T. Hoelzer, T.R. Allen, J. Nucl. Mater. 434 (2013) 311–321.

[16] A.W. Bowen, G.M. Leak, Metal. Trans. 1 (1970) 2767–27723.

[17] G.B. Gibbs, Trans. TMS-AIME 239 (1967) 236.

[18] P. Pareige, M.K. Miller, R.E. Stoller, D.T. Hoelzer, E. Cadel, B. Radiguet, J. Nucl. Mater. 360 (2007) 136–142.

[19] I. Monnet, P. Dubuisson, Y. Serruys, M.O. Ruault, O. Kaitasov, B. Jouffery, J. Nucl. Mater. 335 (2004) 311–321.